DECLARATION OF JUNE ANN MUNFORD

1. My name is June Ann Munford. I am over the age of 18, have personal knowledge of the facts set forth herein, and am competent to testify to the same.

2. I earned a Master of Library and Information Science (MLIS) from the University of Wisconsin-Milwaukee in 2009. I have over ten years of experience in the library/information science field. Beginning in 2004, I have served in various positions in the public library sector including Assistant Librarian, Youth Services Librarian and Library Director. I have attached my Curriculum Vitae as Appendix CV.

3. During my career in the library profession, I have been responsible for materials acquisition for multiple libraries. In that position, I have cataloged, purchased and processed incoming library works. That includes purchasing materials directly from vendors, recording publishing data from the material in question, creating detailed material records for library catalogs and physically preparing that material for circulation. In addition to my experience in acquisitions, I was also responsible for analyzing large collections of library materials, tailoring library records for optimal catalog

search performance and creating lending agreements between libraries during my time as a Library Director.

4. I am fully familiar with the catalog record creation process in the library sector. In preparing a material for public availability, a library catalog record describing that material would be created. These records are typically written in Machine Readable Catalog (herein referred to as "MARC") code and contain information such as a physical description of the material, metadata from the material's publisher, and date of library acquisition. In particular, the 008 field of the MARC record is reserved for denoting the date of creation of the library record itself. As this typically occurs during the process of preparing materials for public access, it is my experience that an item's MARC record indicates the date of an item's public availability.

5. Typically, in creating a MARC record, a librarian would gather various bits of metadata such as book title, publisher and subject headings among others and assign each value to a relevant numerical field. For example, a book's physical description is tracked in field 300 while title/attribution is tracked in field 245. The 008 field of the MARC record is reserved for denoting the creation of the library record itself. As this is the only date reflecting the inclusion of said materials within the library's collection, it is my experience

that an item's 008 field accurately indicates the date of an item's public availability.

6. I have reviewed Exhibit 1015 a document entitled *Characterization of Electrodeposited Copper Foil Surface Roughness for Accurate Conductor Power Loss Modeling* by Michael B. Griesi.

7. Attached hereto as Appendix GRIESI01 is a screen capture of a website entitled "Characterization of Electrodeposited Copper Foil Surface Roughness for Accurate Conductor Power Loss Modeling" as hosted on the University of South Carolina: Theses and Dissertations website. I secured these screen captures myself from https://scholarcommons.sc.edu/etd/2958/.

8. Appendix GRIESI01 contains a true and complete copy of *Characterization of Electrodeposited Copper Foil Surface Roughness for Accurate Conductor Power Loss Modeling* by Michael B. Griesi. In comparing Appendix GRIESI01 to Exhibit 1015 it is my determination that Exhibit 1015 is a true and correct copy of *Characterization of Electrodeposited Copper Foil Surface Roughness for Accurate Conductor Power Loss Modeling*.

9. The 'Date of Award" field present in Appendix GRIESI01 indicates this thesis was first submitted to the University of South Carolina as of

December 15, 2014. The ‘PlumX Metrics’ field indicates this thesis was first made available to download by the University of South Carolina as of January 21, 2015.

10. Attached hereto as Appendix GRIESI02 is a screen capture of a website entitled "A Low Loss X-band Filter Using 3-D Polyjet Technology" as hosted on the ResearchGate website. I secured these screen captures myself from https://www.researchgate.net/publication/275034841_A_Low_Loss_X-band_Filter_Using_3-D_Polyjet_Technology.

11. ResearchGate is an online database that tracks scholarly publications and offers copies of those publications for download. Appendix GRIESI02 contains a true and complete copy of "A Low Loss X-band Filter Using 3-D Polyjet Technology" as published in *Proceedings of the 2015 IEEE MTT-S International Microwave Symposium* from the ResearchGate website. Page 9 of Appendix GRIESI02 includes a citation to the Griesi thesis.

12. Attached hereto as Appendix GRIESI03 is a screen capture of a website entitled "A Low Loss X-band Filter Using 3-D Polyjet Technology" as

hosted on the IEEE Xplore website. I secured these screen captures myself from https://ieeexplore.ieee.org/document/7166895/references#references.

13. Appendix GRIESI03 is a page describing "A Low Loss X-band Filter Using 3-D Polyjet Technology" as published in *Proceedings of the 2015 IEEE MTT-S International Microwave Symposium.* IEEE is the publisher of *Proceedings of the 2015 IEEE MTT-S International Microwave Symposium* and page 1 of this IEEE page indicates this symposium took place between May 17 – 22, 2015.

14. Appendix GRIESI01 indicates *Characterization of Electrodeposited Copper Foil Surface Roughness for Accurate Conductor Power Loss Modeling* was first made available to download by the University of South Carolina as of January 21, 2015. Appendix GRIESI02 is a paper published that cites the Griesi thesis, published via the 2015 IEEE MTT-S International Microwave Symposium which took place between May 17 – 22, 2015. As such it is my determination that *Characterization of Electrodeposited Copper Foil Surface Roughness for Accurate Conductor Power Loss Modeling* was first made available to the public as of January 21, 2015 and certainly no later than May 22, 2015.

15. I have reviewed Exhibit 1005, "Assessment of Activated Polyacrylamide and Guar as Organic Additives in Copper Electrodeposition" by C.P. Fabian, et al. as published in *Hydrometallurgy*, April 2007

16. Attached hereto as Appendix FABIAN01 is a true and correct copy of the MARC record for *Hydrometallurgy* as held by the Penn State University library. I secured this record myself from the library's public catalog. The MARC record contained within Appendix FABIAN01 accurately describes the title, author, publisher, and ISSN number of *Hydrometallurgy.* The 'Dates of Publication and/or Sequential Designation' field of this record visible on page 2 indicates this collection includes the April 2007 edition of *Hydrometallurgy* containing "Assessment of Activated Polyacrylamide and Guar as Organic Additives in Copper Electrodeposition".

17. Attached hereto as Appendix FABIAN02 is a true and correct copy of "Assessment of Activated Polyacrylamide and Guar as Organic Additives in Copper Electrodeposition" as published in *Hydrometallurgy* as held by the Penn State University library. I secured this file myself from the library's collection. In comparing Exhibit 1005 to Appendix FABIAN02, it is my determination that Exhibit 1005 is a true and correct copy of "Assessment of Activated Polyacrylamide and Guar as Organic Additives in Copper

Electrodeposition" by C.P. Fabian, et al. as published in *Hydrometallurgy* April 2007.

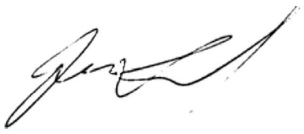
18. The 008 field of the MARC record in Appendix FABIAN01 indicates the date of record creation. The 008 field of Appendix FABIAN01 indicates the Penn State University library first acquired this journal as of April 6, 1998. Considering this information, it is my determination that *Hydrometallurgy* April 2007 and therefore "Assessment of Activated Polyacrylamide and Guar as Organic Additives in Copper Electrodeposition" was made available to the public shortly after its initial release in April 2007.

19. I have been retained on behalf of the Petitioner to provide assistance in the above-illustrated matter in establishing the authenticity and public availability of the documents discussed in this declaration. I am being compensated for my services in this matter at the rate of $200.00 per hour plus reasonable expenses. My statements are objective, and my compensation does not depend on the outcome of this matter.

20. I declare under penalty of perjury that the foregoing is true and correct. I hereby declare that all statements made herein of my own knowledge are true and that all statements made on information and belief are believed to

be true; and further that these statements were made the knowledge that willful false statements and the like so made are punishable by fine or imprisonment, or both, under Section 1001 of Title 18 of the United States Code.

Dated: 9/19/2024



June Ann Munford

APPENDIX CV

June A. Munford
Curriculum Vitae

Education

University of Wisconsin-Milwaukee - MS, Library & Information Science, 2009
Milwaukee, WI

- Coursework included cataloging, metadata, data analysis, library systems, management strategies and collection development.
- Specialized in library advocacy, cataloging and public administration.

Grand Valley State University - BA, English Language & Literature, 2008
Allendale, MI

- Coursework included linguistics, documentation and literary analysis.
- Minor in political science with a focus in local-level economics and government.

Professional Experience

Researcher / Expert Witness, October 2017 – present
Freelance ● Pittsburgh, Pennsylvania & Grand Rapids, Michigan

- Material authentication and public accessibility determination. Declarations of authenticity and/or public accessibility provided upon research completion. Experienced with appeals and deposition process.

- Research provided on topics of public library operations, material publication history, digital database services and legacy web resources.

- Past clients include Alston & Bird, Arnold & Porter, Baker Botts, Fish & Richardson, Erise IP, Irell & Manella, O'Melveny & Myers, Perkins-Coie, Pillsbury Winthrop Shaw Pittman and Slayden Grubert Beard.

Library Director, February 2013 - March 2015
Dowagiac District Library ● Dowagiac, Michigan

- Executive administrator of the Dowagiac District Library. Located in

Southwest Michigan, this library has a service area of 13,000, an annual operating budget of over $400,000 and total assets of approximately $1,300,000.

● Developed careful budgeting guidelines to produce a 15% surplus during the 2013-2014 & 2014-2015 fiscal years while being audited.

● Using this budget surplus, oversaw significant library investments including the purchase of property for a future building site, demolition of existing buildings and building renovation projects on the current facility.

● Led the organization and digitization of the library's archival records.

● Served as the public representative for the library, developing business relationships with local school, museum and tribal government entities.

● Developed an objective-based analysis system for measuring library services - including a full collection analysis of the library's 50,000+ circulating items and their records.

November 2010 - January 2013
Librarian & Branch Manager, Anchorage Public Library ● Anchorage, Alaska

● Headed the 2013 Anchorage Reads community reading campaign including event planning, staging public performances and creating marketing materials for mass distribution.

● Co-led the social media department of the library's marketing team, drafting social media guidelines, creating original content and instituting long-term planning via content calendars.

● Developed business relationships with The Boys & Girls Club, Anchorage School District and the US Army to establish summer reading programs for children.

June 2004 - September 2005, September 2006 - October 2013
Library Assistant, Hart Area Public Library
Hart, MI

● Responsible for verifying imported MARC records and original MARC

cataloging for the local-level collection as well as the Michigan Electronic Library.

● Handled OCLC Worldcat interlibrary loan requests & fulfillment via ongoing communication with lending libraries.

Professional Involvement

Alaska Library Association - Anchorage Chapter
- Treasurer, 2012

Library Of Michigan
- Level VII Certification, 2008
- Level II Certification, 2013

Michigan Library Association Annual Conference 2014
- New Directors Conference Panel Member

Southwest Michigan Library Cooperative
- Represented the Dowagiac District Library, 2013-2015

Professional Development

Library Of Michigan Beginning Workshop, May 2008
Petoskey, MI
- Received training in cataloging, local history, collection management, children's literacy and reference service.

Public Library Association Intensive Library Management Training, October 2011
Nashville, TN
- Attended a five-day workshop focused on strategic planning, staff management, statistical analysis, collections and cataloging theory.

Alaska Library Association Annual Conference 2012 - Fairbanks, February 2012
Fairbanks, AK
- Attended seminars on EBSCO advanced search methods, budgeting, cataloging, database usage and marketing.

Depositions

2019 ● Fish & Richardson

Apple v. Qualcomm (IPR2018-001281, 39521-00421IP, IPR2018-01282 and 39521-00421IP2)

2019 ● Erise IP

Implicit, LLC v. Netscout Systems, Inc (Civil Action No. 2:18-cv-53-JRG)

2019 ● Perkins-Coie

Adobe Inc. v. RAH Color Technologies LLC (Cases IPR2019-00627, IPR2019-00628, IPR2019-00629 and IPR2019-00646)

2020 ● O'Melveny & Myers

Maxell, Ltd. v. Apple Inc. (Case No. 5:19-cv-00036-RWS)

2021 ● Pillsbury Winthrop Shaw Pittman LLP

Intel v. SRC (IPR2020-1449)

2022 ● Perkins-Coie

Realtek v. Future Link (IPR2021-01182)

2023 ● Fish & Richardson

Neuroderm Ltd. v. Abbvie, Inc (Case No. PGR2022-00040)

2023 ● Fish & Richardson

Nearmap US Inc. v. Pictometry International Corp. (IPR2022-00735)

2023 ● Fish & Richardson

Samsung Electronics v. MemoryWeb LLC (Case No. 39843-0136PS1)

2023 ● Pillsbury Winthrop Shaw Whitman LLP

Gravel Rating Systems v. Costco Wholesale Corp. (Civil Action No. 4:21-cv-149-ALM)

2024 ● Willkie-Farr

Netflix, Inc. v. VideoLabs. Inc. (IPR2023-00628)

Limited Case and Clientele History

Alston & Bird

- Ericsson

  v. Collision Communications (IPR2022-01233)

- Nokia

  v. Neptune Subsea, Xtera (Case No. 1:17-cv-01876)

- Universal Electronics Inc

  v. Roku Inc (IPR2022-00818)

Arnold & Porter

- Ivantis

  v. Glaukos (Case No. 8:18-cv-00620)

- Samsung

  v. Jawbone (Case No. 2:21-cv-00186)

Benesch Friedlander Coplan & Aronoff

- Voyis

  v. Cathx (Case No. 5:21-cv-00077-RWS)

Deschert LLP

- Smaxtec Animal Care

  v. ST Reproductive Technologies, LLC (IPR2024-00885)

Erise I.P.

- Apple

  v. Ericsson Inc. (IPR2022-00715)

  v. Future Link Systems (IPRs 6317804, 6622108, 6807505, and 7917680)

  v. INVT (Case No. 20-1881)

  v. Navblazer LLC (IPR2020-01253)

  v. Qualcomm (IPR2018-001281, 39521-00421IP, IPR2018-01282, 39521-00421IP2)

  v. Quest Nettech Corp (Case No. 2:19-cv-00118-JRG)

  v. Telefonaktiebolaget LM Ericsson (IPR2022-00275)

  v. Theta IP, LLC (IPR2024-00818)

- Fanduel

  v. CGT (Case No. 19-1393)

- Garmin

  v. Phillips North America LLC (Case No. 2:19-cv-6301-AB-KS)

- Netscout
    - v. Longhorn HD LLC (Case No. 2:20-cv-00349)
    - v. Implicit, LLC (Civil Action No. 2:18-cv-53-JRG)

- Sony Interactive Entertainment LLC
    - v. Bot M8 LLC (IPR2020-01288)
    - v. Infernal Technology LLC (Case No. 2:19-CV-00248-JRG)

- Unified Patents
    - v. GE Video Compression (Civil Action No. 2:19-cv-248)

Fish & Richardson

- Apple
    - v. AliveCor (3:21-cv-03958)
    - v. LBS Innovations (Case No. 2:19-cv-00119-JRG-RSP)
    - v. Koss Corporation (IPR2021-00305)
    - v. Masimo (IPR 50095-0012IP1, 50095-0012IP2, 50095-0013IP1, 50095-0013IP2, 50095-0006IP1, 50095-0135IP1)
    - v. Neonode (Case No. 21-cv-08872-EMC)
    - v. Qualcomm (IPR2018-001281, 39521-00421IP, IPR2018-01282, 39521-00421IP2)

- Dell
    - v. Neo Wireless (IPR2022-00616)

- Dish Network
    - v. Entropic Communications, LLC (Case No. 2:2023-CV-01043)

v. Realtime Adaptive Streaming (Case No. 1:17-CV-02097-RBJ)

v. TQ Delta LLC (Case No. 18-1798)

- Evapco Dry Cooling

v. SPG Dry Cooling (IPR2021-00688)

- Genetec

v. Sensormatic Electronics (Case No. 1:20-CV-00760)

- Huawei

v. Bell Northern Research LLC (IPR2019-01174)

- Kianxis

v. Blue Yonder (Case No. 3:20-cv-03636)

- LG Electronics

v. Bell Northern Research LLC (Case No. 3:18-cv-2864-CAB-BLM)

- Metaswitch

v. Sonus Networks (IPR2018-01719)

- Microsoft

v. Throughputer Inc (IPR2022-00757)

- Mom Enterprises

v. Ddrops Company (Case No. 1:22-cv-00332)

- MLC Intellectual Property

v. MicronTech (Case No. 3:14-cv-03657-SI)

- Nearmap Inc
  - v. EagleView Technologies (IPR2022-01009)

- Neuroderm Ltd.
  - v. Abbvie, Inc (Case No. PGR2022-00040)

- Realtek Semiconductor
  - v. Future Link (IPR2021-01182)

- Quectel
  - v. Koninklijke Philips (Case No. 1:20-cv-01710)

- Samsung
  - v. Aire Technology (IPR2022-00877)
  - v. Bell Northern Research (Case No. 2:19-cv-00286-JRG)
  - v. Communication Technologies Inc (IPR2022-01221)
  - v. Jawbone Innovations (IPR2022-00865)
  - v. MemoryWeb LLC (IPR2022-00885)
  - v. Dodots Licensing Solutions (IPR2023-00701)
  - v. Telefonaktiebolaget LM Ericsson (IPR2021-00615)

- Texas Instruments
  - v. Vantage Micro LLC (IPR2020-01261)

- Xilinx
  - v. Sentient Sensors LCC (Case No. 1:22-cv-00173)

Groombridge Wu

- Nearmap

  v. Eagle View Technologies Inc. and Pictometry International Corp. (Case No. 2:21-cv-00283-TS-DAO)

Irell & Manella

- Curium

O'Melveny & Myers

- Apple

  v. Maxell (Case No. 5:19-cv-00036-RWS)

- Disney Media & Entertainment Distribution LLC

  v. Digital Media Technology Holdings, LLC (Case No. 2:22-cv-01642)

- Micron Technology Inc.

  v. Besang Inc (IPR2023-00900)

- Samsung

  v. Daedalus Prime LLC (1335 Investigation)

Perkins-Coie

- Amazon

  v. Nokia (IPR2024-00847 and IPR2024-00848)

- Heru Industries

  v. The UAB Research Foundation (IPR2022-01148)

- Intel Corporation

  v. BeSang Inc. (IPR2023-00991)

  v. BitMICRO (Case No. 5:23-cv-00625)

  v. Telefonaktiebolaget L M Ericsson (IPR2024-00610)

- Realtek Semiconductor

  v. Future Link (IPR2021-01182)

- Twitter Inc

  v. VOIP-Pal.com (Case No. 3:20-cv-02397-JD)

- TCL Industries

  v. Koninklijke Philips NV (IPR2021-00495, IPR2021-00496 and IPR2021-00497)

Pillsbury Winthrop Shaw Pittman

- Intel

  v. FG SRC LLC (Case No. 6:20-cv-00315)

- Gravel Rating Systems

  v. Costco (Case No. 4:21-cv-149)
  v. Lowe's Home Centers (Case No. 4:21-cv-150)
  v. T-Mobile USA (Case No. 4:21-cv-152)
  v. Kohl's Inc. (Case No. 4:21-cv-258)
  v. Under Armor (Case No. 4:21-cv-356)

Quinn Emanuel

- ServiceNow, Inc.

  v. InQuisient, Inc. (Case No. 22-900-CJB)

- Wolfspeed

  v. The Trustees of Purdue University (Case No. 1:2021-cv-00840)

Sheppard, Mullin, Richter & Hampton LLP

- Cadence Design Systems Inc.

  v. Semiconductor Design Technologies (Case No. 3:23-cv-01001)

Stern, Kessler, Goldstein & Fox

- Preliminary Research

Willkie, Farr & Gallagher LLP

- Neurent

  v. The Foundry, LLC (IPR2024-00669)

- Netflix, Inc.

  v. VideoLabs, Inc. (IPR2023-00628)

APPENDIX FABIAN01

MARC View

LEADER 01647nas a2200409 a 4500				
001 44921680				
003 SIRSI				
005 20240714090125.0				
006 m o d				
007 cr n				
008 980406c19759999nyuzx pss 0 a0eng c				
010				a| 2006264670
016	7			a| 012433198 2| Uk
019				a| DO NOT EDIT this 360 MARC RECORD
022				a| 1879-1158 l| 0304-386X y| 0304-386X
035				a| (WaSeSS)ssj0006371
040				a| OH1 b| eng c| OH1 d| OCL d| OCLCQ d| BUF d| U9S d| GUA d| OCLCQ d| OCLCF d| OCLCQ d| UKMGB d| VT2 d| OCLCO d| OCLCQ d| UAB d| WaSeSS
042				a| pcc
050		4		a| TN688 b| .H89
130	0			a| Hydrometallurgy (Online)
222			0	a| Hydrometallurgy b| (Online)
245	1		0	a| Hydrometallurgy h| [electronic resource].
260				a| [New York, NY] : b| Elsevier, c| 1975-
310				a| Twenty issues yearly, b| <2005>-
321				a| Frequency varies
362	0			a| Vol. 1, issue 1 (Sept. 1975)-
500				a| Title from general information screen (viewed Apr. 6, 1998).
500				a| "An international journal devoted to all aspects of the aqueous processing of metals."
530				a| Also issued in print.
538				a| Mode of access: World Wide Web.
588				a| Latest issue consulted: Vol. 84, no. 3-4 (Nov. 2006) (viewed Nov. 18, 2006).
650			0	a| Hydrometallurgy v| Periodicals.
655			0	a| Electronic journals.
776	1			t| Hydrometallurgy x| 0304-386X w| (DLC) 76642001 w| (OCoLC)2147037
856	4		0	u| http://SK8ES4MC2L.search.serialssolutions.com/?V=1.0&L=SK8ES4MC2L&S=JCs&C=HYDR&T=marc
910				a| CONSER online
949				a| Electronic resource w| ASIS c| 1 i| 44921680-1001 l| ONLINE m| ONLINE r| Y s| Y t| ONLINE u| 7/20/2024 o| .STAFF. 360 MARC

ASK A LIBRARIAN

PennState

Copyright @2019 The Pennsylvania State University. All rights reserved. Except where otherwise noted, this work is subject to a Creative Commons Attribution 4.0 license. Details and exceptions.

Legal Statements | PSU Hotlines

PENN STATE UNIVERSITY LIBRARIES

Libraries Home (814) 865-6368
Libraries Intranet (Staff Only)
Accessibility Help
Website Feedback
Policies and Guidelines
Staff Directory

CONNECT WITH PENN STATE UNIVERSITY LIBRARIES

Facebook
Twitter
Instagram

Hydrometallurgy [electronic resource].

Uniform Title: Hydrometallurgy (Online)

Published: [New York, NY] : Elsevier, 1975-

Access Online

serialssolutions.com

ASK A LIBRARIAN

Dates of Publication and/or Sequential Designation
Vol. 1, issue 1 (Sept. 1975)-

Subject(s)
Hydrometallurgy—Periodicals

Genre(s)
Electronic journals

ISSN
1879-1158

Publication Frequency
Twenty issues yearly, <2005>-
Frequency varies

Note
Title from general information screen (viewed Apr. 6, 1998).
"An international journal devoted to all aspects of the aqueous processing of metals."

Other Forms
Also issued in print.

Technical Details
Mode of access: World Wide Web.

View MARC record | catkey: 44921680

PennState

Copyright @2019 The Pennsylvania State University. All rights reserved. Except where otherwise noted, this work is subject to a Creative Commons Attribution 4.0 license. Details and exceptions.

Legal Statements | PSU Hotlines

PENN STATE UNIVERSITY LIBRARIES
Libraries Home (814) 865-6368
Libraries Intranet (Staff Only)
Accessibility Help
Website Feedback
Policies and Guidelines
Staff Directory

CONNECT WITH PENN STATE UNIVERSITY LIBRARIES
Facebook
Twitter
Instagram

ScienceDirect

Hydrometallurgy
Volume 86, Issues 1–2, April 2007, Pages 44-55

Assessment of activated polyacrylamide and guar as organic additives in copper electrodeposition

C.P. Fabian [a b], M.J. Ridd [b], M.E. Sheehan [a]

Show more

Outline | Share Cite

https://doi.org/10.1016/j.hydromet.2006.11.002
Get rights and content

Abstract

The effect of current density, temperature, diffusion layer thickness (δ), deposition time, Guarfloc66 (Guar) and activated polyacrylamide (APAM) on the topography (surface roughness) of electrodeposited copper was studied. The level of these variables approximates current commercial copper electrowinning (EW) and electrorefining (ER) operating conditions. The effect of Guar and APAM on surface roughness and number of Peaks-per-Centimeter was assessed both in combination and alone using a rotating cylinder electrode (RCE) for up to 6-hour EW time. Observed effects on surface roughness indicate that a more uniform surface and lower roughness/smoother copper deposits were obtained using the additive APAM rather than Guar. Regression models indicate APAM has a significant effect on reducing surface roughness at 65 °C.

Bench-scale *continuous* electrowinning tests were carried out at 50 °C for 44.6 h using parallel plate electrodes into which APAM and Guar were dosed continuously and independently. These tests also indicated that APAM produces smoother deposits than Guar. The cross sections of the copper deposits from these tests showed that APAM exhibits a *slightly columnar* copper deposit and Guar produced a *porous* copper deposit. The copper deposit produced with additive APAM was brighter and produced greater amounts of both smaller and larger crystallite sizes than those obtained with Guar. This infers that APAM favours higher nucleation rates and greater 3D crystallite growth and coalescence than Guar.

Previous Next

Keywords

Copper; Electrodeposition; Electrowinning; Electrorefining; Polyacrylamide; Rotating cylinder electrode; Guar; Surface roughness; Statistical analysis

1. Introduction

In the copper deposition industry in general, organic additives and chloride ions need to be dosed to produce smooth deposits, free of voids or porosity. It is also known that organic additives significantly influence the current–potential relationship due to their competition for surface coverage with the components of the electrolyte system including chloride ions. Therefore these organic additives must be carefully selected according to their role at the metal/electrolyte interface to control the nucleation and growth during the deposition process. Table 1 summarizes the industry-standard additives used in copper EW, ER and in the damascene process for micro-electronics industry. Table 1 shows the typical concentration of these organic additives in the electrolyte bath and their respective roles. An electrode is polarized when, under constant experimental conditions, the potential in the presence of an additive, e.g., animal glue, PEG, is more negative than the potential without the additive. An electrode is depolarized when the potential in the presence of an additive, e.g., chloride ions, is less negative. The polarizer/inhibitor/leveller controls the vertical growth to produce smooth deposits by conferring preferential adsorption on the peaks or active sites. The grain refiner/accelerator may predominantly control the nucleation process or promote the formation of new nuclei to possibly form new crystallites at the recesses (Vereecken et al., 2005). This synergistic process between the inhibitor and grain refiner is aimed at improving the overall quality of the copper deposit: purity, smoothness and plant productivity i.e., elimination/reduction of short-circuits caused by dendrites.

Table 1. Industry-standard additives used in copper electrometallurgy

Role of the additive	Electrorefining		Electrowinning		Micro-electronics, PCB and IC	
	Additive	mg/L	Additive	mg/L	Additive	mg/L
Leveller	Glue	1	Nil	Nil	PEG* and JGB	100–300 and 1
Brightener**			Guar	0.25–5		
Grain refiner***	Thiourea	2	Nil	Nil	SPS/MPSA	1/1
Depolarizer	Cl^-	50–60	Cl^-	20–25	Cl^-	40–60

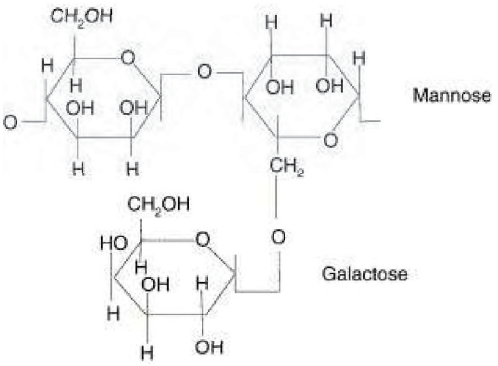
*PEG, polyethylene glycol; SPS, bis(3-sulfo-propyl) disulfide; JGB, Janus Green B (safranine dye); MPSA, 3-mercapto-1-propanesulfinate. **Guar is also known as weak polarizer in the industry. ***Grain refiner or accelerator.

The first step of metal deposition is the formation of nuclei of the depositing metal on a foreign substrate and on a substrate of the same metal. The structure of the first monolayer(s), has an impact on the deposition of further layers and therefore on the morphology of the deposited metal. The competition between nucleation and growth determines the smoothness of the deposit: the higher the nucleation rate; the finer the crystal size (Budevski et al., 1996). Moreover, the forms of the growing crystals determine their physical appearance and structure. A higher crystal size growth rate, normal to the substrate, leads to a more

fibrous/columnar structure. A brightening effect can be achieved when large developed crystal faces grow parallel to the substrate (Budevski et al., 1996).

It has been shown elsewhere (Fabian, 2005, Fabian et al., 2006b) that a rotating cylinder electrode (RCE) may be applied as a novel method of determining the effect of the preparation media of polyacrylamide (PAM) on the surface roughness of electrodeposited copper. It has been shown that when a high molecular weight PAM (MW 15 million Dalton) is prepared in 16-fold diluted copper electrolyte at 50 °C for 2 h and dosed into an EW cell, the electrodeposited copper had a significantly lower mean surface roughness than was the case when polyacrylamide was prepared in water or full-strength electrolyte or alkaline solution. The hydrolysis of PAM in pH 2 solutions is reported to produce a block copolymer (Halverson et al., 1985, Panzer and Halverson, 1988, Panzer et al., 1984). The PAM hydrolysed in 16-fold diluted copper electrolyte (pH 1.5) was named 'activated polyacrylamide' (APAM). It has been also shown that APAM also produced deposits exhibiting a lower surface roughness than polyacrylic acid (Fabian, 2005).

Guar is a naturally occurring galacto-mannan polymer, a polysaccharide, used as flocculant and coagulant with typical molecular weights ranging from 200,000 to 500,000 Da. Guar is a linear D-mannose sugar with a D-galactose sugar chain on every other mannose as shown below, Fig. 1 (Mark et al., 1969). Guar is the industry-standard organic additive used in copper EW as a weak levelling agent for about 40 years to produce bright copper deposits (Langner et al., 1989, Stantke, 1999).



Download: Download full-size image

Fig. 1. The chemical structure of Guar based on Mark et al. (1969).

Pye and Schurz (1957) patented the electrowinning of zinc and copper in the presence of polyacrylamide. They reported that acrylamide polymer can be dissolved in water or electrolyte. Vereecken and Winand (1976) compared the influence of non-ionic and cationic polyacrylamides with Guar on the quality of copper deposits using "industrial" copper sulphate solution at 200 A/m^2 and 50 °C. The conclusion of this study was that the quality of the copper deposits obtained with Guar was always better than those obtained with both non-ionic and cationic polyacrylamides. The conditions under which these studies were conducted are outdated, therefore their results may not be applicable to the current EW commercial plant practice as described in Robinson et al. (2003).

In this paper the results of fractional factorial experimental designs are presented which aims to compare the efficacy of APAM and Guar in controlling surface roughness and dendrite formation. Fractional factorial

experimental designs are a variation of a basic experimental design in which only a subset of runs are systematically selected and conducted to minimize the number of experiments but include all the process variables (Montgomery, 2001). The experimental designs selected for this work use high and low levels of these variables, including Guar and APAM to closely replicate the industry-standard operating conditions of commercial copper EW.

The variables in commercial copper EW and ER are the flow rate of the feed electrolyte into the electrolytic cells containing fresh additives, electrolyte temperature, current density, and copper, sulfuric acid and chloride ion concentrations. Increasing the electrolyte flow rate into the electrolytic cell increases the velocity of the bulk electrolyte near the metal electrode/electrolyte interface and therefore may increase the forced convection and decrease the diffusion layer thickness, δ. In the experimental work described in this publication, the following studies were conducted to evaluate APAM against the industry standard Guar. (i) A fractional factorial experimental design was devised to evaluate whether APAM or Guar act independently or perform the same role. (ii) As APAM and Guar were found to have different roles, APAM and Guar were directly and separately compared in a Guar or APAM 2^2 experimental design at 6-hour EW time. (iii) As these tests indicated that APAM produces smoother copper deposits than Guar, APAM and Guar were further compared in *continuous* bench scale tests using parallel plate electrodes and commercial copper EW conditions.

2. Experimental

The testwork described below was designed to evaluate the effectiveness of APAM and Guar to control dendrite formation using the rotating cylinder electrode (RCE) and parallel plate electrodes (PPE) described by Fabian (2005) and Fabian et al. (2006b). The construction and characterization of the RCE is described elsewhere (Fabian, 2005, Fabian et al., 2006b). The RCE was used to conduct experimental design testwork at batch scale.

The electrolyte was prepared using AR grade copper sulfate and sulfuric acid and its composition throughout the testwork was as follows: Cu^{2+}=36 g/L, H_2SO_4=160 g/L and chloride ions=25 mg/L. 15 million Dalton polyacrylamide, Magnafloc® 800 HP, CIBA was prepared in 16-fold diluted electrolyte at 50 °C for 2 h under stirring conditions (Fabian et al., 2006b). Guarfloc®66 (Guar) from Cognis Corporation Mining Chemicals was prepared in water at 25 °C. The Guar concentration in the EW system used at the Mt. Gordon Operation in Australia was approximately 0.52 mg/L electrolyte or 175 g Guar/tonne copper cathode. This concentration was used as the low level factor in the experimental design and the high level was set at 1.0 mg/L electrolyte.

2.1. Experimental using an RCE

Table 2 shows two 2^{5-2} fractional factorial experimental designs. The factors at low level are common for both designs. The factors at high level differ in temperature only. The values of the diffusion layer thickness, δ were derived using the equation developed by Arvia and Carrozza (1962) and Fick (Newman and Thomas-Alyea, 2004), respectively, using Mathcad 12 (MathSoft Engineering and Education, 2004) and Fluent® as described in Fabian et al. (2006a). The low and high temperature levels of 45 °C and 65 °C were chosen to evaluate the behaviour of APAM at electrolyte temperatures similar to commercial copper EW and ER conditions, respectively. The organic additives, once dosed to the electrolyte, were subjected to 15 min mixing at 40 rpm and 5 min at 10 or 25 rpm before the

application of the desired current to the electrolytic cell. Therefore the total residence time of the organic additives in the electrolyte was 20 min in addition to the EW times at 45 °C, 50 °C or 65 °C±0.5 °C.

Table 2. Two 2^{5-2} fractional factorial experimental designs

Factors		Factor level		
		Low	High	
A	T (Temperature, °C)	45	55	65
B	I (Current density, A.m^{-2})	280	320	320
C	Guar, mg/L	0.5	1	1
D	APAM, mg/L	0.5	1	1
E	δ (Diff. Layer Thickness, μm)	87	108	110

The surface roughness was measured using a Mahr Perthometer M1 (Mahr, 2002) as described elsewhere (Fabian, 2005, Fabian et al., 2006b, Ilgar and O'Keefe, 1997). The surface roughness evaluation includes analysis of variance (ANOVA) and statistical inference procedures using Design-Expert® software (Stat-Ease, 2003, Fabian, 2005, Fabian et al., 2006b, Ilgar and O'Keefe, 1997, Barkey et al., 1989). The adequacy of the models was checked using residual analysis as described by Montgomery (2001) and Stat-Ease (2003).

The cross-section of the copper deposits was prepared for SEM examination. The samples were embedded in an epoxy resin and the cross-section cut with 600 grit silicon carbide powder. It was then sequentially polished with 3, 1 and 0.25 μm diamond paste. It was finally etched with a solution of 5 g of ferric chloride and 5 mL hydrochloric acid in 90 mL ethanol for 20–25 s. XRD data were collected from the copper deposits produced using a Siemens/Bruker General Area Detector Diffraction Solution, GADDS diffractometer and interpreted using the Scherrer equation (Fabian et al., 2003, Mathe et al., 2005).

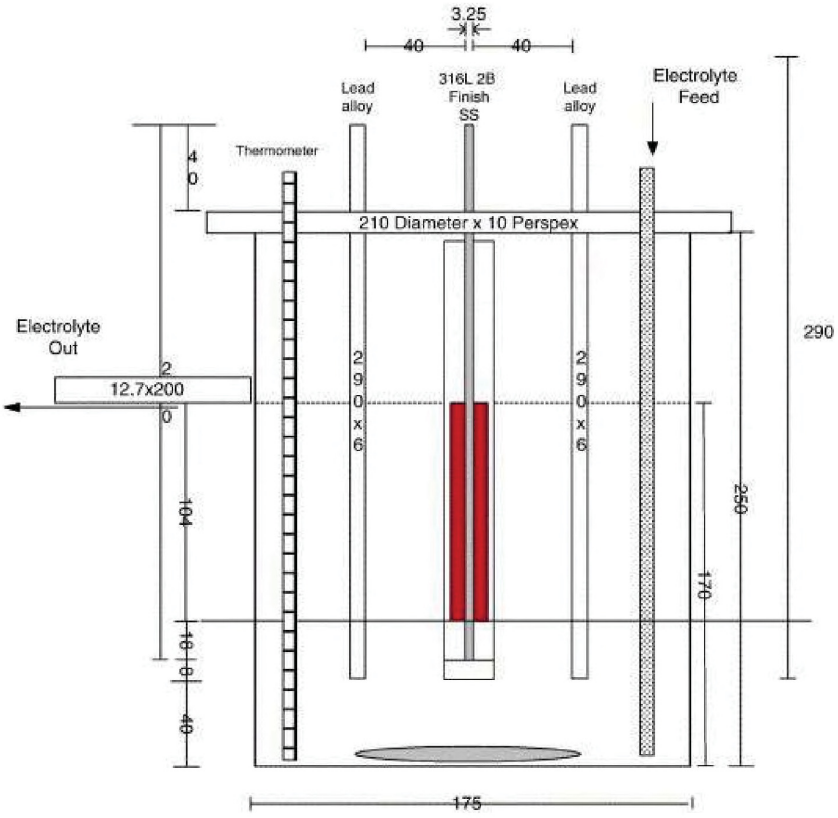
Guar was dosed *twice* and APAM was dosed *once* during this testwork unless otherwise stated. The first dose was added at the beginning and the second at approximately half EW time depending on the current density. The total electrowinning time was 4 h 21 min at a current density of 320 A/m^2 and 4 h 58 min at 280 A/m^2. The number of Coulombs applied was 500 C/cm^2.

2.2. Experimental using parallel plate electrodes

The comparison between Guar and APAM was also carried out using parallel plate electrodes at current-industry standard copper electrowinning operating conditions — except for current density which was increased to 340 A/m^2 from the industry standard of 280–300 A/m^2. (Robinson et al., 2003). Simultaneously, Guar and APAM concentrations were also increased from about 175 g/tonne copper cathode or 0.25–0.50 mg/L in the electrolyte (as was dosed at Mt. Gordon) to 200 g/tonne or 0.68 mg/L.

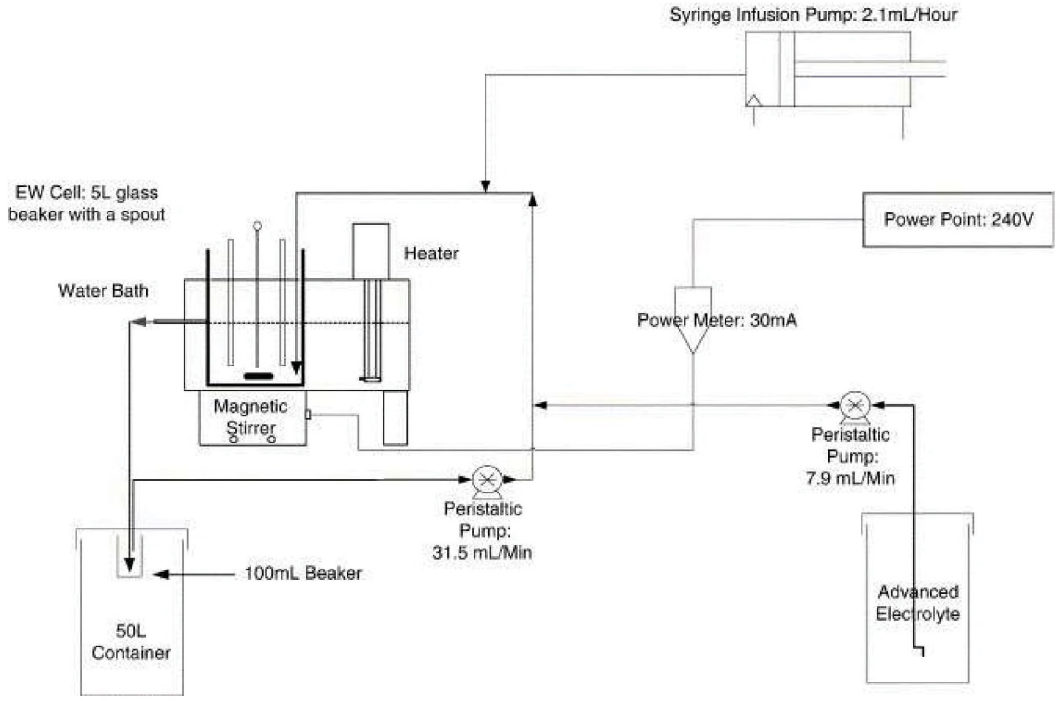
A 316L 2B finish stainless steel cathode with a surface roughness of 0.25±0.05 μm and a lead–alloy anode procured from Mt. Gordon Operations were cut to prepare the electrodes for this testwork. Current industry-standard ABS edge strips were inserted on the stainless steel and the corners were joined at 45° with Araldite K138 and hardener K138 Part B — an acid resistant and thermally stable epoxy resin. The stainless

steel substrates were thoroughly washed with acetone and water, soaked in an electrolyte solution for 24h and washed again with distilled water. The distance between the electrodes was 40mm, which is similar to the industry standard in copper EW. Fig. 2 shows the EW cell design in detail and Fig. 3 shows the overall bench scale design.



Download: Download full-size image

Fig. 2. EW cell design–parallel plate electrodes.



Download: Download full-size image

Fig. 3. Bench scale process.

Table 3 shows the details of the operating conditions for the bench scale experiments. The net electrolyte volume in the EW cell was 3.9L (without electrodes) and the flow rates of the re-circulating and advanced electrolyte were maintained constant at 31.5 and 7.9mL/min, respectively. Eighty percent of the total electrolyte flow rate was re-circulated to the EW cell using a Watson Marlow 505S peristaltic pump to simulate the commercial operation at Mt. Gordon. This recirculation maintains the activity of Guar or APAM constant in the EW cell and also possibly controls their ageing processes. The organic additives were dosed constantly at 2.1 mL/h using a syringe infusion pump. The concentration of the organic additive in the aliquot was 0.68mg/mL. The electrolyte in the EW cell was stirred with minimum agitation using a magnetic stirrer to improve the diffusion of the organic additive. The electrolyte temperature was kept at 50.5±0.5°C in a water bath.

Table 3. Bench scale experimental conditions

Current density, A/m^2	340
Voltage drop, V	2.15
EW iime, h	44.6
Deposition area (85.5×103.5mm), cm^2	88.5
Average copper concentration, g/L	35±1
Sulfuric acid concentration, g/L	160
Chloride ions concentration mg/L	25

Electrolyte net volume, L	3.9
Electrolyte temperature, °C	50.5±0.5
Guar or APAM, g/tonne copper cathode	200
Guar or APAM concentration in electrolyte, mg/L	0.68
Advanced electrolyte, mL/min	31.5
Recirculating electrolyte, mL/min	7.9
Syringe pump-dosing Guar or APAM, mL/h	2.1
Power to stir solution, (30mA), Watts	7–8
Copper concentration in advanced electrolyte, g/L	50
Sulfuric concentration in advanced electrolyte, g/L	142
Chloride concentration in advanced electrolyte, mg/L	30

3. Results and discussion

3.1. 2^{5-2} Experimental design results at 45°C–55°C

Table 4 presents the results indicating the effect of temperature (A), current density (B), Guar concentration (C), APAM concentration (D) and diffusion layer thickness (E) on surface roughness. The regression model obtained from this testwork is shown in Eq. (1). An F-value of 9.41 implies that the model is significant. There is only a 0.01% chance that the model F-value this large could occur due to noise. If the "Prob>F-value" (α) is very small (less than 0.05), then the terms in the model have a significant effect on the response (Montgomery, 2001, Stat-Ease, 2003).

$$\text{Surface Roughness}\,(\mu\text{m}) = +6.26 + 0.05{*}A + 0.27{*}B - 0.053{*}C - 0.056{*}D + 0.25{*}E - 0.62{*}B{*}C - 0.38{*}B{*}E \quad (1)$$

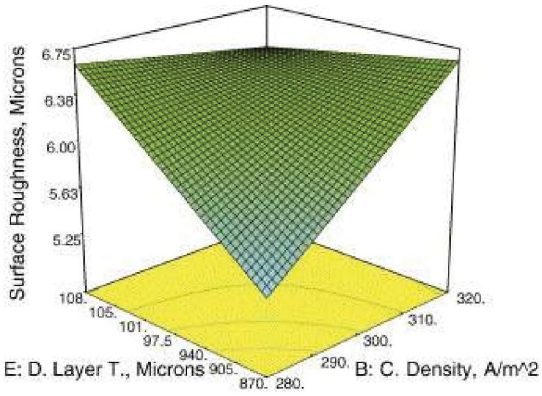
Table 4. 2^{5-2} Fractional factorial experimental results–temperature levels 45°C–55°C

	A	B	C	D=*A**B#*	*E=A**C#*	Mean surface roughness	S.D.
Run	Temperature	Current density	Guar	APAM	Diffusion layer thickness		
Standard	°C	mA/cm^2	mg/L	mg/L	µm	Ra, µm	
1	45	28	0.50	1.00	108	5.95	0.47
2	55	28	0.50	0.50	87	4.90	0.42
3	45	32	0.50	0.50	108	7.08	1.38
4	55	32	0.50	1.00	87	7.33	1.09
5	45	28	1.00	1.00	87	5.83	0.72

	A	B	C	D=*A***B*#	*E*=*A***C*#	Mean surface roughness	S.D.
Run	Temperature	Current density	Guar	APAM	Diffusion layer thickness		
Standard	°C	mA/cm^2	mg/L	mg/L	μm	Ra, μm	
6	55	28	1.00	0.50	108	7.31	1.08
7	45	32	1.00	0.50	87	5.99	0.66
8	55	32	1.00	1.00	108	5.71	0.68
CP	50	30	0.75	0.75	97.50	7.04	0.93

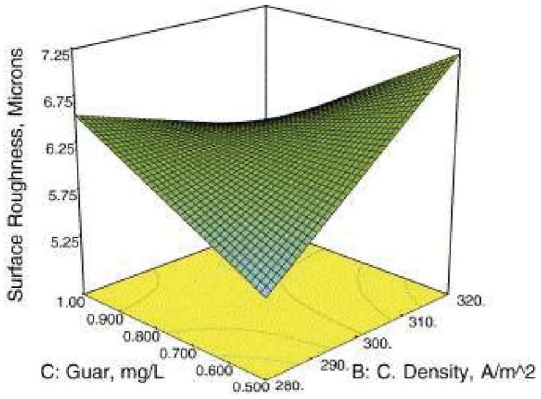
#Level of factors *D* and *E* were determined by the levels of *A***B* and *A***C*, respectively.

It can be seen that the surface roughness is strongly influenced by the current density *B*, (α=0.0180) and diffusion layer thickness *E*, (α=0.0247) as depicted in Fig. 4. Fig. 4 clearly indicates that at high rotational speed of the cylinder and low current density the smoothest surface roughness is achieved. In addition, it is also evident that the terms involving *B***C* (current density*Guar, α<0.0001), depicted in Fig. 5, significantly affect surface roughness. It can be seen that increasing the Guar concentration increases surface roughness at current densities lower than about 300A/m^2, a surprising result for an organic additive dosed to control dendrite formation. Moreover, it indicates that the surface roughness increases more steeply with an increase in the current density than with an increase in Guar concentration.



Download: Download full-size image

Fig. 4. The significant effect of diffusion layer thickness (*E*) and current density (*B*) on surface roughness in the temperature range of 45°C–55°C. The other variables are fixed at their centre point: *A*: temperature, 50°C; Guar, 0.75mg/L and *D*: APAM, 0.75mg/L.



Download: Download full-size image

Fig. 5. The significant effect of current density (*B*) and Guar (*C*) on surface roughness in the temperature range of 45°C–55°C. The other variables are fixed at their centre point: *A*: temperature, 50°C; *D*: APAM, 0.75mg/L and *E*: diffusion layer thickness, 97.5μm.

The effect of APAM was insignificant in this temperature range possibly due to the kinetics of its ageing in the electrolyte. The rationale for this conclusion is as follows. Cyclic voltammetry results (Fabian, 2005) indicate that at 45°C, a maximum polarization of APAM was obtained at about 3-hour residence time in the electrolyte whilst at 65°C it was obtained at about 1-hour residence time. It is therefore inferred that the first 3h of the EW tests at 45°C–55°C took place under sub-optimal adsorption/polarization conditions of APAM.

3.2. 2^{5-2} Experimental design results at 45°C–65°C

Table 5 presents the results indicating the effect of temperature (*A*), current density (*B*), Guar concentration (*C*), APAM concentration (*D*) and diffusion layer thickness (*E*) on surface roughness. The EW tests at this temperature range were also carried out for 4.35 and 4.97h (14,000C) as in the previous testwork. The model obtained from this testwork is shown in Eq. (2). An *F*-value of 2.06 implies that the model is significant and that there is a 6.3% chance that the model *F*-value this large could occur due to noise.

$$\text{Surface Roughness}\,(\mu\text{m}) = +6.16 - 0.051_{*}\,A - 0.089_{*}\,B - 0.075_{*}\,C - 0.41_{*}\,D + 0.23_{*}\,E - 0.17_{*}\,B_{*}\,C \quad (2)$$

Table 5. 2^{5-2} Fractional factorial experimental results–temperature levels 45°C–65°C

	A	B	C	D=*A***B*	*E*=*A***C*	Mean surface roughness	S.D.
Run	Temperature	Current density	Guar	PAM	Diffusion layer thickness		
Standard	°C	mA/cm^2	mg/L	mg/L	μm	Ra, μm	
1	45	28	0.50	1.00	110	5.95	0.47
2	65	28	0.50	0.50	87	6.36	0.64
3	45	32	0.50	0.50	110	7.08	1.38

	A	B	C	D=*A***B*	*E*=*A***C*	Mean surface roughness	S.D.
Run	Temperature	Current density	Guar	PAM	Diffusion layer thickness		
Standard	°C	mA/cm^2	mg/L	mg/L	μm	Ra, μm	
4	65	32	0.50	1.00	87	5.56	0.67
5	45	28	1.00	1.00	87	5.83	0.72
6	65	28	1.00	0.50	110	6.86	2.28
7	45	32	1.00	0.50	87	5.99	0.66
8	65	32	1.00	1.00	110	5.66	0.69

It can be seen from this model that APAM (D, α=0.0041) has the most significant effect on reducing surface roughness. Diffusion layer thickness (E, α=0.1004) has the next largest effect and an increase in E increases surface roughness as expected (Ilgar and O'Keefe, 1997). The aliased effect of current density (B) and Guar (C) are insignificant (B*C, α=0.2185). Current density B (α=0.5192), Guar C, (α=0.5855) and temperature A, (α=0.7129) are also insignificant. The regression analysis (Montgomery, 2001) indicates again that APAM and Guar are also not aliased and therefore confirms that APAM acts independently of Guar to reduce surface roughness. Therefore the effect of Guar and APAM on surface roughness was investigated separately, as described in the following Sections.

3.3. Effect of Guar or APAM over 6-hour EW at 50°C

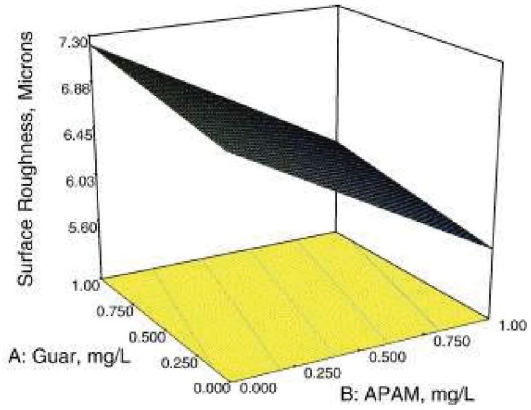
This test was conducted to continue evaluating the effectiveness of Guar or APAM, either alone or in combination, on surface roughness and on the number of Peaks-per Centimetre (PPC) over 6h of EW. PPC is defined as the number of roughness profile elements per centimetre which consecutively intersect at a specified upper profile section level and a lower profile section (Mahr, 2002). A surface profile can have the same surface roughness with a different number of PPC. Guar was dosed twice and APAM once. The electrolyte temperature, current density and δ were 50°C, 300A/m^2 and 109μm (10rpm), respectively. The experimental design and results are shown in Table 6. Eq. (3) shows the surface roughness model for this testwork where A is Guar concentration and B is APAM concentration.

$$\text{Surface Roughness}\,(\mu\text{m}) = 6.45 + 0.144_{*}\,A - 0.627_{*}\,B \tag{3}$$

Table 6. 6-hour EW time at 50°C: Guar-or-APAM

	Factors, mg/L		Surface roughness, μm		No. PPC		Dendrites
Run	*B* = APAM	*A* = Guar	Mean	S.D.	Mean	S.D.	Small needles
1	0	0	7.68	2.16	65.13	13.95	Numerous
2	0	1	6.48	0.70	87.63	8.35	Numerous nascents
3	1	0	6.42	0.27	82.75	8.24	None
4	1	1	6.71	0.36	83.38	7.46	None

The Model *F*-value of 2.58 for surface roughness implies the model shown in Eq. (3) is significant with a 9.37% chance that a "Model *F*-Value" this large could occur due to noise. APAM (B, α=0.0388) has a significant effect on reducing surface roughness and Guar (A, α=0.623) has an insignificant effect on increasing surface roughness as shown in Fig. 6.

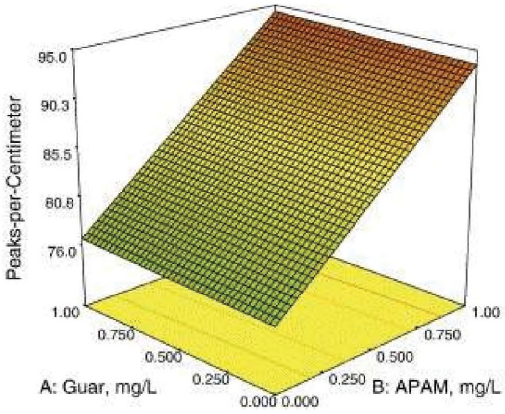


Download: Download full-size image

Fig. 6. The significant effect of APAM on surface roughness after 6-hour EW.

The number of PPC reported in Table 6 was also analysed to confirm the surface roughness results described above. The model for the PPC is presented in Eq. (4) and depicted in Fig. 7. The Model *F*-value of 8.85 for the number of PPC implies the model is significant with only a 0.11% chance that a "Model *F*-Value" this large could occur due to noise.

$$\mathbf{Number\ \ of\ \ Peaks-per-Centimetre} = 85.2 + 0.313_{*}\,A + 8.81_{*}\,B \tag{4}$$



Download: Download full-size image

Fig. 7. The significant effect of APAM on Peaks-per-Centimetre after 6-hour EW.

It is concluded from these results that APAM significantly reduced surface roughness and increased the number of PPC. In contrast, Guar increased the surface roughness and decreased the number of PPC similar

to the copper deposit produced without additives. Table 6 shows results and visual observations from the testwork. It can be seen that qualitatively, the formation of dendrites is reduced in the presence of APAM.

3.4. Effect of Guar or APAM in continuous bench scale tests

Bench scale testwork was aimed at verifying the effectiveness of Guar and APAM in controlling dendrite growth in a continuous copper EW system using *parallel plate* electrodes. The surface roughness of the copper deposits was unable to be measured since it surpassed the specifications of the M1 Perthometer (10nm–100μm). Photographs of the electrowon copper deposits in the presence of Guar and APAM are shown in Fig. 8, Fig. 9, respectively. It can be seen that the physical appearance of copper deposit obtained with Guar was rougher than that obtained with APAM. Both sides of the deposit produced with Guar have a needle-like, granular appearance throughout the plate. In contrast, the deposit produced with APAM is smoother, brighter and more compact than the copper deposit produced with Guar. Moreover, the copper deposits obtained with Guar possess three areas where copper deposition has not taken place. This is described as "lacy" copper deposit and was also reported by Sun and O'Keefe (1992) in the absence of additives. This kind of deposit is often found at commercial scale electrowinning operations but not at ER operations where animal glue and thiourea are used as organic additives. The brightening effect of the copper deposit in the presence of APAM was probably achieved through large crystal faces that are parallel to the substrate.



Download: Download full-size image

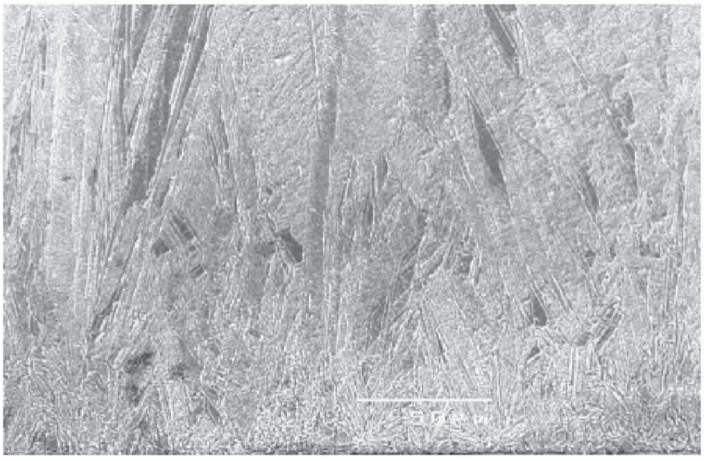
Fig. 8. Copper deposit obtained with Guar at 340A/m^2 and 44h and 35min.



Download: Download full-size image

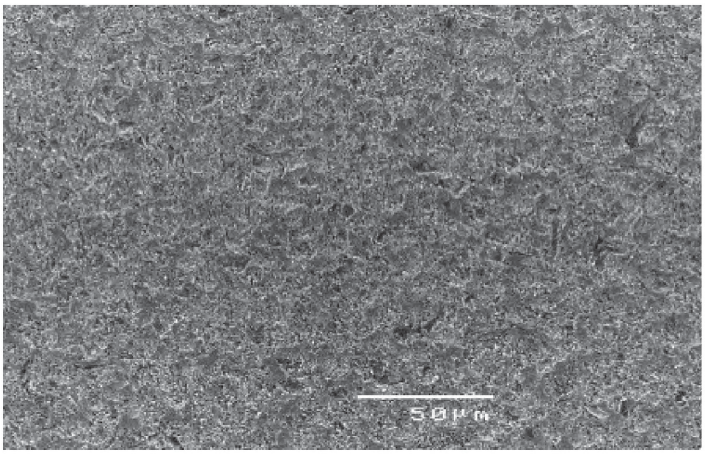
Fig. 9. Copper deposit obtained with APAM at 340A/m^2 and 44h and 35min.

Fig. 10, Fig. 11 are SEM micrographs of the cross-sectioned copper cathodes obtained from this testwork. It can be seen in Fig. 10 that the cross section of the copper cathode obtained with APAM exhibits columnar growth. It has been reported that this type of growth may be improved into an equiaxial microstructure by adding a sulfur bearing organic additive into the electrolyte bath (Plieth, 1992). In contrast, in the presence of Guar, the microstructure of the copper deposit is *porous* (Fig. 11).



Download: Download full-size image

Fig. 10. SEM micrographs of copper deposit obtained using 0.68mg/L APAM (200g/tonne Copper Cathode) at 340A/m^2 current density. Note the slightly fibrous or columnar structure.



Download: Download full-size image

Fig. 11. SEM micrographs of copper deposit obtained using 0.68 mg/L Guar (200 g/tonne Copper Cathode) at 340 A/m^2 current density. Note a porous copper cathode.

Crystallite size was also determined using an XRD technique, General Area Diffraction Detector Solution (GADDS), according to the technique described elsewhere (Fabian et al., 2003). The crystallite size was determined to assess whether the presence of APAM or Guar results in higher nucleation rates during EW under otherwise constant conditions. These tests may also be important to determine coalescence of small crystallite sizes to form larger crystal sizes according to the mechanism of 3D crystallite size growth.

Table 7 shows the Kruskal–Wallis test results for APAM and Guar crystallite size obtained from the bench scale testwork using parallel plate electrode. The median crystallite size with APAM (405 Å) is slightly smaller than with Guar (427 Å). Therefore APAM appears to favour a higher nucleation rate than Guar. The other important results are the 41% crystallite size greater than 1800 Å: for APAM and 24% for Guar. The inferred crystallite size decreases as the full width at half-maximum (FWHM) of the copper deposit sample increases (Klug and Alexander, 1974). If the FWHM of the sample is smaller than that of the LaB_6 standard, the crystallite size is not processed and is reported as greater than 1800 Å. These calculations therefore appear to indicate that nucleation rates, 3D crystallite growth, and coalescence is higher with APAM than with Guar.

Table 7. Kruskal–Wallis test results for APAM and Guar crystallite size

Test no.	APAM	Guar
Electrowinning Time, h	44.60	44.60
FWHM number of readings, N	338	440
Crystallite size data processed, N	198	335
Crystallites size >1800 Å, %	41	24
Kruskal–Wallis crystallite size mean rank	220	295
Asymptotic significance	0.000	

Test no.	APAM	Guar
Median crystallite size, Å	405	427

Bench-scale continuous electrowinning tests using parallel plate electrodes where APAM and Guar were dosed continuously and independently also indicated that APAM produces smoother deposits than Guar. The overall results suggest that APAM is more specifically adsorbed than Guar at the metal electrode/electrolyte interface where high electrical fields are convergent. This behaviour can therefore inhibit the formation of protrusions/dendrites. The covalent bonding that polyacrylamide block polymer confers at the metal/electrolyte interface (Halverson et al., 1985, Panzer and Halverson, 1988, Panzer et al., 1984) probably plays an important role for APAM to be more specifically adsorbed than Guar.

The adsorption properties for Guar were not found in the literature. The difference on inhibition (polarization) and adsorption produced by Guar and APAM has been studied by us using Cyclic Voltammetry and Electrochemical Impedance Spectroscopy (Fabian, 2005) and will be discussed in subsequent papers.

4. Conclusions

It was found that when 14,000C were applied in the fractional factorial experimental design that the effect of APAM was significant in reducing surface roughness at 65 °C but insignificant at 45 °C. This difference is attributed to stronger adsorption and enhanced polarization of APAM at 65 °C. The regression models from this experimental design indicated that APAM and Guar are not aliased and that APAM acts truly independently of Guar. It was also found that current density and Guar were aliased but decreases in significance with increasing temperature consistent with the faster degradation of Guar. Therefore, the role of Guar and APAM was concluded to be independent. In the 6-hour EW tests, APAM significantly reduced surface roughness and increased the number of Peaks-per-Centimetre.

Bench-scale continuous electrowinning tests where APAM and Guar were dosed continuously and independently indicated that APAM produces smoother deposits than Guar. SEM examination of cross sections of the copper deposits showed that Guar produced porous deposits and APAM produced slightly columnar deposits. Furthermore, the copper deposit with APAM is brighter and has greater amounts of both smaller and larger crystallite sizes than those with Guar. We infer that presence of APAM favours higher nucleation rates and greater 3D crystallite growth and coalescence than Guar and that APAM can produce purer copper deposits since voids and porosity can be reduced by smaller crystallites.

The overall results of this work indicate that APAM produces smoother, brighter and more compact copper electrodeposits than Guar. Therefore APAM can be viewed as a potential new levelling and brightening agent for copper electrometallurgy.

Acknowledgments

We wish to thank Mount Gordon Operations of Western Metals Copper Ltd. and to the Australian Research Council for funding this study.

Recommended articles

References

Arvia and Carrozza, 1962 A.J. Arvia, J.S.W. Carrozza

Mass transfer in the electrolysis of $CuSO_4$–H_2SO_4 in aqueous solutions under limiting current and forced convection employing a cylindrical cell with rotating electrodes

Electrochimica Acta, 7 (1962), pp. 65-78

View PDF View article View in Scopus ↗ Google Scholar ↗

Barkey et al., 1989 D. Barkey, R. Muller, C. Tobias

Roughness development in metal electrodeposition I. Experimental results

Journal of the Electrochemical Society, 138 (8) (1989), pp. 2199-2207

Crossref ↗ View in Scopus ↗ Google Scholar ↗

Budevski et al., 1996 E. Budevski, G. Staikov, W. Lorenz

Electrochemical Phase Formation and Growth — an Introduction to the Initial Stages of Metal Deposition

VCH, New York (1996)

Google Scholar ↗

Fabian, 2005 Fabian, C., 2005. Copper electrodeposition in the presence of guar or activated polyacrylamide. PhD Thesis, James Cook University, Australia.

Google Scholar ↗

Fabian et al., 2003 C. Fabian, M. Ridd, S. Ness, T. Lancaster, G. Griffin

Determination of crystallite size and surface roughness of copper deposits for electrowinning in the presence of an organic additive

C.A. Young, C.G. Anderson, D.B. Dreisinger, B. Harris, A. James (Eds.), Hydrometallurgy, The Minerals Metals and Materials Society (TMS), Warrendale (2003), pp. 1233-1245

Crossref ↗ View in Scopus ↗ Google Scholar ↗

Fabian et al., 2006a C. Fabian, P. Mandin, M.J. Ridd, M. Sheehan

Hydrodynamic modelling of copper electrodeposition at a vertical rotating cylinder electrode

R. Woods, F.M. Doyle, G.H. Kelsall (Eds.), Electrochemistry in Mineral and Metal Processing VII, The Electrochemical Society Inc., Denver, CO (2006), pp. 303-315

Crossref ↗ View in Scopus ↗ Google Scholar ↗

Fabian et al., 2006b C. Fabian, M.J. Ridd, M.E. Sheehan

Rotating cylinder electrode study of the effect of activated polyacrylamide on surface roughness of electrodeposited copper

Hydrometallurgy, 84 (3–4) (2006), pp. 256-263

View PDF View article View in Scopus ↗ Google Scholar ↗

Halverson et al., 1985 F. Halverson, J. Lancaster, M. O'Connor

Sequence distribution of carboxyl groups in hydrolyzed polyacrylamide

Macromolecules, 18 (6) (1985), pp. 1139-1144

Crossref ↗ View in Scopus ↗ Google Scholar ↗

Ilgar and O'Keefe, 1997 E. Ilgar, T. O'Keefe

Surface roughening of electrowon copper in the presence of chloride ions

D. Dreisinger (Ed.), Aqueous Electrotechnologies: Progress in Theory and Practice, The Minerals Metals and Materials Society (TMS), Warrendale (1997), pp. 51-62

View in Scopus ↗ Google Scholar ↗

Klug and Alexander, 1974 H. Klug, L. Alexander

X-ray Diffraction Procedures for Polycrystalline and Amorphous Materials

John Wiley & Sons, Sydney (1974)

Google Scholar ↗

Langner et al., 1989 B.E. Langner, P. Stantke, E.F. Reinking

Method of Measuring the Effective Inhibitor Concentration During a Deposition Process of Metal from Aqueous Electrolytes and Test Apparatus Therefore, Norddeutsche Affinerie Aktiengesellschaft, Hamburg, DE (1989), p. 11

Google Scholar ↗

Mahr, 2002 Mahr

M1 Mahr Perthometer Operating Manual

(2002)

Google Scholar ↗

Mark et al., 1969 H. Mark, N. Gaylord, N. Bikales

Encyclopedia of Polymer Science and Technology, vol. 11, Wiley-Interscience, New York (1969), pp. 401-420

Mathe et al., 2005 M.K. Mathe, S.M. Cox, V. Venkatasamy, U. Happek, J.L. Stickney

Formation of HgSe thin films using electrochemical atomic layer epitaxy

Journal of the Electrochemical Society, 152 (11) (2005), pp. C751-C755

Crossref ↗ View in Scopus ↗ Google Scholar ↗

MathSoft Engineering and Education, I, 2004 MathSoft Engineering and Education, I

Mathcad (2004)

Google Scholar ↗

Montgomery, 2001 D.C. Montgomery

Design and Analysis of Experiments

John Wiley & Sons (2001)

Google Scholar ↗

Newman and Thomas-Alyea, 2004 J. Newman, K.E. Thomas-Alyea

Electrochemical Systems

John Wiley & Sons, Inc., Hoboken, New Jersey (2004)

Google Scholar ↗

Panzer and Halverson, 1988 H. Panzer, F. Halverson

Blockiness in hydrolyzed polyacrylamide

B. Moudgil, B. Scheiner (Eds.), Flocculation Dewatering, Proc. Eng. Found. Conf., Florida, Eng. Found., New York, N.Y (1988), pp. 239-249

Google Scholar ↗

Panzer et al., 1984 H. Panzer, F. Halverson, J. Lancaster

Carboxyl sequence distribution in hydrolyzed polyacrylamide

Polymeric Materials Science and Engineering, 51 (1984), pp. 268-271

View in Scopus ↗ Google Scholar ↗

Plieth, 1992 W. Plieth

Additives in the electrocrystallization process

Electrochimica Acta, 37 (12) (1992), pp. 2115-2121

View PDF View article View in Scopus ↗ Google Scholar ↗

Pye and Schurz, 1957 Pye, D., Schurz, G., 1957. Electrowinning of metals, U.S.Patent 2,798,040. The Dow Chemical Company.

Google Scholar ↗

Robinson et al., 2003 T. Robinson, W.G. Davenport, J. Quinn, G. Karkas

Electrolytic copper refining — 2003 world tankhouse operating data

J.E. Dutrizac, C.G. Clement (Eds.), Proc. Copper 2003–Cobre 2003, Santiago, Chile, Canadian Institute of Mining, Metallurgy and Petroleum, Montreal (2003), pp. 3-66

View in Scopus ↗ Google Scholar ↗

Stantke, 1999 P. Stantke

Guar concentration measurement with the Collamat system

J. Dutrizac, J. Ji, V. Ramachandran (Eds.), Proc. Copper 99–Cobre 99, vol. 3, Minerals, Metals and Materials Society, Warrendale, PA (1999), pp. 643-651

View in Scopus ↗ Google Scholar ↗

Stat-Ease, 2003 S.M.E. Stat-Ease

Design-Expert Software

John Wiley & Sons, Inc. (2003)

Google Scholar ↗

Sun and O'Keefe, 1992 M. Sun, T. O'Keefe

The effect of additives on the nucleation and growth onto stainless steel cathodes

Metallurgical Transactions. B, Process Metallurgy, 23B (1992), pp. 591-599

View in Scopus ↗ Google Scholar ↗

Vereecken and Winand, 1976 J. Vereecken, R. Winand

Influence of polyacrylamides on the quality of copper deposits from acidic copper sulphate solutions

Surface Technology, 4 (1976), pp. 227-235

View PDF View article View in Scopus ↗ Google Scholar ↗

Vereecken et al., 2005 P.M Vereecken, R.A Binstead, H. Deligianni, P.C. Andricacos

The chemistry of additives in damascene copper plating

IBM Journal of Research and Development, 49 (1) (2005), pp. 3-19

Crossref ↗ View in Scopus ↗ Google Scholar ↗

Cited by (22)

Industrial perspectives for electrochemical extraction of metals from primary and secondary resources

2024, Inorganic Chemistry Communications

Show abstract

High-strength copper foil prepared with 2-mercaptothiazoline by direct current electrodeposition

2023, Electrochimica Acta

Show abstract

Evaluating the effect of molecular properties of polyacrylamide reagents on deposit growth in copper electrowinning

2020, Hydrometallurgy

> *Citation Excerpt :*
>
> ...The effectiveness of polyacrylamides is attributed to their specific adsorption on metal surfaces. Adsorption occurs via hydrogen bonds through amide groups in the double layer at the interface resulting in control of lateral and vertical copper growth on the cathode face (Broseta and Medjahed, 1995; Fabian et al., 2007; Grchev et al., 1991). The result is an evenly distributed deposit growth, which is unlike the polysaccharide Guar gum which does not specifically adsorb (Fabian et al., 2007)....

Show abstract

Continuous electrolytic refining process of cathode copper with non-dissolving anode

2019, Minerals Engineering

> *Citation Excerpt :*
>
> ...Second, chemical factors must be improved, such as electrolyte and additives, which are commonly used as additives for gelatin, thiourea, casein, and chloride (Gladysz et al., 2007). Fabian et al. (2007) found that the surface of copper was smooth and the copper grains were columnar with the use of polyacrylamide, whereas the cathode copper was porous with guar gum. Quinet et al. (2009) found that thiourea played a role in refining the grains of the cathode copper....

Show abstract

The effects of Zn²⁺ and Polyacrylamide (PAM) on the electrodeposition of manganese from non-selenium sulfate solutions

2018, International Journal of Electrochemical Science

Show abstract

The effect of gold on anode passivation and high current density operation under simulated silver electrorefining conditions

2016, Hydrometallurgy

Citation Excerpt :

...Refining of silver and gold as products from gold mining or the smelting of copper anode slime, is often the final process of these metal production processes (Shi and Ye, 2013; Bard and Sobral, 2008). Although there has been a significant number of studies into many aspects of the copper electrorefining processes including the effect of current density (Dabroś and Jaskula, 1978; Ntengwe et al., 2010), temperature (Owais et al., 2015), additives (Ojaghi Ilkhchi et al., 2007; Fabian et al., 2007), anode slime formation (Kilviluoma et al., 2016; Chen and Dutrizac, 2004; Chen and Dutrizac, 2008) and the presence of impurities (including silver, antimony, arsenic, bismuth) (Kucharska-Giziewicz and Mackinnon, 1996; Minotas et al., 1989; Hiskey and Maeda, 2003), in comparison, the electrorefining of silver has so far received less attention (Habashi, 1980; Ammen, 1984; Pophanken and Friedrich, 2015; Auerswald and Radcliffe, 2005). From the binary diagram of silver and gold, it can be seen that both metals will form a single phase solid throughout the mass fraction (Okamoto and Massalski, 1983)....

Show abstract

View all citing articles on Scopus

View Abstract

Copyright © 2006 Elsevier B.V. All rights reserved.

ELSEVIER

All content on this site: Copyright © 2024 Elsevier B.V., its licensors, and contributors. All rights are reserved, including those for text and data mining, AI training, and similar technologies. For all open access content, the Creative Commons licensing terms apply.

RELX™

APPENDIX FABIAN02

Available online at www.sciencedirect.com
ScienceDirect
Hydrometallurgy 86 (2007) 44–55
hydrometallurgy
www.elsevier.com/locate/hydromet

Assessment of activated polyacrylamide and guar as organic additives in copper electrodeposition

C.P. Fabian [a,b,*], M.J. Ridd [b], M.E. Sheehan [a]

[a] Department of Chemical Engineering, School of Engineering, James Cook University, Townsville, QLD., 4811 Australia
[b] Department of Chemistry, School of Pharmacy and Molecular Sciences, James Cook University, Townsville, QLD., 4811 Australia

Received 3 August 2006; received in revised form 7 November 2006; accepted 8 November 2006
Available online 19 December 2006

Abstract

The effect of current density, temperature, diffusion layer thickness (δ), deposition time, Guarfloc66 (Guar) and activated polyacrylamide (APAM) on the topography (surface roughness) of electrodeposited copper was studied. The level of these variables approximates current commercial copper electrowinning (EW) and electrorefining (ER) operating conditions. The effect of Guar and APAM on surface roughness and number of Peaks-per-Centimeter was assessed both in combination and alone using a rotating cylinder electrode (RCE) for up to 6-hour EW time. Observed effects on surface roughness indicate that a more uniform surface and lower roughness/smoother copper deposits were obtained using the additive APAM rather than Guar. Regression models indicate APAM has a significant effect on reducing surface roughness at 65 °C.

Bench-scale *continuou*s electrowinning tests were carried out at 50 °C for 44.6 h using parallel plate electrodes into which APAM and Guar were dosed continuously and independently. These tests also indicated that APAM produces smoother deposits than Guar. The cross sections of the copper deposits from these tests showed that APAM exhibits a *slightly columnar* copper deposit and Guar produced a *porous* copper deposit. The copper deposit produced with additive APAM was brighter and produced greater amounts of both smaller and larger crystallite sizes than those obtained with Guar. This infers that APAM favours higher nucleation rates and greater 3D crystallite growth and coalescence than Guar.
© 2006 Elsevier B.V. All rights reserved.

Keywords: Copper; Electrodeposition; Electrowinning; Electrorefining; Polyacrylamide; Rotating cylinder electrode; Guar; Surface roughness; Statistical analysis

1. Introduction

In the copper deposition industry in general, organic additives and chloride ions need to be dosed to produce smooth deposits, free of voids or porosity. It is also known that organic additives significantly influence the current–potential relationship due to their competition for surface coverage with the components of the electrolyte system including chloride ions. Therefore these organic additives must be carefully selected according to their role at the metal/electrolyte interface to control the nucleation and growth during the deposition process. Table 1 summarizes the industry-standard additives used in copper EW, ER and in the damascene process for micro-electronics industry. Table 1 shows the typical concentration of these organic additives in

* Corresponding author. Department of Chemical Engineering, School of Engineering, James Cook University, Townsville, QLD., 4811 Australia. Tel.: +61 2 9717 7067; fax: +61 2 9543 7179.
E-mail addresses: cfabian2@bigpond.net.au, ces.fabian@ansto.gov.au (C.P. Fabian).

0304-386X/$ - see front matter © 2006 Elsevier B.V. All rights reserved.
doi:10.1016/j.hydromet.2006.11.002

the electrolyte bath and their respective roles. An electrode is polarized when, under constant experimental conditions, the potential in the presence of an additive, e.g., animal glue, PEG, is more negative than the potential without the additive. An electrode is depolarized when the potential in the presence of an additive, e.g., chloride ions, is less negative. The polarizer/inhibitor/leveller controls the vertical growth to produce smooth deposits by conferring preferential adsorption on the peaks or active sites. The grain refiner/accelerator may predominantly control the nucleation process or promote the formation of new nuclei to possibly form new crystallites at the recesses (Vereecken et al., 2005). This synergistic process between the inhibitor and grain refiner is aimed at improving the overall quality of the copper deposit: purity, smoothness and plant productivity i.e., elimination/reduction of short-circuits caused by dendrites.

The first step of metal deposition is the formation of nuclei of the depositing metal on a foreign substrate and on a substrate of the same metal. The structure of the first monolayer(s), has an impact on the deposition of further layers and therefore on the morphology of the deposited metal. The competition between nucleation and growth determines the smoothness of the deposit: the higher the nucleation rate; the finer the crystal size (Budevski et al., 1996). Moreover, the forms of the growing crystals determine their physical appearance and structure. A higher crystal size growth rate, normal to the substrate, leads to a more fibrous/columnar structure. A brightening effect can be achieved when large developed crystal faces grow parallel to the substrate (Budevski et al., 1996).

It has been shown elsewhere (Fabian, 2005; Fabian et al., 2006b) that a rotating cylinder electrode (RCE) may be applied as a novel method of determining the effect of the preparation media of polyacrylamide (PAM) on the surface roughness of electrodeposited copper. It has been shown that when a high molecular weight PAM (MW 15 million Dalton) is prepared in 16-fold diluted copper electrolyte at 50 °C for 2 h and dosed into an EW cell, the electrodeposited copper had a significantly lower mean surface roughness than was the case when polyacrylamide was prepared in water or full-strength electrolyte or alkaline solution. The hydrolysis of PAM in pH 2 solutions is reported to produce a block copolymer (Halverson et al., 1985; Panzer and Halverson, 1988; Panzer et al., 1984). The PAM hydrolysed in 16-fold diluted copper electrolyte (pH 1.5) was named 'activated polyacrylamide' (APAM). It has been also shown that APAM also produced deposits exhibiting a lower surface roughness than polyacrylic acid (Fabian, 2005).

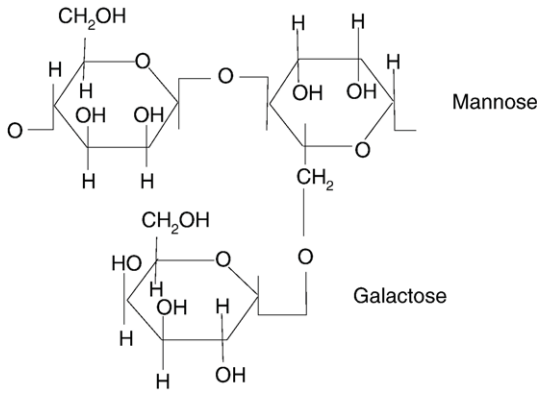


Fig. 1. The chemical structure of Guar based on Mark et al. (1969).

Guar is a naturally occurring galacto-mannan polymer, a polysaccharide, used as flocculant and coagulant with typical molecular weights ranging from 200,000 to 500,000 Da. Guar is a linear D-mannose sugar with a D-galactose sugar chain on every other mannose as shown below, Fig. 1 (Mark et al., 1969). Guar is the industry-standard organic additive used in copper EW as a weak levelling agent for about 40 years to produce bright copper deposits (Langner et al., 1989; Stantke, 1999).

Pye and Schurz (1957) patented the electrowinning of zinc and copper in the presence of polyacrylamide. They reported that acrylamide polymer can be dissolved in water or electrolyte. Vereecken and Winand (1976) compared the influence of non-ionic and cationic

Table 1
Industry-standard additives used in copper electrometallurgy

Role of the additive	Electrorefining		Electrowinning		Micro-electronics, PCB and IC	
	Additive	mg/L	Additive	mg/L	Additive	mg/L
Leveller	Glue	1	Nil	Nil	PEG* and JGB	100–300 and 1
Brightener**			Guar	0.25–5		
Grain refiner***	Thiourea	2	Nil	Nil	SPS/MPSA	1/1
Depolarizer	Cl^-	50–60	Cl^-	20–25	Cl^-	40–60

*PEG, polyethylene glycol; SPS, bis(3-sulfo-propyl) disulfide; JGB, Janus Green B (safranine dye); MPSA, 3-mercapto-1-propanesulfinate. **Guar is also known as weak polarizer in the industry. ***Grain refiner or accelerator.

Table 2
Two 2^{5-2} fractional factorial experimental designs

Factors		Factor level		
		Low	High	
A	T (Temperature, °C)	45	55	65
B	I (Current density, $A.m^{-2}$)	280	320	320
C	Guar, mg/L	0.5	1	1
D	APAM, mg/L	0.5	1	1
E	δ (Diff. Layer Thickness, μm)	87	108	110

polyacrylamides with Guar on the quality of copper deposits using "industrial" copper sulphate solution at 200 A/m^2 and 50 °C. The conclusion of this study was that the quality of the copper deposits obtained with Guar was always better than those obtained with both non-ionic and cationic polyacrylamides. The conditions under which these studies were conducted are outdated, therefore their results may not be applicable to the current EW commercial plant practice as described in Robinson et al. (2003).

In this paper the results of fractional factorial experimental designs are presented which aims to compare the efficacy of APAM and Guar in controlling surface roughness and dendrite formation. Fractional factorial experimental designs are a variation of a basic experimental design in which only a subset of runs are systematically selected and conducted to minimize the number of experiments but include all the process variables (Montgomery, 2001). The experimental designs selected for this work use high and low levels of these variables, including Guar and APAM to closely replicate the industry-standard operating conditions of commercial copper EW.

The variables in commercial copper EW and ER are the flow rate of the feed electrolyte into the electrolytic cells containing fresh additives, electrolyte temperature, current density, and copper, sulfuric acid and chloride ion concentrations. Increasing the electrolyte flow rate into the electrolytic cell increases the velocity of the bulk electrolyte near the metal electrode/electrolyte interface and therefore may increase the forced

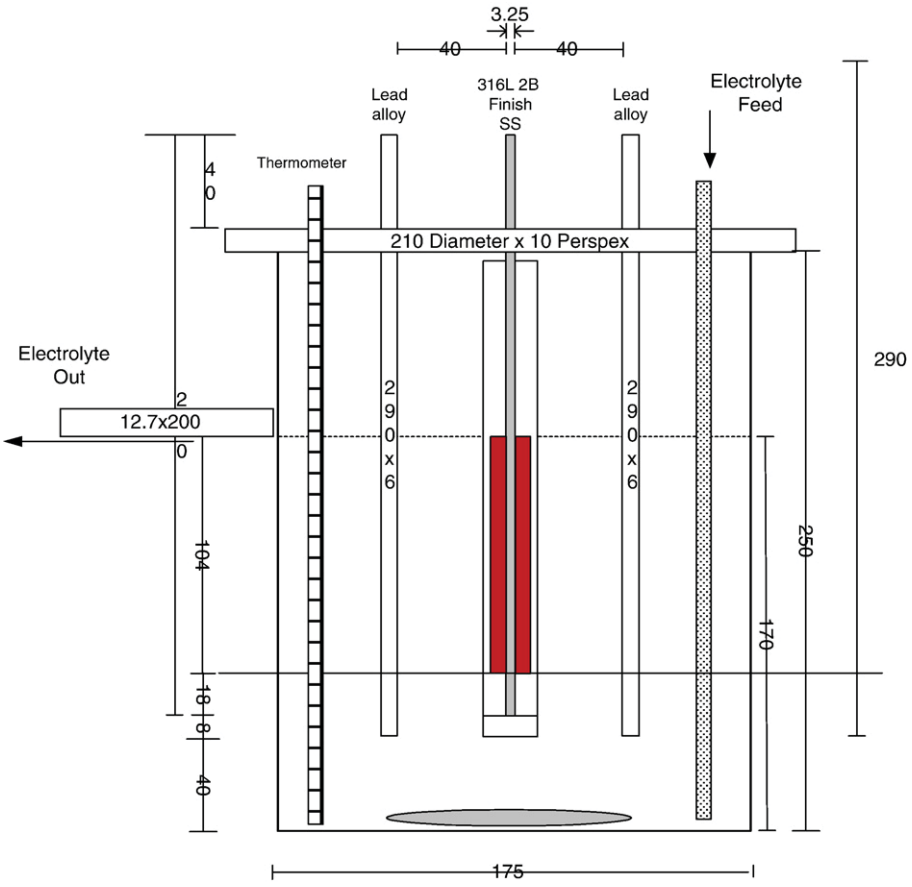


Fig. 2. EW cell design–parallel plate electrodes.

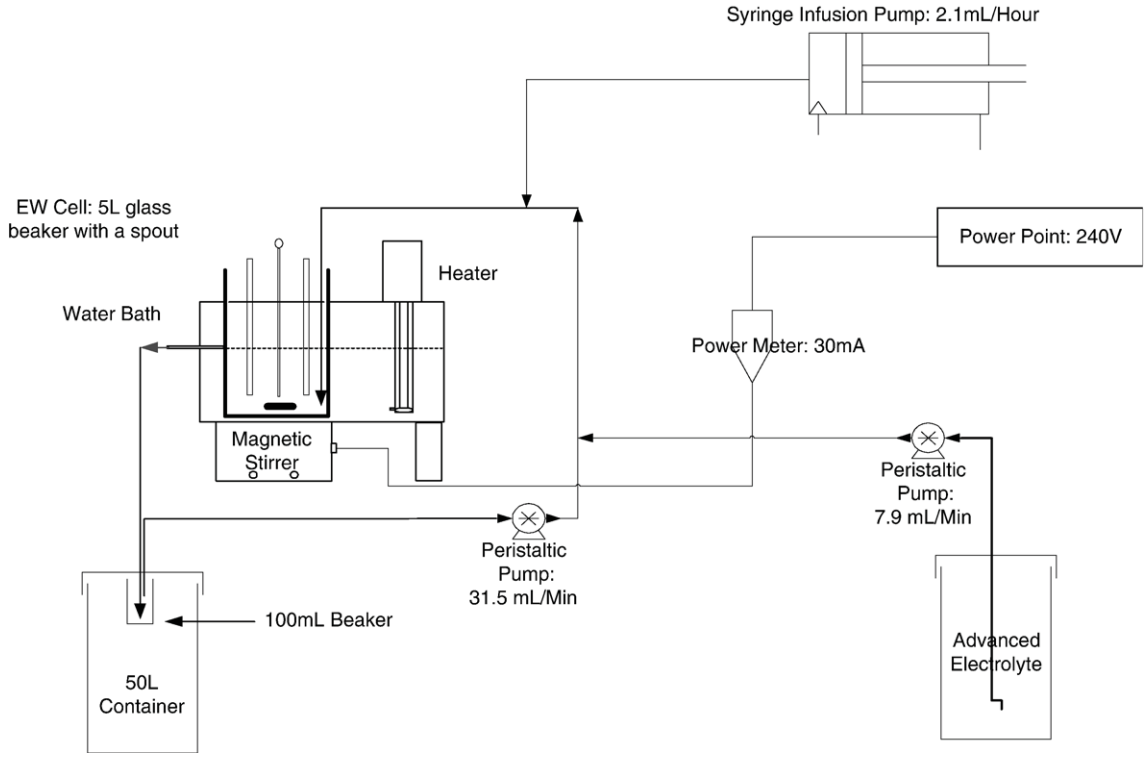


Fig. 3. Bench scale process.

convection and decrease the diffusion layer thickness, δ. In the experimental work described in this publication, the following studies were conducted to evaluate APAM against the industry standard Guar. (i) A fractional factorial experimental design was devised to evaluate whether APAM or Guar act independently or perform the same role. (ii) As APAM and Guar were found to have different roles, APAM and Guar were directly and separately compared in a Guar or APAM 2^2 experimental design at 6-hour EW time. (iii) As these tests indicated that APAM produces smoother copper deposits than Guar, APAM and Guar were further compared in *continuous* bench scale tests using parallel plate electrodes and commercial copper EW conditions.

2. Experimental

The testwork described below was designed to evaluate the effectiveness of APAM and Guar to control dendrite formation using the rotating cylinder electrode (RCE) and parallel plate electrodes (PPE) described by Fabian (2005) and Fabian et al. (2006b). The construction and characterization of the RCE is described elsewhere (Fabian, 2005; Fabian et al., 2006b). The RCE was used to conduct experimental design testwork at batch scale.

The electrolyte was prepared using AR grade copper sulfate and sulfuric acid and its composition throughout the testwork was as follows: Cu^{2+}=36 g/L, H_2SO_4=160 g/L and chloride ions=25 mg/L. 15 million Dalton polyacrylamide, Magnafloc® 800 HP, CIBA was prepared in 16-fold diluted electrolyte at 50 °C for 2 h under stirring conditions (Fabian et al., 2006b). Guarfloc®66 (Guar) from Cognis Corporation Mining Chemicals was prepared in water at 25 °C. The Guar concentration in the EW system used at the Mt. Gordon Operation in Australia was approximately 0.52 mg/L electrolyte or 175 g Guar/tonne copper cathode. This concentration was used as the low level factor in the experimental design and the high level was set at 1.0 mg/L electrolyte.

2.1. Experimental using an RCE

Table 2 shows two 2^{5-2} fractional factorial experimental designs. The factors at low level are common for both designs. The factors at high level differ in temperature only. The values of the diffusion layer

thickness, δ were derived using the equation developed by Arvia and Carrozza (1962) and Fick (Newman and Thomas-Alyea, 2004), respectively, using Mathcad 12 (MathSoft Engineering and Education, 2004) and Fluent® as described in Fabian et al. (2006a). The low and high temperature levels of 45 °C and 65 °C were chosen to evaluate the behaviour of APAM at electrolyte temperatures similar to commercial copper EW and ER conditions, respectively. The organic additives, once dosed to the electrolyte, were subjected to 15 min mixing at 40 rpm and 5 min at 10 or 25 rpm before the application of the desired current to the electrolytic cell. Therefore the total residence time of the organic additives in the electrolyte was 20 min in addition to the EW times at 45 °C, 50 °C or 65 °C±0.5 °C.

The surface roughness was measured using a Mahr Perthometer M1 (Mahr, 2002) as described elsewhere (Fabian, 2005; Fabian et al., 2006b, Ilgar and O'Keefe, 1997). The surface roughness evaluation includes analysis of variance (ANOVA) and statistical inference procedures using Design-Expert® software (Stat-Ease, 2003; Fabian, 2005; Fabian et al., 2006b, Ilgar and O'Keefe, 1997; Barkey et al., 1989). The adequacy of the models was checked using residual analysis as described by Montgomery (2001) and Stat-Ease (2003).

The cross-section of the copper deposits was prepared for SEM examination. The samples were embedded in an epoxy resin and the cross-section cut with 600 grit silicon carbide powder. It was then sequentially polished with 3, 1 and 0.25 μm diamond paste. It was finally etched with a solution of 5 g of ferric chloride and 5 mL hydrochloric acid in 90 mL ethanol for 20–25 s. XRD data were collected from the copper deposits produced using a Siemens/Bruker General Area Detector Diffraction Solution, GADDS diffractometer and interpreted using the Scherrer equation (Fabian et al., 2003; Mathe et al., 2005).

Guar was dosed *twice* and APAM was dosed *once* during this testwork unless otherwise stated. The first dose was added at the beginning and the second at approximately half EW time depending on the current density. The total electrowinning time was 4 h 21 min at a current density of 320 A/m^2 and 4 h 58 min at 280 A/m^2. The number of Coulombs applied was 500 C/cm^2.

2.2. Experimental using parallel plate electrodes

The comparison between Guar and APAM was also carried out using parallel plate electrodes at current-industry standard copper electrowinning operating conditions — except for current density which was increased to 340 A/m^2 from the industry standard of 280–300 A/m^2. (Robinson et al., 2003). Simultaneously, Guar and APAM concentrations were also increased from about 175 g/tonne copper cathode or 0.25–0.50 mg/L in the electrolyte (as was dosed at Mt. Gordon) to 200 g/tonne or 0.68 mg/L.

A 316L 2B finish stainless steel cathode with a surface roughness of 0.25±0.05 μm and a lead–alloy anode procured from Mt. Gordon Operations were cut to prepare the electrodes for this testwork. Current industry-standard ABS edge strips were inserted on the stainless steel and the corners were joined at 45° with Araldite K138 and hardener K138 Part B — an acid resistant and thermally stable epoxy resin. The stainless steel substrates were thoroughly washed with acetone and water, soaked in an electrolyte solution for 24 h and washed again with distilled water. The distance between the electrodes was 40 mm, which is similar to the industry standard in copper EW. Fig. 2 shows the EW cell design in detail and Fig. 3 shows the overall bench scale design.

Table 3 shows the details of the operating conditions for the bench scale experiments. The net electrolyte volume in the EW cell was 3.9 L (without electrodes) and the flow rates of the re-circulating and advanced electrolyte were maintained constant at 31.5 and 7.9 mL/min, respectively. Eighty percent of the total electrolyte flow rate was re-circulated to the EW cell using a Watson Marlow 505S peristaltic pump to simulate the commercial operation at Mt. Gordon. This recirculation maintains the activity of Guar or APAM constant in the EW cell and also possibly

Table 3
Bench scale experimental conditions

Current density, A/m^2	340
Voltage drop, V	2.15
EW iime, h	44.6
Deposition area (85.5×103.5 mm), cm^2	88.5
Average copper concentration, g/L	35±1
Sulfuric acid concentration, g/L	160
Chloride ions concentration mg/L	25
Electrolyte net volume, L	3.9
Electrolyte temperature, °C	50.5±0.5
Guar or APAM, g/tonne copper cathode	200
Guar or APAM concentration in electrolyte, mg/L	0.68
Advanced electrolyte, mL/min	31.5
Recirculating electrolyte, mL/min	7.9
Syringe pump-dosing Guar or APAM, mL/h	2.1
Power to stir solution, (30 mA), Watts	7–8
Copper concentration in advanced electrolyte, g/L	50
Sulfuric concentration in advanced electrolyte, g/L	142
Chloride concentration in advanced electrolyte, mg/L	30

controls their ageing processes. The organic additives were dosed constantly at 2.1 mL/h using a syringe infusion pump. The concentration of the organic additive in the aliquot was 0.68 mg/mL. The electrolyte in the EW cell was stirred with minimum agitation using a magnetic stirrer to improve the diffusion of the organic additive. The electrolyte temperature was kept at 50.5±0.5 °C in a water bath.

3. Results and discussion

3.1. 2^{5-2} Experimental design results at 45 °C–55 °C

Table 4 presents the results indicating the effect of temperature (*A*), current density (*B*), Guar concentration (*C*), APAM concentration (*D*) and diffusion layer thickness (*E*) on surface roughness. The regression model obtained from this testwork is shown in Eq. (1). An *F*-value of 9.41 implies that the model is significant. There is only a 0.01% chance that the model *F*-value this large could occur due to noise. If the "Prob > *F*-value" (α) is very small (less than 0.05), then the terms in the model have a significant effect on the response (Montgomery, 2001; Stat-Ease, 2003).

$$\begin{aligned}\text{Surface Roughness}(\mu\text{m}) = {} & +6.26 + 0.05{*}A + 0.27{*}B \\ & -0.053{*}C - 0.056{*}D \\ & + 0.25{*}E - 0.62{*}B{*}C \\ & -0.38{*}B{*}E \end{aligned} \quad (1)$$

It can be seen that the surface roughness is strongly influenced by the current density *B*, (α=0.0180) and diffusion layer thickness *E*, (α=0.0247) as depicted in Fig. 4. Fig. 4 clearly indicates that at high rotational speed of the cylinder and low current density the smoothest surface roughness is achieved. In addition, it is also evident that the terms involving *B***C* (current density*Guar, α<0.0001), depicted in Fig. 5, significantly affect surface roughness. It can be seen that increasing the Guar concentration increases surface roughness at current densities lower than about 300 A/m^2, a surprising result for an organic additive dosed to control dendrite formation. Moreover, it indicates that the surface roughness increases more steeply with an increase in the current density than with an increase in Guar concentration.

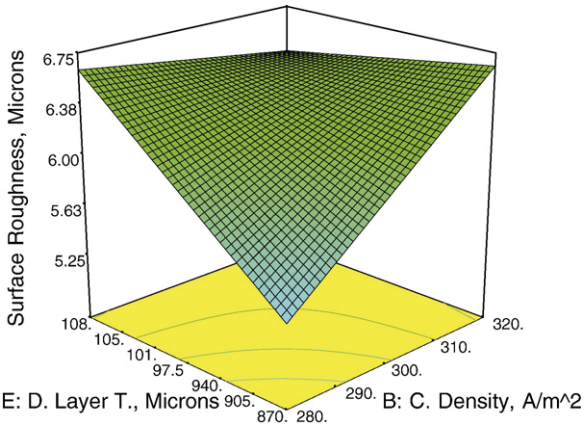


Fig. 4. The significant effect of diffusion layer thickness (*E*) and current density (*B*) on surface roughness in the temperature range of 45 °C–55 °C. The other variables are fixed at their centre point: *A*: temperature, 50 °C; Guar, 0.75 mg/L and *D*: APAM, 0.75 mg/L.

The effect of APAM was insignificant in this temperature range possibly due to the kinetics of its ageing in the electrolyte. The rationale for this conclusion is as follows. Cyclic voltammetry results

Table 4
2^{5-2} Fractional factorial experimental results–temperature levels 45 °C–55 °C

Run	*A* Temperature	B Current density	C Guar	D=*A***B*# APAM	*E*=*A***C*# Diffusion layer thickness	Mean surface roughness	S.D.
Standard	°C	mA/cm^2	mg/L	mg/L	μm	Ra, μm	
1	45	28	0.50	1.00	108	5.95	0.47
2	55	28	0.50	0.50	87	4.90	0.42
3	45	32	0.50	0.50	108	7.08	1.38
4	55	32	0.50	1.00	87	7.33	1.09
5	45	28	1.00	1.00	87	5.83	0.72
6	55	28	1.00	0.50	108	7.31	1.08
7	45	32	1.00	0.50	87	5.99	0.66
8	55	32	1.00	1.00	108	5.71	0.68
CP	50	30	0.75	0.75	97.50	7.04	0.93

#Level of factors *D* and *E* were determined by the levels of *A***B* and *A***C*, respectively.

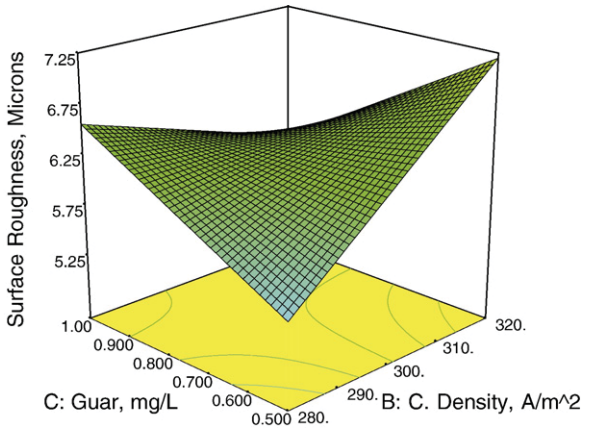


Fig. 5. The significant effect of current density (*B*) and Guar (*C*) on surface roughness in the temperature range of 45 °C–55 °C. The other variables are fixed at their centre point: *A*: temperature, 50 °C; *D*: APAM, 0.75 mg/L and *E*: diffusion layer thickness, 97.5 μm.

(Fabian, 2005) indicate that at 45 °C, a maximum polarization of APAM was obtained at about 3-hour residence time in the electrolyte whilst at 65 °C it was obtained at about 1-hour residence time. It is therefore inferred that the first 3 h of the EW tests at 45 °C–55 °C took place under sub-optimal adsorption/polarization conditions of APAM.

3.2. 2^{5-2} Experimental design results at 45 °C–65 °C

Table 5 presents the results indicating the effect of temperature (*A*), current density (*B*), Guar concentration (*C*), APAM concentration (*D*) and diffusion layer thickness (*E*) on surface roughness. The EW tests at this temperature range were also carried out for 4.35 and 4.97 h (14,000 C) as in the previous testwork. The model obtained from this testwork is shown in Eq. (2). An *F*-value of 2.06 implies that the model is significant and that there is a 6.3% chance that the model *F*-value this large could occur due to noise.

$$\text{Surface Roughness}(\mu\text{m}) = +6.16 - 0.051{*}A - 0.089{*}B - 0.075{*}C - 0.41{*}D + 0.23{*}E - 0.17{*}B{*}C \quad (2)$$

It can be seen from this model that APAM (*D*, $\alpha = 0.0041$) has the most significant effect on reducing surface roughness. Diffusion layer thickness (*E*, $\alpha = 0.1004$) has the next largest effect and an increase in *E* increases surface roughness as expected (Ilgar and O'Keefe, 1997). The aliased effect of current density (*B*) and Guar (*C*) are insignificant ($B{*}C$, $\alpha = 0.2185$). Current density *B* ($\alpha = 0.5192$), Guar *C*, ($\alpha = 0.5855$) and temperature *A*, ($\alpha = 0.7129$) are also insignificant. The regression analysis (Montgomery, 2001) indicates again that APAM and Guar are also not aliased and therefore confirms that APAM acts independently of Guar to reduce surface roughness. Therefore the effect of Guar and APAM on surface roughness was investigated separately, as described in the following Sections.

3.3. Effect of Guar or APAM over 6-hour EW at 50 °C

This test was conducted to continue evaluating the effectiveness of Guar or APAM, either alone or in combination, on surface roughness and on the number of Peaks-per Centimetre (PPC) over 6 h of EW. PPC is defined as the number of roughness profile elements per centimetre which consecutively intersect at a specified upper profile section level and a lower profile section (Mahr, 2002). A surface profile can have the

Table 5
2^{5-2} Fractional factorial experimental results–temperature levels 45 °C–65 °C

Run	*A*	B	C	D=*A***B*	*E*=*A***C*	Mean surface roughness	S.D.
	Temperature	Current density	Guar	PAM	Diffusion layer thickness		
Standard	°C	mA/cm^2	mg/L	mg/L	μm	Ra, μm	
1	45	28	0.50	1.00	110	5.95	0.47
2	65	28	0.50	0.50	87	6.36	0.64
3	45	32	0.50	0.50	110	7.08	1.38
4	65	32	0.50	1.00	87	5.56	0.67
5	45	28	1.00	1.00	87	5.83	0.72
6	65	28	1.00	0.50	110	6.86	2.28
7	45	32	1.00	0.50	87	5.99	0.66
8	65	32	1.00	1.00	110	5.66	0.69

Table 6
6-hour EW time at 50 °C: Guar-or-APAM

	Factors, mg/L		Surface roughness, μm		No. PPC		Dendrites
Run	*B* = APAM	*A* = Guar	Mean	S.D.	Mean	S.D.	Small needles
1	0	0	7.68	2.16	65.13	13.95	Numerous
2	0	1	6.48	0.70	87.63	8.35	Numerous nascents
3	1	0	6.42	0.27	82.75	8.24	None
4	1	1	6.71	0.36	83.38	7.46	None

same surface roughness with a different number of PPC. Guar was dosed twice and APAM once. The electrolyte temperature, current density and δ were 50 °C, 300 A/m^2 and 109 μm (10 rpm), respectively. The experimental design and results are shown in Table 6. Eq. (3) shows the surface roughness model for this testwork where A is Guar concentration and B is APAM concentration.

$$\text{Surface Roughness}(\mu\text{m}) = 6.45 + 0.144^{*}A - 0.627^{*}B \quad (3)$$

The Model F-value of 2.58 for surface roughness implies the model shown in Eq. (3) is significant with a 9.37% chance that a "Model F-Value" this large could occur due to noise. APAM (B, $\alpha = 0.0388$) has a significant effect on reducing surface roughness and Guar (A, $\alpha = 0.623$) has an insignificant effect on increasing surface roughness as shown in Fig. 6.

The number of PPC reported in Table 6 was also analysed to confirm the surface roughness results described above. The model for the PPC is presented in Eq. (4) and depicted in Fig. 7. The Model F-value of 8.85 for the number of PPC implies the model is significant with only a 0.11% chance that a "Model F-Value" this large could occur due to noise.

$$\text{Number of Peaks} - \text{per} - \text{Centimetre} = 85.2 + 0.313^{*}A + 8.81^{*}B \quad (4)$$

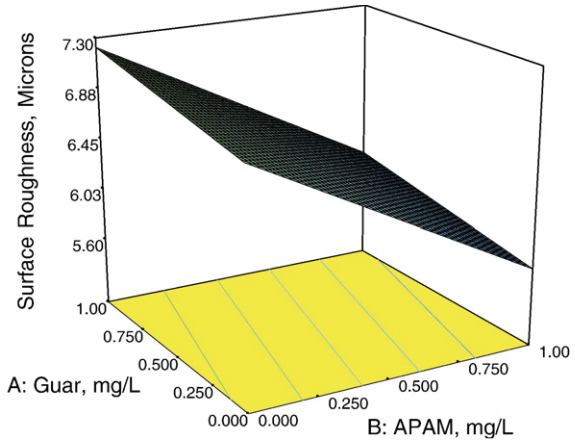


Fig. 6. The significant effect of APAM on surface roughness after 6-hour EW.

It is concluded from these results that APAM significantly reduced surface roughness and increased the number of PPC. In contrast, Guar increased the surface roughness and decreased the number of PPC similar to the copper deposit produced without additives. Table 6 shows results and visual observations from the testwork. It can be seen that qualitatively, the formation of dendrites is reduced in the presence of APAM.

3.4. Effect of Guar or APAM in continuous bench scale tests

Bench scale testwork was aimed at verifying the effectiveness of Guar and APAM in controlling dendrite growth in a continuous copper EW system using *parallel plate* electrodes. The surface roughness of the copper deposits was unable to be measured since it surpassed the specifications of the M1 Perthometer (10 nm–100 μm). Photographs of the electrowon copper deposits in the presence of Guar and APAM are shown in Figs. 8 and 9, respectively. It can be seen that the physical appearance of copper deposit obtained with Guar was rougher than that obtained with APAM. Both sides of the deposit produced with Guar have a needle-like, granular appearance throughout the plate. In contrast, the deposit produced with APAM is smoother, brighter and more compact than the copper deposit produced with Guar. Moreover, the copper deposits obtained with Guar possess three areas where copper deposition has not taken place. This is described as "lacy" copper

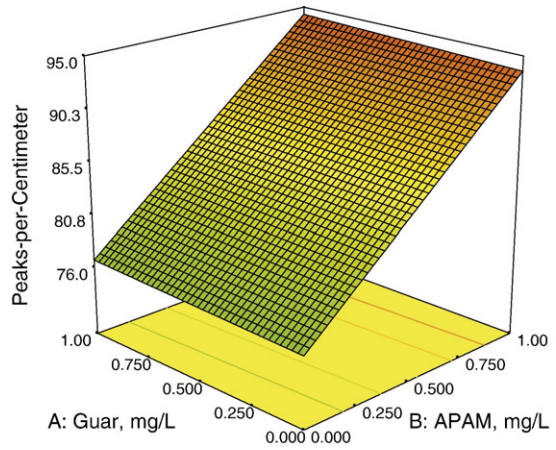


Fig. 7. The significant effect of APAM on Peaks-per-Centimetre after 6-hour EW.

deposit and was also reported by Sun and O'Keefe (1992) in the absence of additives. This kind of deposit is often found at commercial scale electrowinning operations but not at ER operations where animal glue and thiourea are used as organic additives. The brightening effect of the copper deposit in the presence of APAM was probably achieved through large crystal faces that are parallel to the substrate.

Figs. 10 and 11 are SEM micrographs of the cross-sectioned copper cathodes obtained from this testwork. It can be seen in Fig. 10 that the cross section of the copper cathode obtained with APAM exhibits columnar growth. It has been reported that this type of growth may be improved into an equiaxial microstructure by adding a sulfur bearing organic additive into the electrolyte bath (Plieth, 1992). In contrast, in the presence of Guar, the microstructure of the copper deposit is *porous* (Fig. 11).



Fig. 8. Copper deposit obtained with Guar at 340 A/m^2 and 44 h and 35 min.



Fig. 9. Copper deposit obtained with APAM at 340 A/m^2 and 44 h and 35 min.

Crystallite size was also determined using an XRD technique, General Area Diffraction Detector Solution (GADDS), according to the technique described elsewhere (Fabian et al., 2003). The crystallite size was determined to assess whether the presence of APAM or Guar results in higher nucleation rates during EW under otherwise constant conditions. These tests may also be important to determine coalescence of small crystallite sizes to form larger crystal sizes according to the mechanism of 3D crystallite size growth.

Table 7 shows the Kruskal–Wallis test results for APAM and Guar crystallite size obtained from the bench scale testwork using parallel plate electrode. The median crystallite size with APAM (405 Å) is slightly smaller than with Guar (427 Å). Therefore APAM appears to favour a higher nucleation rate than Guar. The other important results are the 41% crystallite size greater than 1800 Å: for APAM and 24% for Guar. The inferred crystallite size decreases as the full width at half-maximum (FWHM) of the copper deposit sample increases (Klug and Alexander, 1974). If the FWHM of

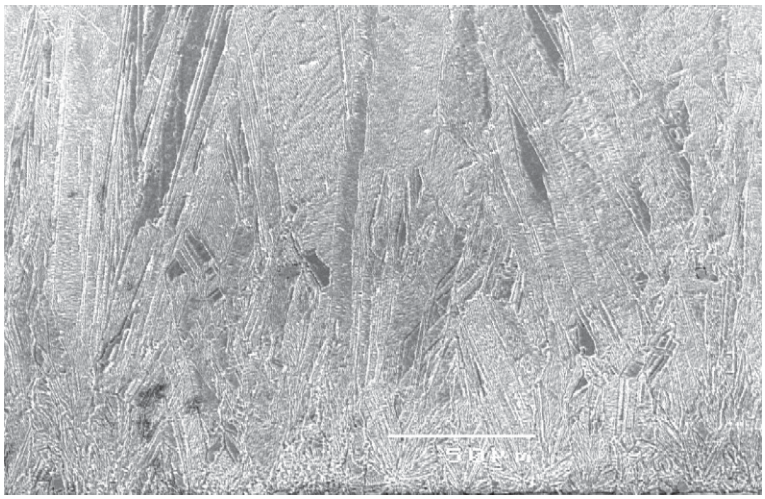


Fig. 10. SEM micrographs of copper deposit obtained using 0.68 mg/L APAM (200 g/tonne Copper Cathode) at 340 A/m^2 current density. Note the slightly fibrous or columnar structure.

the sample is smaller than that of the LaB_6 standard, the crystallite size is not processed and is reported as greater than 1800 Å. These calculations therefore appear to indicate that nucleation rates, 3D crystallite growth, and coalescence is higher with APAM than with Guar.

Bench-scale continuous electrowinning tests using parallel plate electrodes where APAM and Guar were dosed continuously and independently also indicated that APAM produces smoother deposits than Guar. The overall results suggest that APAM is more specifically adsorbed than Guar at the metal electrode/electrolyte interface where high electrical fields are convergent. This behaviour can therefore inhibit the formation of protrusions/dendrites. The covalent bonding that polyacrylamide block polymer confers at the metal/electrolyte interface (Halverson et al., 1985; Panzer and Halverson, 1988; Panzer et al., 1984) probably plays an important role for APAM to be more specifically adsorbed than Guar.

The adsorption properties for Guar were not found in the literature. The difference on inhibition (polarization) and adsorption produced by Guar and APAM has been studied by us using Cyclic Voltammetry and

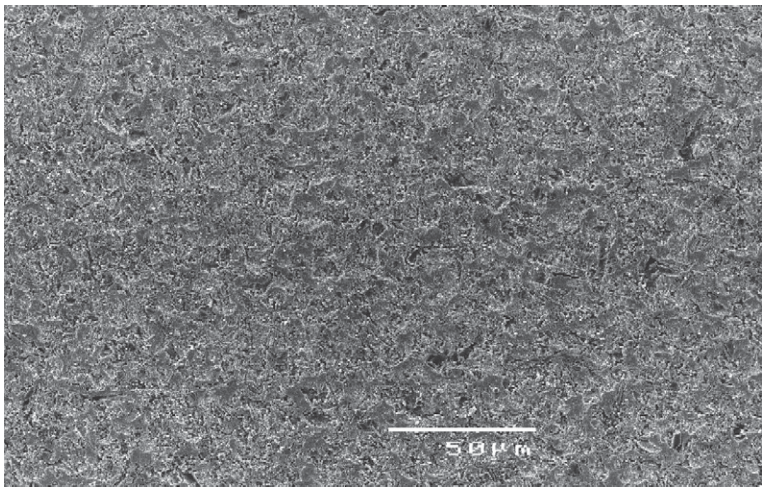


Fig. 11. SEM micrographs of copper deposit obtained using 0.68 mg/L Guar (200 g/tonne Copper Cathode) at 340 A/m^2 current density. Note a porous copper cathode.

Table 7
Kruskal–Wallis test results for APAM and Guar crystallite size

Test no.	APAM	Guar
Electrowinning Time, h	44.60	44.60
FWHM number of readings, N	338	440
Crystallite size data processed, N	198	335
Crystallites size >1800 Å, %	41	24
Kruskal–Wallis crystallite size mean rank	220	295
Asymptotic significance	0.000	
Median crystallite size, Å	405	427

Electrochemical Impedance Spectroscopy (Fabian, 2005) and will be discussed in subsequent papers.

4. Conclusions

It was found that when 14,000 C were applied in the fractional factorial experimental design that the effect of APAM was significant in reducing surface roughness at 65 °C but insignificant at 45 °C. This difference is attributed to stronger adsorption and enhanced polarization of APAM at 65 °C. The regression models from this experimental design indicated that APAM and Guar are not aliased and that APAM acts truly independently of Guar. It was also found that current density and Guar were aliased but decreases in significance with increasing temperature consistent with the faster degradation of Guar. Therefore, the role of Guar and APAM was concluded to be independent. In the 6-hour EW tests, APAM significantly reduced surface roughness and increased the number of Peaks-per-Centimetre.

Bench-scale continuous electrowinning tests where APAM and Guar were dosed continuously and independently indicated that APAM produces smoother deposits than Guar. SEM examination of cross sections of the copper deposits showed that Guar produced porous deposits and APAM produced slightly columnar deposits. Furthermore, the copper deposit with APAM is brighter and has greater amounts of both smaller and larger crystallite sizes than those with Guar. We infer that presence of APAM favours higher nucleation rates and greater 3D crystallite growth and coalescence than Guar and that APAM can produce purer copper deposits since voids and porosity can be reduced by smaller crystallites.

The overall results of this work indicate that APAM produces smoother, brighter and more compact copper electrodeposits than Guar. Therefore APAM can be viewed as a potential new levelling and brightening agent for copper electrometallurgy.

Acknowledgments

We wish to thank Mount Gordon Operations of Western Metals Copper Ltd. and to the Australian Research Council for funding this study.

References

Arvia, A.J., Carrozza, J.S.W., 1962. Mass transfer in the electrolysis of $CuSO_4$–H_2SO_4 in aqueous solutions under limiting current and forced convection employing a cylindrical cell with rotating electrodes. Electrochimica Acta 7, 65–78.

Barkey, D., Muller, R., Tobias, C., 1989. Roughness development in metal electrodeposition I. Experimental results. Journal of the Electrochemical Society 138 (8), 2199–2207.

Budevski, E., Staikov, G., Lorenz, W., 1996. Electrochemical Phase Formation and Growth — an Introduction to the Initial Stages of Metal Deposition. VCH, New York.

Fabian, C., 2005. Copper electrodeposition in the presence of guar or activated polyacrylamide. PhD Thesis, James Cook University, Australia.

Fabian, C., Ridd, M., Ness, S., Lancaster, T., Griffin, G., 2003. Determination of crystallite size and surface roughness of copper deposits for electrowinning in the presence of an organic additive. In: Young, C.A., Anderson, C.G., Dreisinger, D.B., Harris, B., James, A. (Eds.), Hydrometallurgy. The Minerals Metals and Materials Society (TMS), Warrendale, pp. 1233–1245.

Fabian, C., Mandin, P., Ridd, M.J., Sheehan, M., 2006a. Hydrodynamic modelling of copper electrodeposition at a vertical rotating cylinder electrode. In: Woods, R., Doyle, F.M., Kelsall, G.H. (Eds.), Electrochemistry in Mineral and Metal Processing VII. The Electrochemical Society Inc., Denver, CO, pp. 303–315.

Fabian, C., Ridd, M.J., Sheehan, M.E., 2006b. Rotating cylinder electrode study of the effect of activated polyacrylamide on surface roughness of electrodeposited copper. Hydrometallurgy 84 (3–4), 256–263.

Halverson, F., Lancaster, J., O'Connor, M., 1985. Sequence distribution of carboxyl groups in hydrolyzed polyacrylamide. Macromolecules 18 (6), 1139–1144.

Ilgar, E., O'Keefe, T., 1997. Surface roughening of electrowon copper in the presence of chloride ions. In: Dreisinger, D. (Ed.), Aqueous Electrotechnologies: Progress in Theory and Practice. The Minerals Metals and Materials Society (TMS), Warrendale, pp. 51–62.

Klug, H., Alexander, L., 1974. X-ray Diffraction Procedures for Polycrystalline and Amorphous Materials. John Wiley & Sons, Sydney.

Langner, B.E., Stantke, P., Reinking, E.F., 1989. Method of Measuring the Effective Inhibitor Concentration During a Deposition Process of Metal from Aqueous Electrolytes and Test Apparatus Therefore. Norddeutsche Affinerie Aktiengesellschaft, Hamburg, DE, p. 11.

Mahr, 2002. M1 Mahr Perthometer Operating Manual.

Mark, H., Gaylord, N., Bikales, N., 1969. Encyclopedia of Polymer Science and Technology, vol. 11. Wiley-Interscience, New York, pp. 401–420.

Mathe, M.K., Cox, S.M., Venkatasamy, V., Happek, U., Stickney, J.L., 2005. Formation of HgSe thin films using electrochemical atomic layer epitaxy. Journal of the Electrochemical Society 152 (11), C751–C755.

MathSoft Engineering and Education, I, 2004. Mathcad.

Montgomery, D.C., 2001. Design and Analysis of Experiments. John Wiley & Sons.

Newman, J., Thomas-Alyea, K.E., 2004. Electrochemical Systems. John Wiley & Sons, Inc., Hoboken, New Jersey.

Panzer, H., Halverson, F., 1988. Blockiness in hydrolyzed polyacrylamide. In: Moudgil, B., Scheiner, B. (Eds.), Flocculation Dewatering, Proc. Eng. Found. Conf., Florida. Eng. Found., New York, N.Y, pp. 239–249.

Panzer, H., Halverson, F., Lancaster, J., 1984. Carboxyl sequence distribution in hydrolyzed polyacrylamide. Polymeric Materials Science and Engineering 51, 268–271.

Plieth, W., 1992. Additives in the electrocrystallization process. Electrochimica Acta 37 (12), 2115–2121.

Pye, D., Schurz, G., 1957. Electrowinning of metals, U.S.Patent 2,798,040. The Dow Chemical Company.

Robinson, T., Davenport, W.G., Quinn, J., Karkas, G., 2003. Electrolytic copper refining — 2003 world tankhouse operating data. In: Dutrizac, J.E., Clement, C.G. (Eds.), Proc. Copper 2003–Cobre 2003, Santiago, Chile. Canadian Institute of Mining, Metallurgy and Petroleum, Montreal, pp. 3–66.

Stantke, P., 1999. Guar concentration measurement with the Collamat system. In: Dutrizac, J., Ji, J., Ramachandran, V. (Eds.), Proc. Copper 99–Cobre 99, vol. 3. Minerals, Metals and Materials Society, Warrendale, PA, pp. 643–651.

Stat-Ease, S.M.E., 2003. Design-Expert Software. John Wiley & Sons, Inc.

Sun, M., O'Keefe, T., 1992. The effect of additives on the nucleation and growth onto stainless steel cathodes. Metallurgical Transactions. B, Process Metallurgy 23B, 591–599.

Vereecken, J., Winand, R., 1976. Influence of polyacrylamides on the quality of copper deposits from acidic copper sulphate solutions. Surface Technology 4, 227–235.

Vereecken, P.M, Binstead, R.A, Deligianni, H., Andricacos, P.C., 2005. The chemistry of additives in damascene copper plating. IBM Journal of Research and Development 49 (1), 3–19.

APPENDIX GRIESI01

University Libraries
UNIVERSITY OF SOUTH CAROLINA

Scholar Commons

Home | About | FAQ | My Account

Search
Enter search terms:
Search
in this series
Advanced Search
Notify me via email or RSS

Browse
Collections
Disciplines
Authors

Submissions
Author FAQ

Links
Give us Feedback
University Libraries
Exhibits

THESES AND DISSERTATIONS

Characterization of Electrodeposited Copper Foil Surface Roughness for Accurate Conductor Power Loss Modeling

Michael B. Griesi, *University of South Carolina - Columbia*

Follow

Download

2,837 DOWNLOADS
Since January 21, 2015

PLUMX METRICS

INCLUDED IN
Electrical and Computer Engineering Commons

SHARE

Date of Award
12-15-2014

Document Type
Open Access Thesis

Department
Electrical Engineering

First Advisor
Paul G. Huray

Abstract
As computer data rates have increased, designers observed that the standard models for estimating the impact of copper foil surface roughness on conductor loss are limited to a few GHz. The more recent snowball model (a "snowball" estimation of the Huray Model) has demonstrated improved conductor loss predictions up to 50 GHz by estimating the necessary parameters using reasonable assumptions about the geometric surface features of electrodeposited copper foil. Since then, the Huray Model has been incorporated into commercial electromagnetic field simulators. However, a standard method of characterizing the electrodeposited copper foil used in high-speed circuits to directly implement the snowball model has not yet been fully established. Therefore, the primary objective of this thesis was to develop a method of more accurately characterizing the geometric parameters of electrodeposited copper foil surfaces for accurate conductor loss modeling as defined by the snowball model. This thesis demonstrates the first methods of directly characterizing electrodeposited copper foil surface roughness to obtain snowball model parameters. Additionally, this research further legitimizes the analytic form of the snowball model as it pertains to scattered power, demonstrates the practical impact of its parameters, and reveals a source of existing irregularities between the estimated model parameters and actual performance measurements.

Rights
© 2014, Michael B. Griesi

Recommended Citation
Griesi, M. B.(2014). *Characterization of Electrodeposited Copper Foil Surface Roughness for Accurate Conductor Power Loss Modeling.* (Master's thesis). Retrieved from https://scholarcommons.sc.edu/etd/2958

DIGITALCOMMONS powered by bepress

Home | About | FAQ | My Account | Accessibility Statement
Privacy Copyright

University of South Carolina
Scholar Commons

Theses and Dissertations

12-15-2014

Characterization of Electrodeposited Copper Foil Surface Roughness for Accurate Conductor Power Loss Modeling

Michael B. Griesi
University of South Carolina - Columbia

Follow this and additional works at: https://scholarcommons.sc.edu/etd

 Part of the Electrical and Computer Engineering Commons

Recommended Citation

Griesi, M. B.(2014). *Characterization of Electrodeposited Copper Foil Surface Roughness for Accurate Conductor Power Loss Modeling.* (Master's thesis). Retrieved from https://scholarcommons.sc.edu/etd/2958

This Open Access Thesis is brought to you by Scholar Commons. It has been accepted for inclusion in Theses and Dissertations by an authorized administrator of Scholar Commons. For more information, please contact digres@mailbox.sc.edu.

CHARACTERIZATION OF ELECTRODEPOSITED COPPER FOIL SURFACE ROUGHNESS FOR ACCURATE CONDUCTOR POWER LOSS MODELING

by

Michael B. Griesi

Bachelor of Science
University of South Carolina, 2013

Submitted in Partial Fulfillment of the Requirements

For the Degree of Master of Science in

Electrical Engineering

College of Engineering and Computing

University of South Carolina

2014

Accepted by:

Paul G. Huray, Director of Thesis

Olufemi B. Oluwafemi, Reader

Lacy Ford, Vice Provost and Dean of Graduate Studies

© Copyright by Michael Griesi, 2014
All Rights Reserved.

DEDICATION

I dedicate this thesis to my wife Jessica. It was her love, support, understanding and patience that made this pursuit possible. I will be forever grateful.

ACKNOWLEDGEMENTS

My deepest gratitude goes to my professor, advisor and committee chair Dr. Paul Huray. His passion for understanding the curious and nuanced intricacies of electromagnetic phenomenon is both inspiring and enlightening. It was through this passion I found a trusted mentor, leader and friend in our shared pursuit of understanding. Of particular importance to the completion of this thesis were Dr. Huray's integral research and development of the Huray surface roughness model accompanied by his detailed instruction provided throughout his lectures and publications.

A special thanks to my committee member Dr. Olufemi (Femi) Oluwafemi whose contributions to developing the snowball model provided practical relevance and legitimacy to the conclusions and impact of this thesis. Furthermore, his feedback was both motivating and constructive.

I especially want to thank John Fatcheric and Lee Lesher of Oak-Mitsui who contributed a significant amount of time explaining the process of manufacturing electrodeposited copper foil and providing a plant tour. Furthermore, they supplied most of the material and measurement tools for this research. The conclusions of this thesis are thanks to John and Lee's willingness to share their knowledge and resources.

I also want to thank Stephen Hall, who generously contributed constructive feedback for focused and practical content. As well, I would like to thank Christine Jones for graciously sharing additional VNA measurements and test board specifications that were critical for these conclusions. Thank you all.

ABSTRACT

As computer data rates have increased, designers observed that the standard models for estimating the impact of copper foil surface roughness on conductor loss are limited to a few GHz. The more recent snowball model (a "snowball" estimation of the Huray Model) has demonstrated improved conductor loss predictions up to 50 GHz by estimating the necessary parameters using reasonable assumptions about the geometric surface features of electrodeposited copper foil. Since then, the Huray Model has been incorporated into commercial electromagnetic field simulators. However, a standard method of characterizing the electrodeposited copper foil used in high-speed circuits to directly implement the snowball model has not yet been fully established. Therefore, the primary objective of this thesis was to develop a method of more accurately characterizing the geometric parameters of electrodeposited copper foil surfaces for accurate conductor loss modeling as defined by the snowball model.

This thesis demonstrates the first methods of directly characterizing electrodeposited copper foil surface roughness to obtain snowball model parameters. Additionally, this research further legitimizes the analytic form of the snowball model as it pertains to scattered power, demonstrates the practical impact of its parameters, and reveals a source of existing irregularities between the estimated model parameters and actual performance measurements.

PREFACE

This work is divided into six chapters. Chapter one introduces the motivation and reasons for this research. Chapter two reviews the history of conductor loss modeling, introduces electrodeposited copper foil and recent developments in conductor loss modeling. Chapter three meets the primary objective of this research by demonstrating methods for characterizing the surface of electrodeposited copper foil for accurate conductor loss modeling with results. Chapter four demonstrates a method for implementing the characterized parameters in commercially available simulation tools. Chapter five considers some limitations and concerns for the characterization methods described and alternatives measurements. Chapter six concludes with significant takeaways and recommendations for future work.

TABLE OF CONTENTS

DEDICATION iii

ACKNOWLEDGEMENTS iv

ABSTRACT v

PREFACE vi

LIST OF TABLES ix

LIST OF FIGURES x

LIST OF SYMBOLS xiii

LIST OF ABBREVIATIONS xv

CHAPTER 1: INTRODUCTION 1

CHAPTER 2: BACKGROUND 3

2.1 ELECTRICAL CONDUCTOR LOSSES IN HIGH-SPEED TRANSMISSION LINES 3

2.2 THE MORGAN-HAMMERSTAD EMPIRICAL FIT 4

2.3 PROBLEMS WITH THE MORGAN-HAMMERSTAD EMPIRICAL FIT 6

2.4 ELECTRODEPOSITED COPPER FOIL 11

2.5 THE SNOWBALL MODEL 15

2.6 OBJECTIONS TO AND PROBLEMS WITH THE SNOWBALL MODEL 17

CHAPTER 3: COPPER FOIL SURFACE CHARACTERIZATION 24

3.1 IMPACT OF SNOWBALL MODEL PARAMETERS ON CONDUCTOR LOSS 24

3.2 CHARACTERIZING TREATED COPPER FOIL: a_i AND N_i/A_{flat} 27

3.3 CHARACTERIZING UNTREATED COPPER FOIL: A_{matte}/A_{flat} 34

Chapter 4: Using Characterized Parameters in Simulation Tools 42
4.1 An Effective Snowball Radius 43
4.2 Performance Experiments 45
Chapter 5: Discussion 52
5.1 Concerns and Alternatives 52
5.2 Known Limitations of this Research 53
Chapter 6: Conclusion and Future Work 56
6.1 Conclusion 56
6.2 Future Work 57
References 58
Appendix A – Periodic Interpolation Pseudocode 60
Appendix B – MATLAB Code for Oak-Mitsui Image Analysis 61
Appendix C – MATLAB Code for Gould Image Analysis 64
Appendix D – MATLAB Code for 3D Microscope Distribution Binning 67
Appendix E – MATLAB Code for Average Distribution Binning 69
Appendix F – Python Code for Composite Simpson's Rule 71
Appendix G – Derivation of Eddy Current Equation 73

LIST OF TABLES

Table 2.1 Conductor Surface Parameters of the Snowball Model.....16

Table 3.1 Drum Side A_{matte}/A_{flat} 39

Table 3.2 Matte Side A_{matte}/A_{flat} 39

Table 4.1 Microstrip Model Dimensions.....46

LIST OF FIGURES

Figure 2.1 (a) Rectangular and (b) triangular surface grooves. 5

Figure 2.2 Current density isolated within the RMS surface roughness.....6

Figure 2.3 Hammerstad Fit vs. VNA measurement of 7" microstrip. 7

Figure 2.4 Incorrect current path for a rough surface with skin depth. 8

Figure 2.5 Cross sectional view of isolated copper below a microstrip. 9

Figure 2.6 (a) Traditional vs (b) fundamental current density in high-speed conductors..10

Figure 2.7 Three phases of ED copper foil fabrication.....11

Figure 2.8 Oak-Mitsui Untreated Drum Side 0.5 oz MLS GIII HTE foil 3500x. 12

Figure 2.9 Oak-Mitsui Untreated Matte Side 0.5 oz TOB GIII HTE 3500x. 13

Figure 2.10 Oak-Mitsui Treated Drum Side 0.5 oz MLS GIII HTE foil 3500x. 14

Figure 2.11 Oak-Mitsui Treated Matte Side 0.5 oz TOB GIII HTE 3500x. 14

Figure 2.12 Gould Treated Drum Side 5000x. 15

Figure 2.13 Snowball model vs. VNA measurement of 7" microstrip. 17

Figure 2.14 Absorption and scattering cross-sections of various size copper spheres. 20

Figure 2.15 Distribution of snowball sizes emphasized with orange rings. 21

Figure 2.16 Altered number of snowballs in stack-up caused by an irregular base. 22

Figure 2.17 Snowball densities on drum side (left) vs. matte side (right). 22

Figure 3.1 Distribution effect on skin loss. 25

Figure 3.2 Distribution effect on power loss for a 5" microstrip. 25

Figure 3.3 Effect of a uniform snowball radius vs. a narrow distribution of radii. 26

Figure 3.4 Effect of a uniform snowball radius vs. a wide distribution of radii. 26

Figure 3.5 SEII v2.3 PCI Scanning Electron Microscope (SEM). 28

Figure 3.6 MATLAB Snowballs on Drum (left) and Matte (right) Sides. 29

Figure 3.7 Snowball Radii Distribution of Drum Side from SEM Method. 30

Figure 3.8 Hirox KH-8700 E 3D Digital Microscope. 31

Figure 3.9 Microscope Snowballs on Drum (left) and Matte (right) Sides. 32

Figure 3.10 Snowball Radii Distribution of Drum Side from Microscope Method. 33

Figure 3.11 Linear Interpolation between Data Points (Absolute Minimum). 35

Figure 3.12 Sin Interpolation between Data Points (Effective Maximum). 36

Figure 3.13 Hybrid Interpolation between Data Points (Intermediate). 37

Figure 3.14 Periodic Interpolation of Data Points (Intermediate). 37

Figure 3.15 Mahr M2 Perthometer Controller (left) and Pull Force Meter (right). 38

Figure 3.16 Printed Perthometer Surface Profile of Raw Untreated Copper Foil. 38

Figure 3.17 Recreation of Surface Profile from Discrete Data Points. 38

Figure 3.18 3D Drum Side (left) and Matte Side (right) Untreated Copper Surfaces. 40

Figure 4.1 Gould Snowball Radii Distribution of Drum Side from SEM Method. 43

Figure 4.2 Determination of an Effective Snowball Radius. 44

Figure 4.3 Actual Microstrip (top) and Modeled Microstrip (bottom). 46

Figure 4.4 5” Huray Model with a flat non-causal substrate vs. VNA Measured. 47

Figure 4.5 5” Groisse Model with a flat non-causal substrate vs. VNA Measured. 47

Figure 4.6 7” Huray Model with a flat non-causal substrate vs. VNA Measured. 48

Figure 4.7 7” Groisse Model with a flat non-causal substrate vs. VNA Measured. 48

Figure 4.8 5” Huray Model with a Djordjevic-Sarkar substrate vs. VNA Measured. 49

Figure 4.9 5” Groisse Model with a Djordjevic-Sarkar substrate vs. VNA Measured.....49

Figure 4.10 7” Huray Model with a Djordjevic-Sarkar substrate vs. VNA Measured.....50

Figure 4.11 7” Groisse Model with a Djordjevic-Sarkar substrate vs. VNA Measured....50

Figure 5.1 Hidden snowballs (blue) beneath surface snowballs on low profile ED foil. ..52

Figure 5.2 Hypothetical distribution (orange) scaled by hidden snowballs (blue). 53

Figure 5.3 Hidden snowballs (blue) beneath surface snowballs on high profile ED foil. .53

Figure 5.4 Elemental compositions of snowballs after a treatment of brass. 54

LIST OF SYMBOLS

A	Area (Square Meters)
A_{flat}	Perfectly Flat Surface Area of Copper Foil (Square Meters)
a_i	Radius of the i^{th} Snowball (Meters)
A_{matte}	Actual Untreated Surface Area of Copper Foil (Square Meters)
$\vec{B}$	Magnetic Flux Density (Tesla)
δ	Skin Depth (Meters)
Δ	RMS Peak-to-Valley Surface Deviation (Meters)
$\vec{E}$	Electric Field Intensity (Volts per Meter)
ε_0	Permittivity of Free Space (Farads per Meter)
$\varepsilon_{r,2}$	Permittivity of Propagating Medium (Dimensionless)
η	Intrinsic Impedance of the Propagating Medium (Ohms)
f	Frequency (Hertz)
$\vec{H}$	Magnetic Field Intensity (Amperes per Meter)
$\vec{H}_0$	Maximum Amplitude of Magnetic Field Intensity (Amperes per Meter)
I	Electric Current (Amperes)
$\vec{J}$	Electric Current Density (Amperes per Square Meter)
k_2	Wave Number in the Propagating Medium (Meters)
l	Length (Meters)
μ	Permeability (Henry per Meter)

μ_0	Permeability of Free Space (Henry per Meter)
N_i	Total Number of Snowball of radial size a_i (Dimensionless)
P_{loss}	Electrical Power Loss (Watts)
P_{rough}	Electrical Power Loss of a Rough Conductor (Watts)
P_{smooth}	Electrical Power Loss a Smooth Conductor (Watts)
$R_{conductor}$	Electrical Resistance (Ohms)
ρ	Resistivity (Ohm Meters)
σ	Conductivity (Siemens per Meter)
$\sigma_{absorbed}$	Absorption Cross Section of Radial Size a_i (Square Meters)
$\sigma_{scattered}$	Scattered Cross Section of Radial Size a_i (Square Meters)
σ_{total}	Total Absorption and Scattered Cross Section (Square Meters)
SR	Hall-Huray Surface Ratio (Dimensionless)
ω	Angular Frequency (Radians per Second)

List of Abbreviations

CHT.....Circular Hough Transform

DC..... Direct Current

DSP.....Digital Signal Processing

ED.....Electrodeposited

FR-4.....Flame Retardant 4

GHz.....Gigahertz

GI..... Grade I

GIII.....Grade III

HFSS..... High Frequency Structural Simulator

HTE.....High Temperature Elongation

kHz..... Kilohertz

MHT.....Mitsui High Temperature

MLS..... Multi-Layer Shiny Side Treatment

PCB..... Printed Circuit Board

PLSP..... Plain Stain Proof

PTFE.....Polytetrafluoroethylene

RGB.....Red Green Blue

RMS.....Root Mean Square

SEM..... Scanning Electron Microscope

TOB.....Treatment of Brass

VNA..... Vector Network Analyzer

CHAPTER 1

INTRODUCTION

With computer bus speeds increasing from only 108 kHz in 1971 to nearly 4 GHz in 2010 and even higher frequencies currently under development, the success of high-speed circuit designs depends more than ever on precisely predicting signal power loss [1] [2]. Interestingly, however, most of today's high speed bus designs rely on low-frequency circuit concepts with hypothetical parameters, rather than applying a first principle analysis to the propagation of high-frequency electromagnetic fields using properly characterized materials. In particular is the power loss prediction associated with copper foil conductors used in modern printed circuit boards (PCBs). While a low frequency analysis of conductor loss is rather simple, a high frequency analysis becomes especially challenging when considering the effects of a conductor's surface roughness geometry on electromagnetic fields.

The conventional method of estimating the impact of conductor surface roughness on electrical power loss is the Morgan-Hammerstad empirical fit. The conclusions of this empirical fit were based on a hypothetical surface roughness with illogical assumptions that contradicted causality and, in some instances, principles of relativity that has consequently proven incapable of suitably estimating conductor power losses above a few GHz. While there are a few modified forms of the Morgan-Hammerstad empirical fit which attempt to correct its inherent frequency limitation, they are all plagued by the same logic flaw that limits accurate conductor loss modeling to a relatively narrow band.

Recently, as industry struggled to increase bus speeds to 8 Gbps (4 GHz), the Huray surface roughness model was developed using a first principles analysis of high-frequency propagating electromagnetic fields in copper-based channels to enable logical and accurate conductor loss predictions for all frequencies. This provided a much needed fundamental description of conductor loss as determined directly from Maxwell's field equations. In order to provide industry with a simple and practical method of implementing the Huray surface roughness model, the snowball model was derived directly from the more general Huray surface roughness model to correspond with scanning electron microscope (SEM) images taken of electrodeposited copper foil used in modern high-speed transmission lines.

CHAPTER 2

BACKGROUND

2.1 ELECTRICAL CONDUCTOR LOSSES IN HIGH-SPEED TRANSMISSION LINES

At low frequencies, conductor losses are easily explained by Joule's first law:

$$P_{loss} = I^2 R_{conductor} \tag{1}$$

where P_{loss} is the power lost to heat in W and I is the current flowing through the conductor in amperes. $R_{conductor}$ is the resistance of the conductor in Ω defined as

$$R_{conductor} = \frac{\rho l}{A} \tag{2}$$

where ρ is the resistivity in Ωm, l is the length in m and A is the cross sectional area in m^2. The simplicity of this analysis is thanks to a relatively uniform current density distributed throughout the entire thickness of a conductor at low, at or near DC, frequencies. However, as the frequency of the signal transmitted through the conductor increases, the exponentially decaying penetration depth, $e^{-x/\delta}$, of the current density reduces until it resides largely on the surface of the conductor effectively reducing the cross sectional area of the conductor and increasing the resistance as described by (2). This is well known as the skin effect and can be determined by

$$\delta(f) = \sqrt{\frac{2}{\omega\mu\sigma}} = \sqrt{\frac{1}{\pi f\mu\sigma}} \tag{3}$$

where δ is the exponential penetration depth of the current density in meters, ω is the angular frequency in rad/s of a propagating signal, μ is the permeability in H/m of the conductor, σ is the conductivity in S/m of the conductor, and f is the frequency in Hz of

a propagating signal. It is clear from (2) that the penetration depth decreases as frequency increases. It is important to note however, as the electric field intensity oscillates, so does the induced current density. In other words, the current is induced inside the conductor which penetrates up to an exponential depth (i.e. the skin depth) at the point of $e^{-x/\delta}$ magnetic field intensity and decays along with the electric field intensity as it oscillates 45° out of phase with the magnetic field intensity. This concept is critical when considering the distribution of current and the associated power losses in a practical conductor which has a rough surface rather than a flat surface. This would effectively isolate the current flow within the surface profile of the conductor as a function of frequency. The challenge is then to describe and predict how an irregular surface impacts conductor losses when the current density is not uniform and oscillates harmonically in time.

2.2 The Morgan-Hammerstad Empirical Fit

An early work that addressed the impact of surface roughness on conductor losses was written by Samuel Morgan and published in 1949 [3]. This research was inspired by existing measurements that observed conductor losses exceeded the predictions of (1) at 1 GHz and increased with higher frequencies, even after $R_{conductor}$ was calculated to account for a reduced skin depth. The approach was to analyze hypothetical transverse and parallel grooves in an imagined "rough" surface since there were no SEM instruments available in 1949. The study was simplified by choosing imagined rectangular and triangular grooves, and then extending them infinitely for a two-dimensional analysis rather than three since computers had not been developed in 1949 (Figure 2.1).

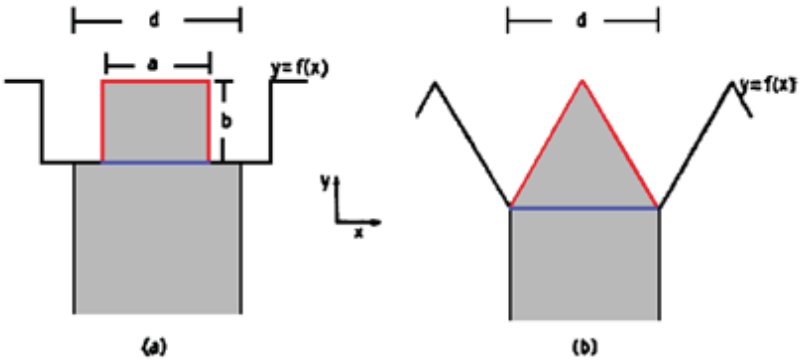


Figure 2.1 (a) Rectangular and (b) triangular surface grooves.

The red surface perimeter was varied to a maximum of twice the length of the blue path labeled *d* in Figure 2.1. Some later engineers have incorrectly interpreted this picture as if the electric field intensity propagating in the x direction in Figure 2.1 caused current traveling parallel to the grooved surface would need to travel along the longer red path of the transverse conductor grooves compared to a flat surface blue path. This concept led those engineers to conclude that increased conductor losses at microwave frequencies are caused by an increased current path length, effectively resulting in additional Joule heating for induced eddy currents. Morgan also analyzed electric field intensity in grooves parallel to the direction of propagation (i.e. the x direction) and concluded the power dissipation attributed to them was 36% of the impact attributed by transverse grooves.

In an effort to apply Morgan's work with a more practical calculation for high-speed copper channel designers, Erik Hammerstad presented an empirical fit to Morgan's transverse grooves as:

$$\frac{P_{rough}}{P_{smooth}} = 1 + \frac{2}{\pi} arctan\left[1.4\left(\frac{\Delta}{\delta}\right)^2\right] \quad (4)$$

where $\frac{P_{rough}}{P_{smooth}}$ is the ratio of power loss caused by a rough conductor versus a perfectly flat conductor, and Δ is the RMS deviation from a perfectly flat surface [4] [5]. This Morgan-Hammerstad empirical fit, which is only a mathematical guess to an accurate expression, attempts to describes the impact of a conductor's surface roughness as a function of eddy current flow with a relatively small skin depth at high frequencies isolated within the RMS deviation of the surface (Figure 2.2).



Figure 2.2 Current density isolated within the RMS surface roughness.

2.3 Problems with the Morgan-Hammerstad Empirical Fit

There is no scientific basis for the $arctan$ function in (4); it is simply a **guess** of a function that empirically fits Morgan's two-dimensional data. This function's asymptotic maximum of 2.00 roughly agrees with Morgan's results since Morgan chose a maximum increased path length (i.e. the red perimeter in Figure 2.1) of 2.00. In practice however, the surface roughness can impact power loss greater than a factor of 2.00. Also, (4) does not consider power loss which may be contributed by parallel grooves. Although Morgan considered the impact of parallel grooves to be 36%, Hammerstad chose to ignore it. Using Hammerstad's empirical fit, high-speed bus designers have been able to predict conductor losses within practical error up to about 4 GHz. However, these predictions were observed to break down as bus speeds approached 8 Gbps [6]. Specifically, performance measurements indicated conductor losses were greater than predicted when

using the empirical fit, implying that the fit tends to underestimate these losses with a growing error trend for all frequencies greater than a few GHz (Figure 2.3) [7].

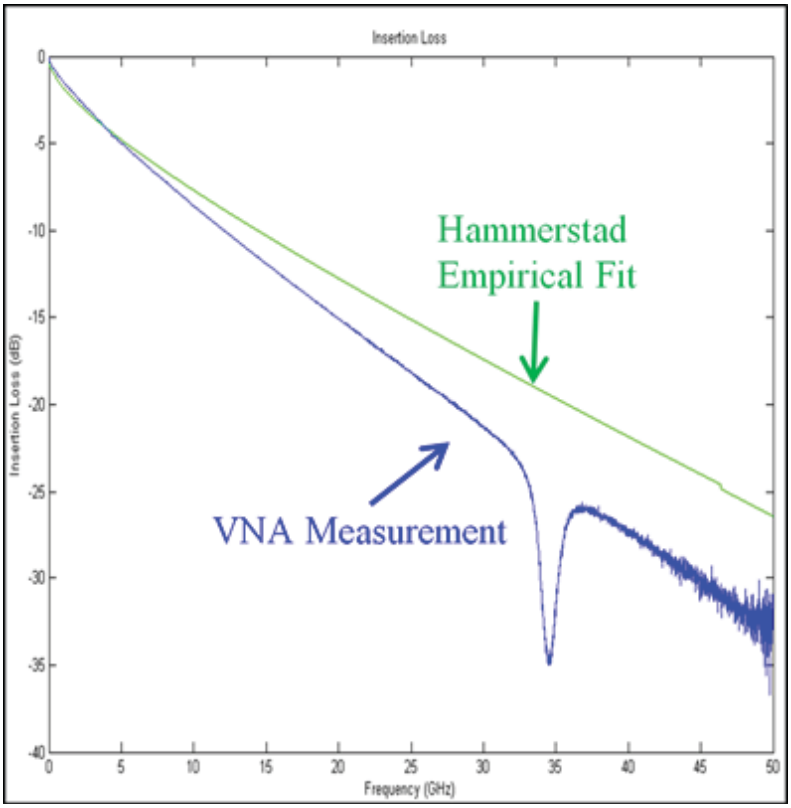


Figure 2.3 Hammerstad Fit vs. VNA measurement of 7" microstrip.

Any simple modification to (4) will not adequately solve this logical problem because there is a fundamental flaw in the premise behind the empirical fit. Morgan's two-dimensional transverse grooves assume the skin depth follows the surface profile (i.e. skin depth is normal to the surface at any point), causing the current to travel a farther distance. While it is true that a reduced cross section and increased length would increase Joule heating (1-2), it cannot be true that the current density follows the surface profile (Figure 2.4).

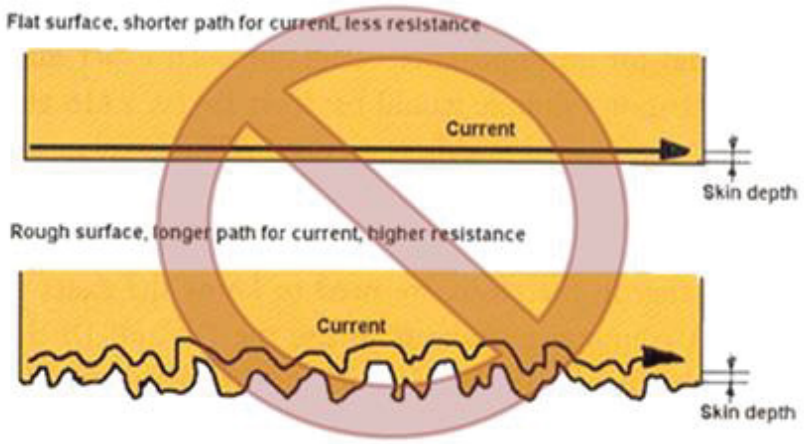


Figure 2.4 Incorrect current path for a rough surface with skin depth. [8]

In order for Figure 2.4 to be true, 1 of these 2 observations must be true:

1. Propagation delay between a transmitter and receiver increases.
2. Causality and in some instances principles of relativity are violated.

Since the propagation delay between a transmitter and receiver does not increase as a function of surface roughness, we are left with the contradictions to causality and relativity. It is important to remember that the surface current density is induced by Gauss's Law applied to a propagating electric field intensity in the horizontal direction. To begin with causality alone, there is no mechanism for surface current density to reverse when it encounters a hook like structure without the field reversing. Likewise, current density cannot instantaneously flow vertically when it encounters a vertical structure without the field somehow pausing, which would then violate Faraday's law even if it were possible. Relativity can be discussed with a single substrate media such as FR-4 where a propagating electric field is traveling a 1/2 the speed of light. Then when reconsidering Morgan's equilateral triangular surface, the propagating electric charge density would need to travel at the speed of light since the distance traveled would be

doubled, as illustrated in Figure 2.1. Worse off, as the permittivity of the media decreases (e.g. Teflon ≈ 2.08) or the surface roughness increases beyond 2.00, charge density would need to travel **faster** than the speed of light. Since neither of the conditions necessary to support Figure 2.4 is met, it is clear that the Hammerstad empirical fit is not a physical model of surface roughness but rather a convenient rule of thumb that works for some frequencies. It is not surprising then that the empirical fit tends to break down at some frequency, which happens to be around 4-5 GHz for a microstrip transmission line. While there has been value in the empirical fit for designers, higher frequency designs need to consider a first principles method for modeling conductor losses.

In order to calibrate our understanding of current density in a high-speed circuit, the current density should be thought of as eddy currents induced by a surface charge density that's caused by a propagating signal electric field intensity displacing electrons, transverse to the surface, rather than a discrete current traveling along the surface path as shown in Figure 2.4. This idea is a bit more intuitive when considering an isolated conducting feature near the conductor but not in contact (Figure 2.5).

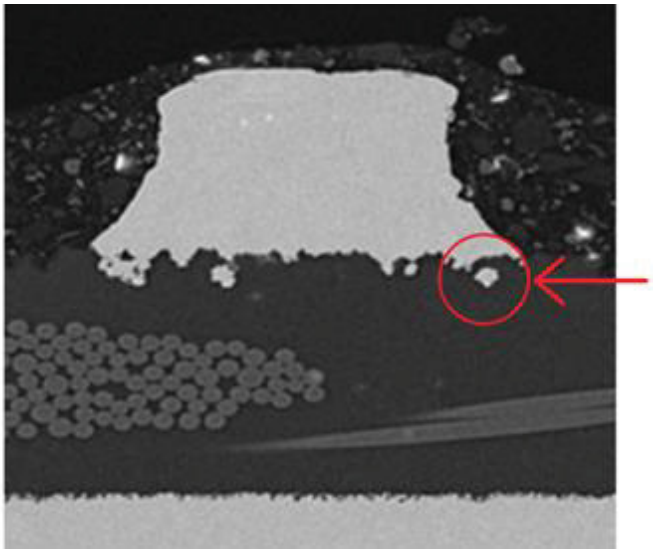


Figure 2.5 Cross sectional view of isolated copper below a microstrip.

If current were to flow discretely through the conductor, there would be no way for current to also travel through an isolated feature. It is quite clear that any current residing in this feature would be induced eddy currents. Likewise, the power loss caused by the surface roughness can be thought of the same way as the isolated feature. Since eddy currents are directly proportional to the frequency

$$\sigma\nabla \times \vec{E} = -\nabla \times \vec{J} = -j\omega\mu\sigma\vec{H} \tag{5}$$

(marginally simplified by assuming a large conductivity), where $\vec{E}$ is the electric field intensity in volts/m, $\vec{J}$ is the electric current density in amperes/m^2, and $\vec{H}$ is the magnetic field intensity in. amperes/m, an increase in eddy currents induced over an increased surface area at high frequencies would result in higher losses, rather than increased resistance over length (Figure 2.6).

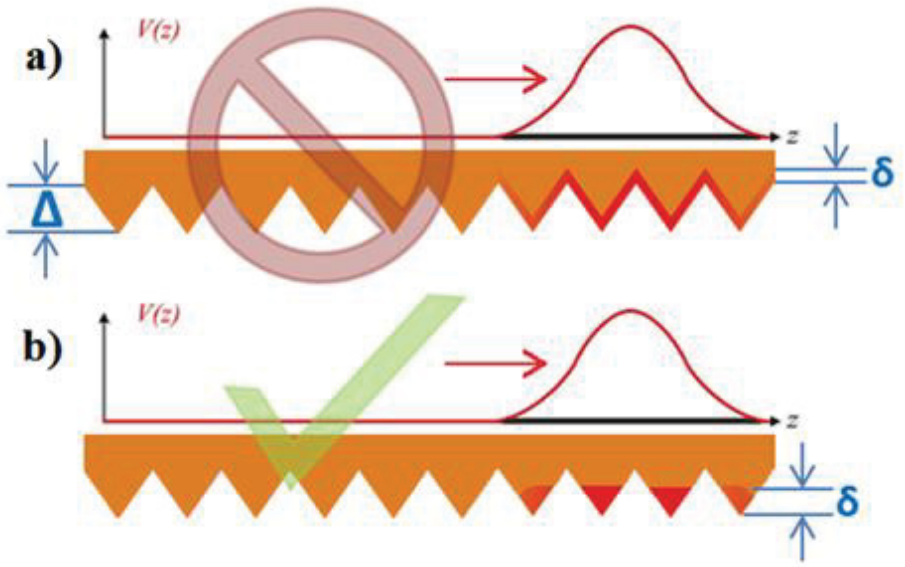


Figure 2.6 (a) Traditional vs (b) fundamental current density in high-speed conductors.

The integral form of Faraday's equation highlights the double integration of the magnetic flux density $\vec{B}$ over a surface area

$$\oint_c \vec{E} \cdot dl = -\frac{d}{dt} \iint_s \vec{B} \cdot dS \tag{6}$$

as opposed to the single length dimension used in the empirical fit. This idea changes our traditional view of ohmic losses as determined by RMS surface deviation and skin depth to a fundamentals based view of electromagnetic field losses based on electric field intensity and induced surface charge density as determined by the total surface area. It is the absorption and scattering of these fields from the increased surface area of these irregular features which contribute to conductor losses at high frequencies. For that reason, the geometric features of the conductor surfaces used in high-speed PCB design need to be carefully examined and characterized for accurate conductor power loss modeling.

2.4 Electrodeposited Copper Foil

As concluded in Section 2.3, it is necessary to examine the surfaces of the conductors used in high-speed PCB design. This is almost always a form of electrodeposited (ED) copper foil for its dimensional consistency, peel strength, and electrical characteristics. Today's manufacturer's use 3 main phases to fabricate these foils (Figure 2.7).

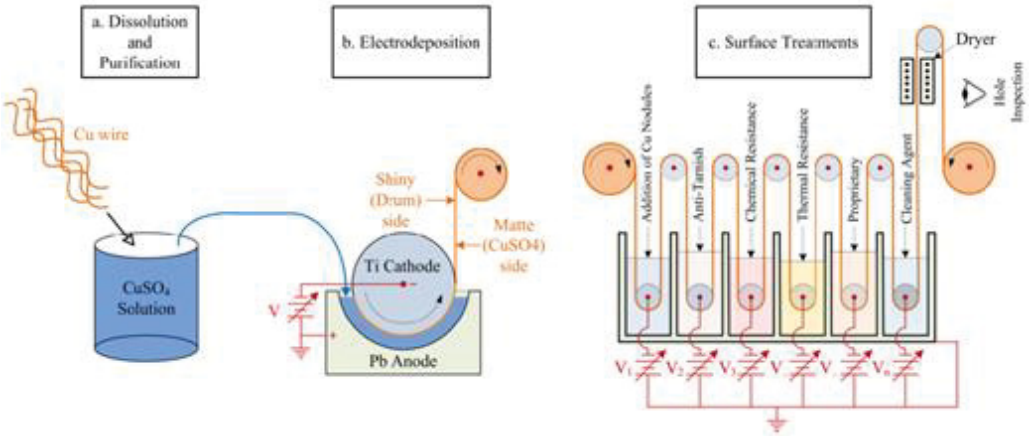


Figure 2.7 Three phases of ED copper foil fabrication. [9]

The electrodeposition and surface treatment phases (b and c in Figure 2.7) play key roles in determining the surface roughness of the ED foil. To begin, there are 2 sides of the foil made during the electrodeposition phase; the "drum side" and the "matte side". The surface roughness of the drum side (also known as the "shiny side" in Figure 2.7 b) is determined by the roughness of the drum, or titanium cathode, itself. These drums are polished to have an extremely smooth surface which creates the "low profile" side of the ED foil with an average deviation in the z-axis height as low as 0.3 μm (Figure 2.8).

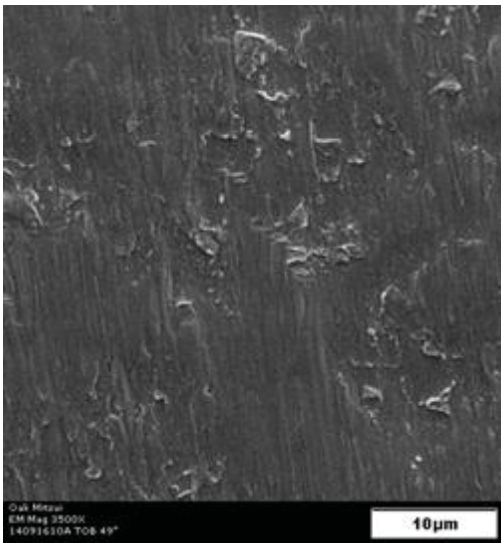


Figure 2.8 Oak-Mitsui Untreated Drum Side 0.5 oz MLS GIII HTE foil 3500x.

The surface roughness of the matte side is determined by how uniformly the copper grows outward from the drum. Several factors contribute to this surface such as the flatness of the base (i.e. the drum), the purity of the copper sulfate ($CuSO_4$), the uniformity of the electric field, the pH and temperature of the solution, and the time allowed for growth as determined by the electrodeposition over potential and current. Since so many factors are associated with determining surface of the matte or "high

profile" side of the ED foil, it usually has a larger deviation in the z-axis height typically ranging from 2-25 μm (Figure 2.9).

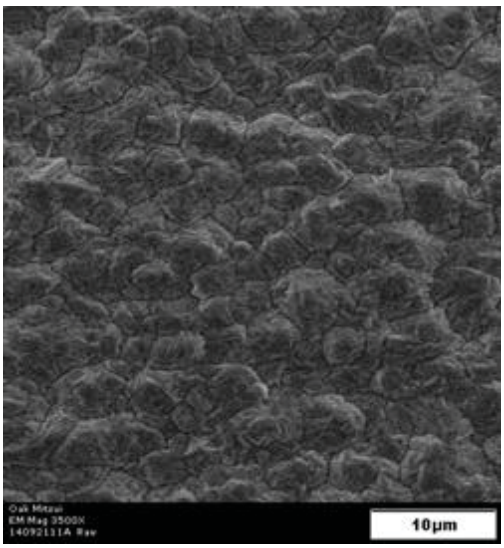


Figure 2.9 Oak-Mitsui Untreated Matte Side 0.5 oz TOB GIII HTE 3500x.

After the electrodeposition phase, a number of surface treatments are given to the foil for mostly mechanical and chemical properties such as anti-tarnish, chemical resistance, thermal resistance, and PCB adhesion. Of particular interest to the electrical properties are the copper dendrites or "anchor nodules" grown on the surface for PCB adhesion. These anchor nodules leave pockets for resin to fill during PCB lamination to increase the mechanical adhesion, referred to by its test name "peel strength". The size and distribution of anchor nodules may be affected by the surface profile fabricated during the electrodeposition phase. While manufacturers typically have a substantial degree of control over this, there are generally 2 different distribution arrangements of anchor nodule growth; one for the drum side and another for the matte side. The anchor nodules on the drum side appear similar in size and distributed uniformly across the surface (Figure 2.10).

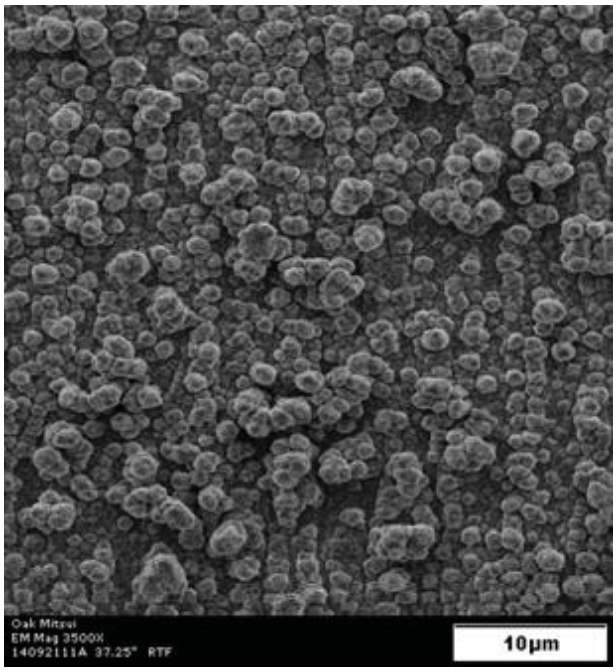


Figure 2.10 Oak-Mitsui Treated Drum Side 0.5 oz MLS GIII HTE foil 3500x.

The anchor nodules on the matte side, however, appear to concentrate towards the peaks of the untreated matte surface (Figure 2.11).

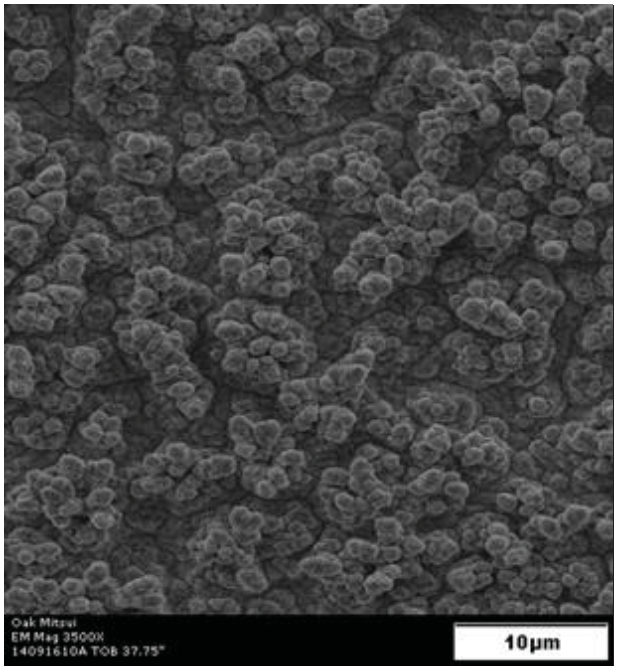


Figure 2.11 Oak-Mitsui Treated Matte Side 0.5 oz TOB GIII HTE 3500x.

Therefore, in order to examine and characterize the surface as concluded in Section 2.3, two components must be analyzed. The first is the surface area of the untreated ED foil before anchor nodules are deposited. The second is the surface area of the anchor nodules themselves. Both analyses are necessary for accurate conductor power loss modeling.

2.5 The Snowball Model

In an effort to describe the impact in terms of the untreated ED foil and the geometric features of any surface anomalies such as anchor nodules as concluded in Section 2.4, Dr. Paul Huray applied a first principles analysis to describe the power loss of a conductor's rough surface with respect to a flat surface

$$\frac{P_{rough}}{P_{smooth}} \approx \left[\frac{\mu_0 \omega \delta}{4}|H_0|^2 A_{Matte} + \sum_{i=1}^{j} N_i \sigma_{total,i} \frac{\eta}{2}|H_0|^2\right] / \left[\frac{\mu_0 \omega \delta}{4}|H_0|^2 A_{Flat}\right] \qquad (7)$$

where H_0 is the local magnetic field intensity maximum in amperes/m, A_{Matte} is the untreated copper foil surface area (drum side or matte side) without anchor nodules m^2, A_{Flat} is the perfectly flat two-dimensional area in m^2, μ_0 is the permeability of free space in H/m, N_i is the total number of surface spherical features of radial size a_i , $\sigma_{total,i}$ is the total absorption and scattering cross sections of radial size a_i spheres in m^2, and η is the intrinsic impedance of the propagating medium in Ω. Taking a closer look at the anchor nodules reveals a stack-up of copper balls which resemble "snowballs" (Figure 2.12).

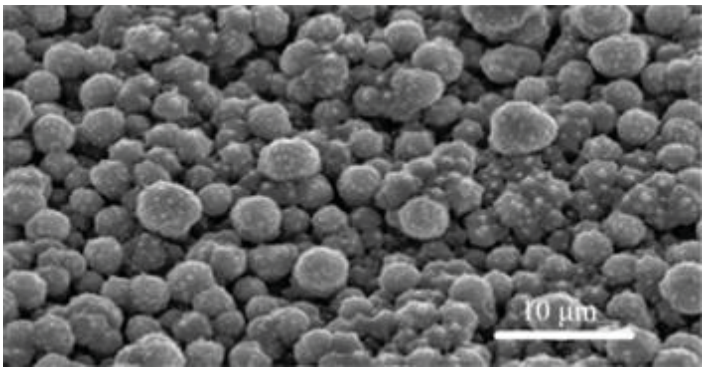


Figure 2.12 Gould Treated Drum Side 5000x.

Approximating the snowballs to spheres and substituting the cross section of a distribution of j different sized snowballs into (7) yields

$$\frac{P_{rough}}{P_{smooth}} \approx \frac{A_{Matte}}{A_{Flat}} + 6\sum_{i=1}^{j}\left[\left(\frac{N_i \pi a_i^2}{A_{Flat}}\right)\Big/\left(1+\frac{\delta}{a_i}+\frac{\delta^2}{2a_i^2}\right)\right] \quad (8)$$

where a_i is the radius of the i^{th} snowball (sphere). In this equation, two assumptions have been made: the absorbed power is so much larger than scattered power that the latter may be neglected and that the dipole terms in the absorption are so much larger than the quadrupole (and higher) terms that the latter may be neglected. The form of (8) clearly isolates the two components concluded in Section 2.4, where $\frac{A_{Matte}}{A_{Flat}}$ describes the ratio of surface area of the untreated ED foil before anchor nodules are deposited to a perfectly flat surface area and the remainder describes the total surface area of the various sized snowballs per unit flat area in the (parenthesis of the numerator) modified by the frequency dependence in the (parenthesis of the denominator). Furthermore, the form of (8) allows for a simple analysis of (7) requiring the surface characterization of only three measurable components (Table 2.1).

Table 2.1 Conductor Surface Parameters of the Snowball Model

Parameter	Description
A_{Matte}/A_{Flat}	The relative surface area without snowballs per unit flat area
a_i	The radius of the i^{th} snowball
N_i/A_{Flat}	The number of snowballs with radius a_i per unit flat area

Channel performance VNA measurements have been used to fit estimations for the 3 parameters of (8) which have demonstrated improved channel loss prediction within

industry and have subsequently been incorporated into commercial electromagnetic field simulators. The qualitative accuracy of the snowball model in dB/in was determined to be within 1% of measured transmission line losses up to 50 GHz using these estimations for a 7" microstrip (Figure 2.13). While a qualitative verification has only been performed up to 50 GHz, the snowball model is predicted to maintain the same accuracy up to a minimum of 100 GHz.

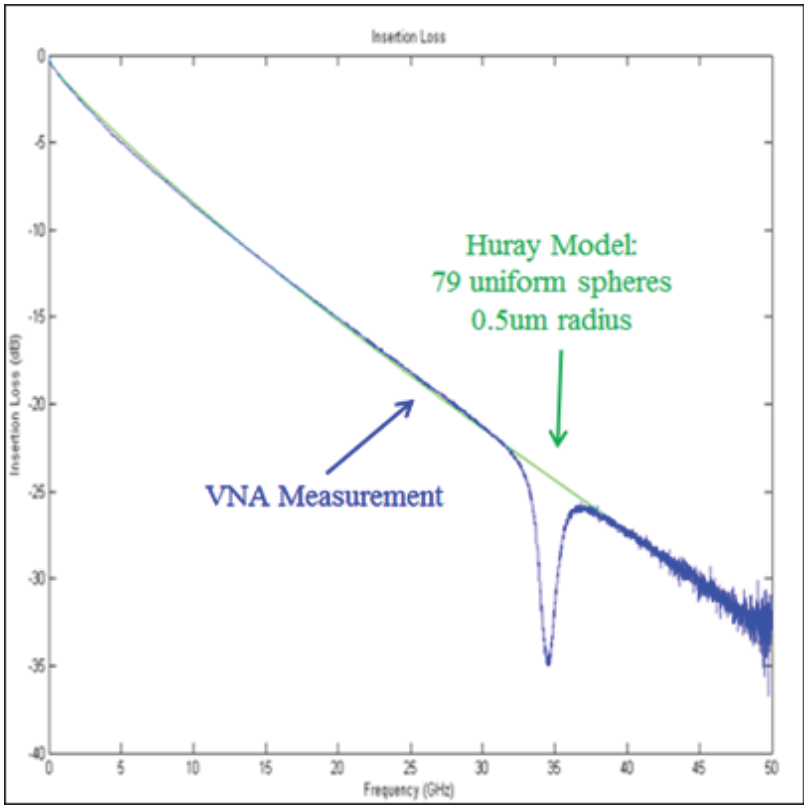


Figure 2.13 Snowball model vs. VNA measurement of 7" microstrip.

2.6 Objections to and Problems with the Snowball Model

The first and perhaps most pressing question about the first principles snowball model is whether it is necessary. The Hammerstad empirical fit to Morgan's two-dimensional data has served bus designers for more than 30 years with acceptable error

up to about 4-5 GHz, depending on the length of the transmission line. From an academic perspective, the Hammerstad empirical fit exploits our mistaken intuition for eddy current paths in high-speed conductors, ignores our conviction in causality, and challenges our fundamental understanding of relativity; as evident from Figures 2.4 and 2.6. Conversely, the snowball model clears this misunderstanding by providing a description which agrees with the standard model of propagating electromagnetic fields in a dielectric (like FR-4) at a boundary with a good conductor (like copper). Without this clarification, scientific and technological advances are easily hindered by misidentifying the root cause of electromagnetic power absorption caused by conductor surface roughness.

This leads to the impact it has on industry when designing higher-speed digital communications using copper channels. To begin, copper channels are plagued with inherently low-pass filter characteristics, which limits trace length to account for signal loss and distortion at high frequencies. Even at lengths as short as 1 inch, the impact of ED foil surface roughness on signal power absorption becomes significant at frequencies above 1 GHz. Although it may be true that the empirical fit has performed well in the past up to a few GHz, Figure 2.3 clearly illustrates its practical limitations. In fact, the loss error in dB/in associated with the empirical fit continues to grow after only a few more GHz, resulting in unacceptably large errors. When comparing the predictions of the snowball model in Figure 2.13 to the predictions of the empirical fit in Figure 2.3, it becomes quite clear that high-speed designs which exceed 5 GHz will require a new model to prevent significantly underestimating signal loss, which can be provided by the snowball model. Underestimating this loss would most certainly lead to unanticipated closed signal “eyes” at the receiver and ultimately inhibit operational success of the

design. In short, future designs at frequencies above a few GHz will need to consider an improved method of predicting conductor loss. The snowball model can fulfill that need for industry designs of the near future. At a minimum, the snowball model can allow designers to accurately predict these losses and design around them. The snowball model provides a clear root cause that future designs can use to mitigate the effects of surface roughness; which is not possible with the empirical fit since the Hammerstad fit is incorrect.

Another concern about the snowball model is revealed with a closer look at the derivation of (8) from (7). When a propagating signal encounters a good conducting sphere, like an approximation for a copper snowball, the signal can either be scattered (outgoing power) or absorbed (incoming power). The total cross section for a copper snowball is then the sum of the absorption and scattering cross sections

$$\sigma_{total} = \sigma_{absorbed} + \sigma_{scattered} \tag{9}$$

If the absorption and scattering cross sections (neglecting quadrupole and higher multi-pole terms) are deduced as

$$\sigma_{absorbed}(\omega) \approx 3\pi k_2 a_i^2 \delta \Big/ \left[1 + \frac{\delta}{a_i} + \frac{\delta^2}{2a_i^2}\right] \tag{10}$$

and

$$\sigma_{scattered}(\omega) \approx \frac{10\pi}{3} k_2^4 a_i^6 \left[1 + \frac{2}{5}\left(\frac{\delta}{a_i}\right)\right] \tag{11}$$

where the wave vector for the non-conducting medium is

$$k_2 = \omega\sqrt{\mu_o \varepsilon_o \varepsilon_{r,2}} \tag{12}$$

and the intrinsic impedance of the propagating medium is

$$\eta = \sqrt{\mu_o / \varepsilon_o \varepsilon_{r,2}} \tag{13}$$

then (8) disregards the scattered cross section. While (7) is entirely capable of considering the effects of scattered power, the calculations become arduous. With this in mind, we can ask: "To what extent can the scattered cross section be ignored?" That is, to determine at what frequencies are the effect of scattered power negligible. By normalizing (10) and (11) to the geometric cross section of an individual snowball of size *i*, their effects can be compared directly as a function of frequency (Figure 2.14).

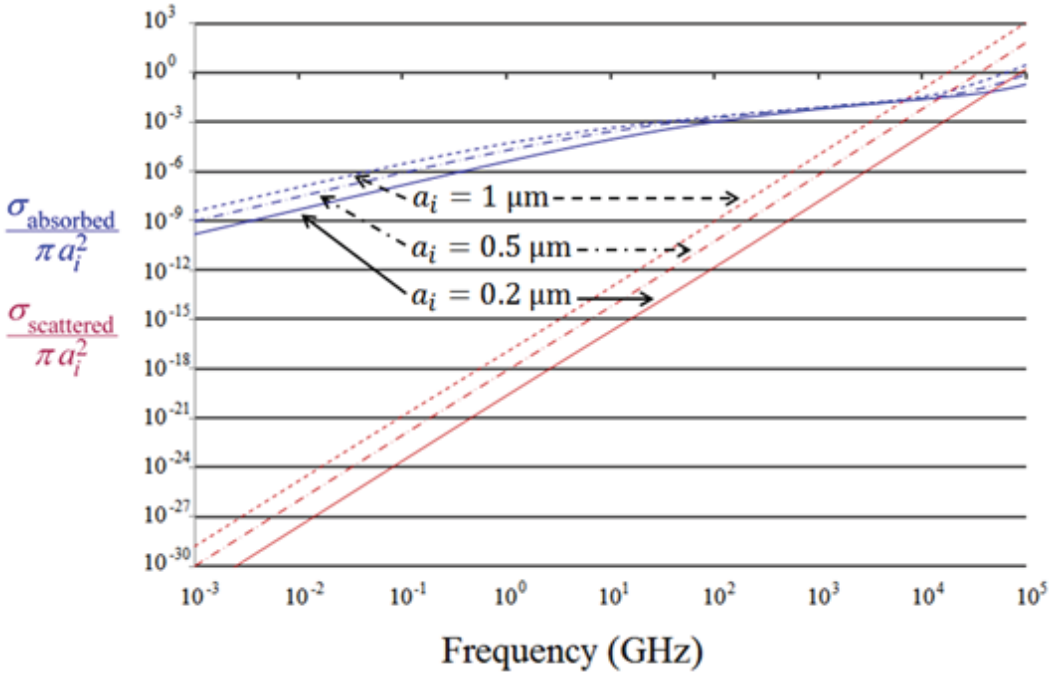


Figure 2.14 Absorption and scattering cross-sections of various size copper spheres. [10]

Selecting a reasonable radial length of $a_i = 0.5$ µm at 100 GHz, we can see that the scattered cross section is only 10^{-11} of the geometric cross section, which is also relatively minute when compared to the absorbed cross section at 10^{-3}. As well, the scattered cross section reduces at a rate of about 10^{-4} per decade of frequency. So, if a 36% impact has been considered 'negligible' by the Hammerstad empirical fit for the past 30 years, it seems sensible to consider a 10^{-9} impact or less as negligible in this approximation.

Therefore, the practical answer to when the scattered cross section can be ignored is: for all frequencies below 100 GHz. Only when frequencies are above 100 GHz, and certainly as they extend into the optical range (i.e. above 10 THz), will the effects of scattered power have a significant impact. Thus, by accepting an error of 10^{-9} to be negligible, (8) is justified in disregarding the scattered cross section.

A problem with the snowball model as it exists today is that industry has had trouble in obtaining the 3 necessary parameters listed in Table 2.1. So far, performance correlation has been made by measuring a channel after fabrication and fitting the parameters to match the measured data. For each of these parameters, assumptions were made about the surface of the ED foil to estimate their values. The assumptions were:

1. Snowball stack-ups can be treated as uniform, average sized spheres.
2. The number of snowballs can be ascertained using a perfectly flat base.
3. The surface (without snowballs) is flat (i.e. $A_{Matte}/A_{Flat} = 1$).

Using SEM images, each of these assumptions can be investigated. The first assumption simplified a_i by assuming all snowballs were the same size and assigning a single value. However, real snowballs have many different sizes (Figure 2.15).

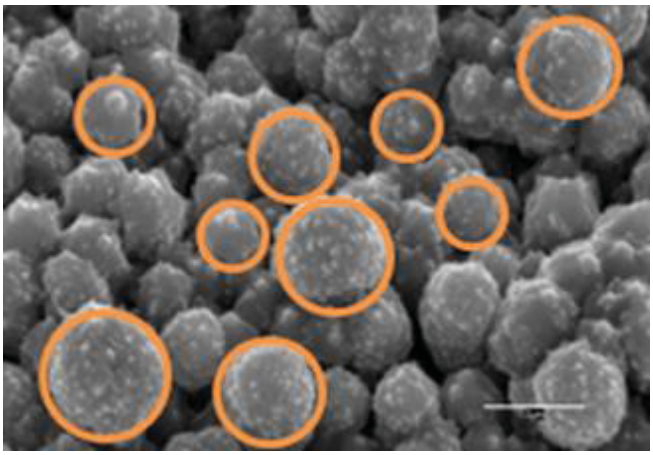


Figure 2.15 Distribution of snowball sizes emphasized with orange rings.

The second assumption simplified N_i/A_{flat} by assuming the base of the stack-up was flat. However, a close look at the surface before snowballs are added, reveals that the base is not perfectly flat (Figures 2.8 and 2.9). This could alter the number of snowballs in a stack up as compared to the estimated number of snowballs in a stack up by reducing the available volume (Figure 2.16).

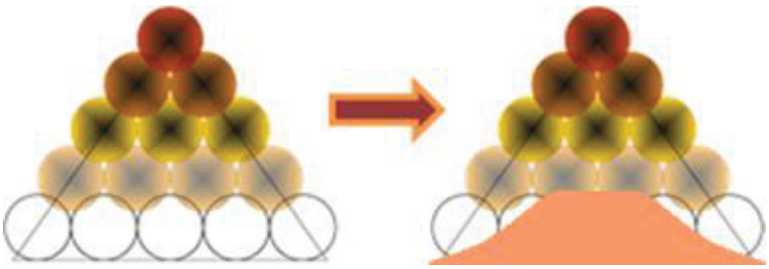


Figure 2.16 Altered number of snowballs in stack-up caused by an irregular base.

Furthermore, the number of snowballs per unit area may change between products since the distribution of snowballs change with different bases (drum side or matte side) as described in Section 2.4 (Figure 2.17).

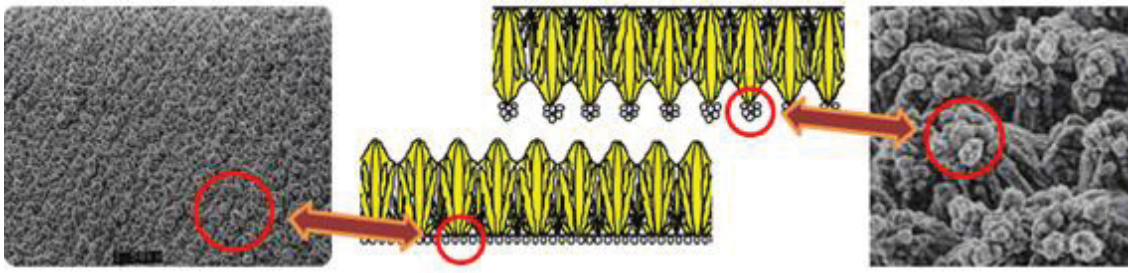


Figure 2.17 Snowball densities on drum side (left) vs. matte side (right).

The third assumption simplified A_{matte}/A_{flat} by assuming it was flat in order to estimate the number of snowballs in the second assumption.

While these assumptions have demonstrated the model's usefulness and potential accuracy to within 1% from 5-50 GHz for channels up to 7", they still exhibit minor deviations between approximations in the snowball theory and measurement as a function of frequency. It is the primary objective of this thesis to address this problem by describing and demonstrating a method of more accurately characterizing the surface of electrodeposited copper foil in order to obtain the 3 parameters for industry implementation.

CHAPTER 3

COPPER FOIL SURFACE CHARACTERIZATION

3.1 IMPACT OF SNOWBALL MODEL PARAMETERS ON CONDUCTOR LOSS

Much of the text and images in this chapter have been submitted for a technical conference paper and presentation [22]. Before considering practical methods of characterizing copper foil to obtain parameters for the snowball model, it is important to determine if a snowball radii distribution is necessary or whether a single average radius is sufficient. This was assessed by calculating (8) for skewed, narrow and wide distributions, and a single average radius for comparison, all with the same total number of snowballs per unit flat area. The Morgan-Hammerstad empirical fit (4) was also calculated for comparison. The small and large skewed distributions did not reveal any surprises. It was expected that a decrease in surface area would result in a decrease in power loss and vice versa. What's particularly interesting is how a normal distribution of snowballs with the same average size as the single average results in a significantly different magnitude and slightly shifted point of inflection. Results show that as the standard deviation of a normal distribution of snowball radii increases, the power loss also increases, even though the average size of the snowballs remains constant (Figure 3.1). If instead, the **volume** of added copper in the nodules is the same for all radii, then the surface area of small radii per unit volume will be much larger for small spheres as for large spheres. Therefore, each of the 3 parameters defined by the snowball model play a distinct role in

predicting conductor losses over a wideband, and should be determined completely and independently for the most accurate results.

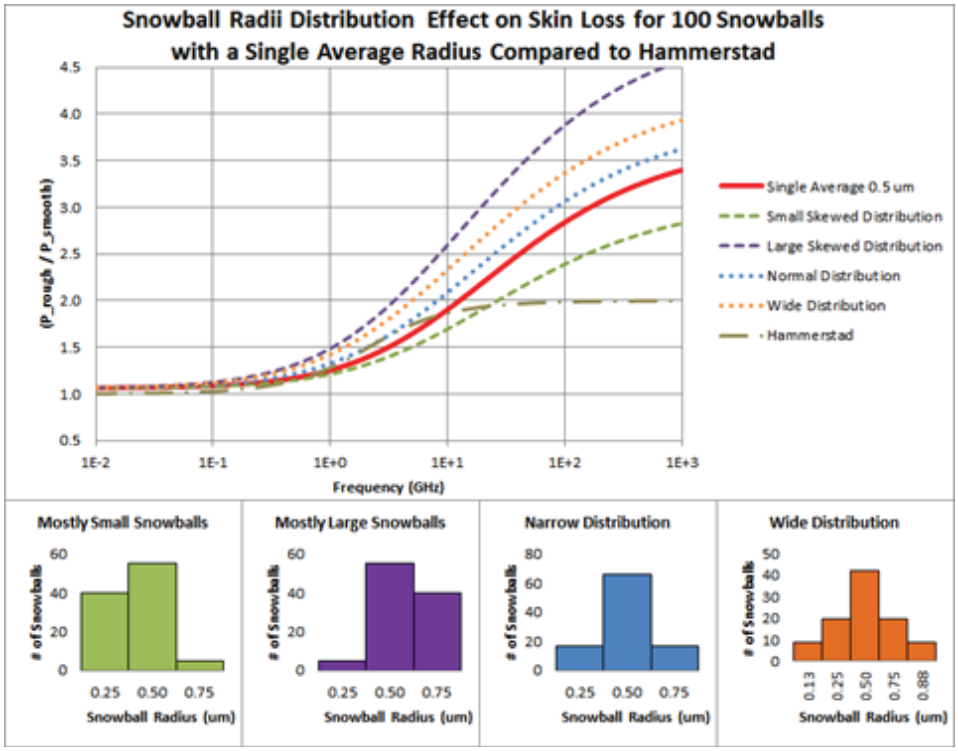


Figure 3.1 Distribution effect on skin loss.

The impact of snowball distributions on power loss is shown in Figure 3.2.

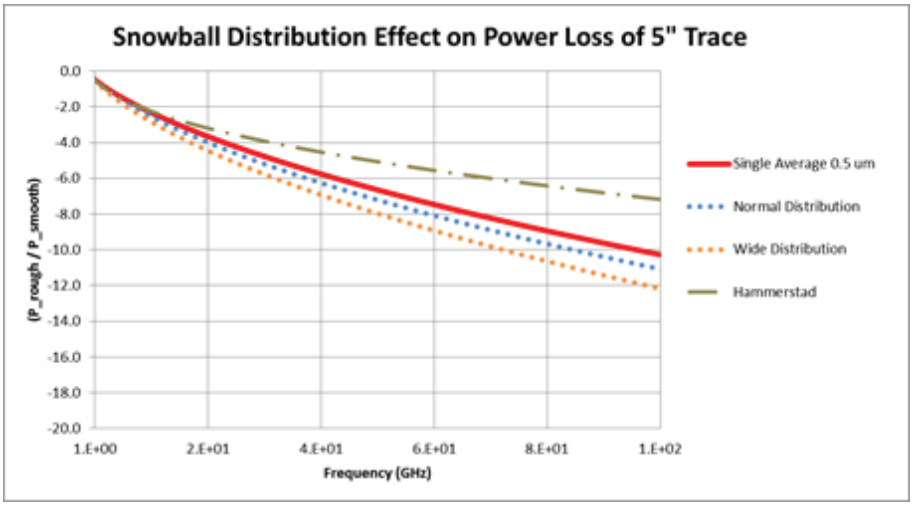


Figure 3.2 Distribution effect on power loss for a 5" microstrip.

Although Figure 3.1 demonstrates the impact of a distribution of snowball radii, it does not clearly demonstrate the impact of a *uniform* radius. That is, a single radius for all N_i that is not necessarily the average radius. This was assessed by comparing the narrow and wide distributions to a single uniform radius with an impact of similar magnitude (Figures 3.3 and 3.4).

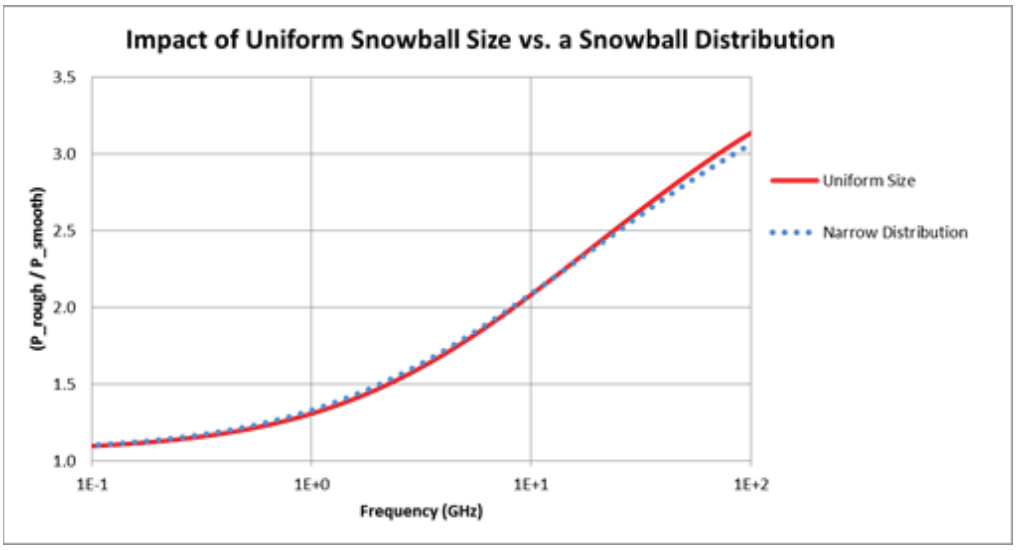


Figure 3.3 Effect of a uniform snowball radius vs. a narrow distribution of radii.

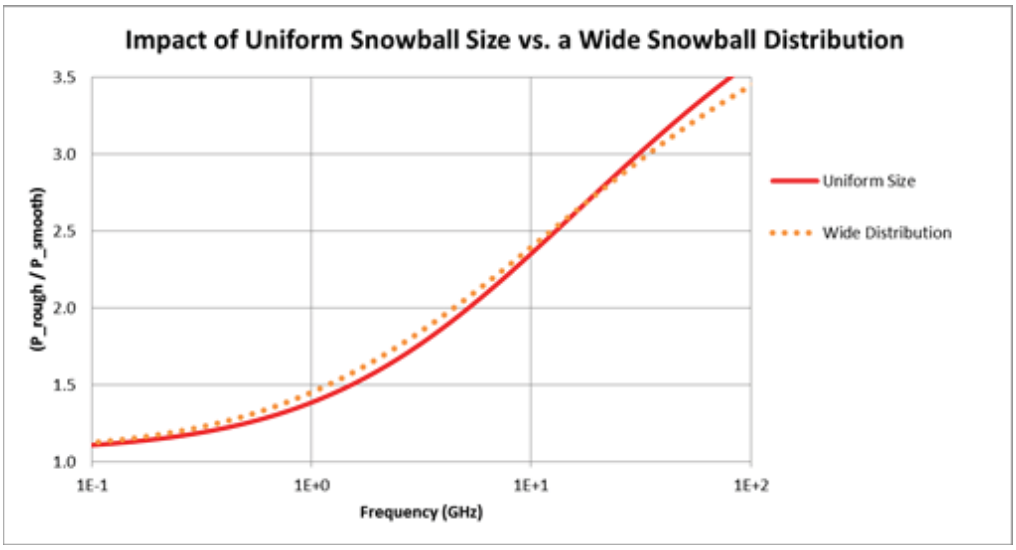


Figure 3.4 Effect of a uniform snowball radius vs. a wide distribution of radii.

Figures 3.3 and 3.4 demonstrate the impact of a distribution of snowball radii as described by Figure 2.14. This low-to-high frequency inflection point suggests an increased impact on conductor loss at relatively low frequencies and a slightly reduced impact at higher frequencies which is also proportional to the standard deviation of the snowball radial length distribution. This data could provide an explanation for the error observed in [7] when correlating the snowball model with VNA measurements.

Another concern of interest is that any characterization performed before PCB lamination might not predict the impact of snowballs shifting during the annealing process. This is not expected to have any significant impact since (8) is not dependent on where the snowballs are located and there is no reason to believe a shift in location would alter the average snowball density N_i/A_{Flat} for the total area.

3.2 Characterizing Treated Copper Foil: a_i and N_i/A_{flat}

In order to obtain a_i and N_i/A_{flat}, images must be taken of the treated copper surface with enough magnification and resolution to easily distinguish the snowballs while maintaining the largest field of view possible. A nice balance was found for these criteria at a magnification of 3500x. There are 2 methods presented for obtaining a snowball distribution. The first method uses images taken by an SEM, and the second uses images taken by a 3D digital microscope. After the images are obtained, there are 3 challenges to extracting a_i and N_i/A_{flat}:

1. Identify all of the snowballs in the image.
2. Count the number of snowballs in the image.
3. Measure the radius of each snowball in the image.

Performing these 3 challenges manually would not be a practical solution. Some common approaches to automating image feature detection include binarization and RGB thresholding to isolate the foreground from the background, usually after clustering and filtering [11] [12] [13]. However, it was found that these methods did not prove reliable for this type of analysis since they often missed snowballs in the filtered background and clumped neighboring snowballs together in the foreground. Since the snowballs are approximately spherical, and thus circular in a 2D image, a more appropriate choice is a Circular Hough Transform (CHT) [14]. While a CHT can identify partially hidden snowballs, one possible drawback to analyzing a 2D image of the surface is that there may be snowballs completely hidden beneath other snowballs. This may be a concern if the surface had several layers of snowballs. If this is a concern, it may be possible to analyze a cross-section of the foil to determine how many layers of snowballs are stacked and extend the surface distribution to the appropriate number of layers, but this was not performed during this research.

3.2.1 SEM Analysis Method

The SEM used to capture images of the treated copper foil was an SEII v2.3 PCI SEM (Figure 3.5).



Figure 3.5 SEII v2.3 PCI Scanning Electron Microscope (SEM).

The previously recommended magnification of 3500x was chosen since it gave the largest field of view where the snowballs were still readily visible. Five samples were analyzed from 5 positions across the entire width of two rolls of copper foil, 1 treated drum side and 1 treated matte side, illustrated in Figures 2.10 and 2.11 respectively. After SEM images were captured, MATLAB was used to implement a CHT and identify the snowballs (Figure 3.6).

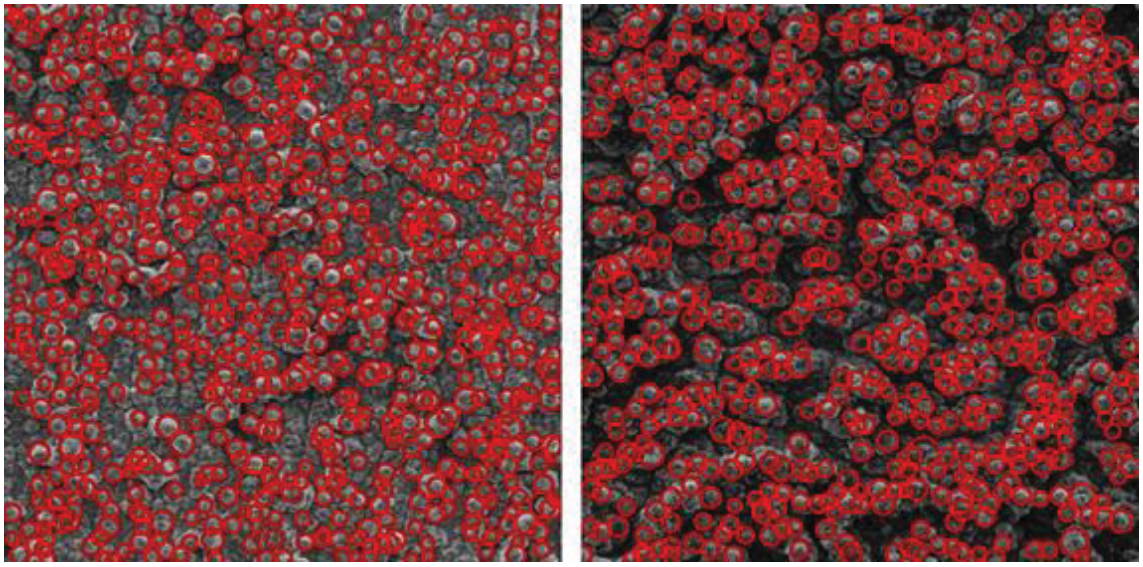


Figure 3.6 MATLAB Snowballs on Drum (left) and Matte (right) Sides.

Although the CHT algorithm in MATLAB is quite simple, some initial care should be taken to fine tune the sensitivity and edge detection threshold for the first image to qualitatively assess whether too many or too few snowballs are being detected. After these are set initially, all subsequent analyses should be standardized to the same settings. After the snowballs are identified, MATLAB can also be used to count the number of snowballs and measure their respective radii (Figure 3.7).

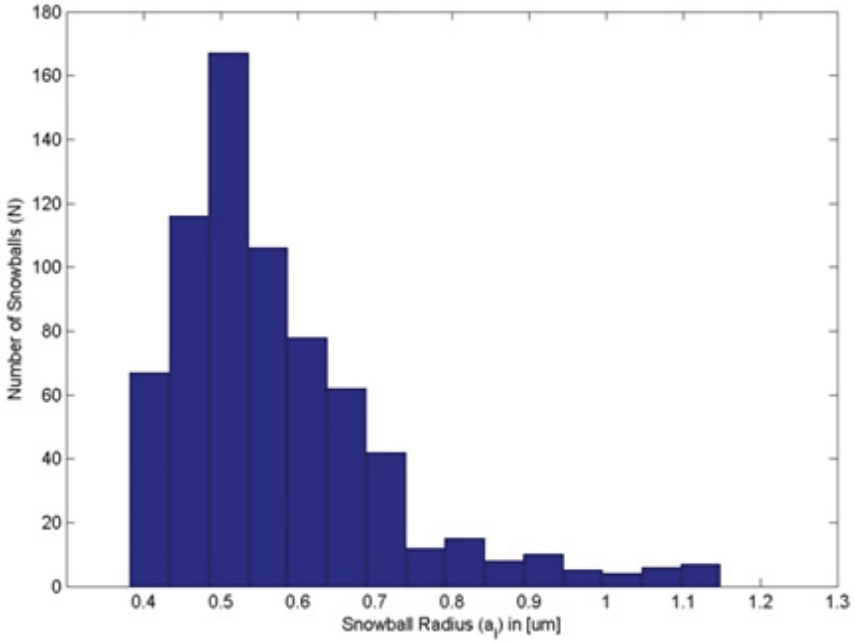


Figure 3.7 Snowball Radii Distribution of Drum Side from SEM Method.

Distributions were divided into 15 bins. Drum side analysis determined an average a_i of 0.54 μm with a standard deviation of only 0.03 μm and an average N_i/A_{flat} of 45 snowballs per 100 μm^2 with a standard deviation less than 3 snowballs per 100 μm^2. Matte side analysis determined an average a_i of 0.56 μm with a standard deviation of 0.09 μm and an average N_i/A_{flat} of 43 snowballs per 100 μm^2 with a standard deviation of 4 snowballs per 100 μm^2 (excluding 1 outlier of 64 snowballs per 100 μm^2).

3.2.2 Digital 3D Microscope Analysis Method

The 3D microscope used to capture images of the treated copper foil was a Hirox KH-8700 E (Figure 3.8).

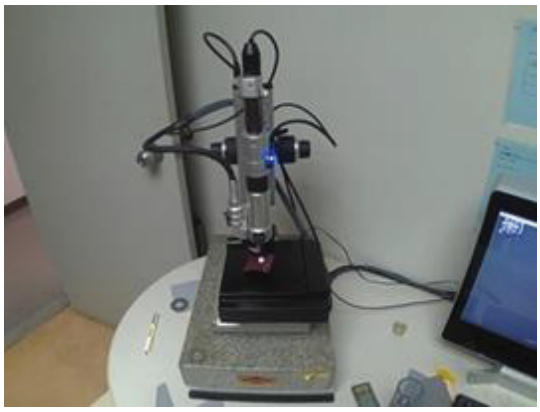


Figure 3.8 Hirox KH-8700 E 3D Digital Microscope.

A magnification of 2800x was chosen since it provided the clearest image. One factor that proved difficult to overcome was vibration. The base of the microscope features a vibration absorber and the included software offers a digital signal processing (DSP) anti-vibration filter that provided some needed stability, but the setup could benefit from additional support from something like an isolated anti-vibration table. Again, 5 samples from 5 positions across the entire width of two rolls of copper foil, 1 treated drum side and 1 treated matte side were analyzed.

After the microscope images were captured, the system's accompanying software was used to identify the snowballs and determine the distribution of their radii. With measurement and image processing tools built in to provide a complete solution, this is certainly a convenient option. In particular, the software provides a particle counter. Unfortunately, the only algorithms provided for counting particles (or in this case snowballs) is binarization or RGB thresholding. Nonetheless, after images were captured, the provided software was used to identify the snowballs using binarization (Figure 3.9).

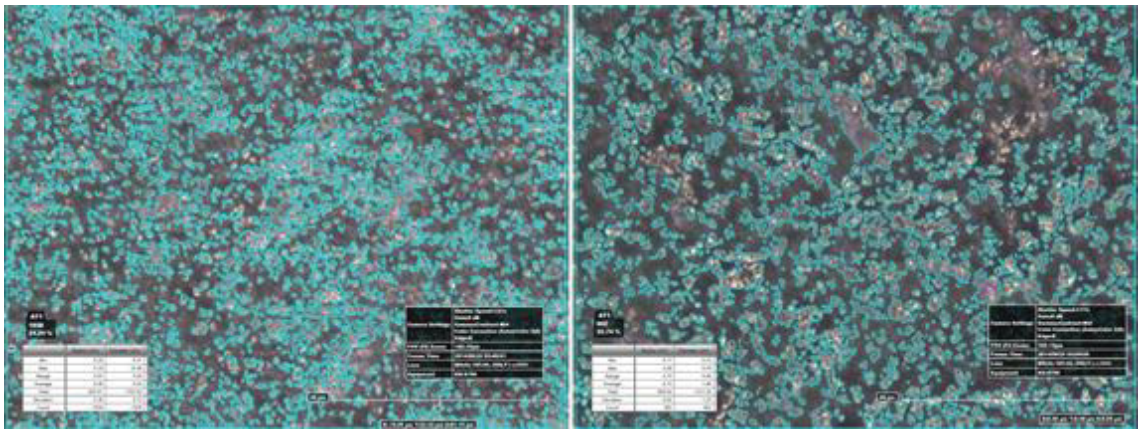


Figure 3.9 Microscope Snowballs on Drum (left) and Matte (right) Sides.

Unlike the MATLAB process, it was necessary to manually tune the binarization filters to qualitatively isolate the snowballs for each image. This can be time consuming and disrupts the automation process. As well, using different settings for each measurement decreases measurement precision (or repeatability), which could lead to increased standard deviation between similar measurements. Furthermore, Figure 3.9 provides a good example of how some snowballs are missed in the "background" while snowballs in the "foreground" are often clumped together when using binarization to count snowballs. Although the system's software cannot directly determine the snowball distribution, it does provide some immediate calculated statistics such as the total area ratio which can be used to improve the precision between measurements. Furthermore, the software allows all of the data and any measurements to be exported as a csv file. What's particularly nice about this capability is that it provides visibility of each measurement. Therefore, impractically large or small measured radii can be filtered out. However, there are 2 caveats to filtering this data. First, though this process may eliminate outlier radii, it will also eliminate the total number and thus total surface area of

the snowballs. Second, there is no inherent justification for choosing which radii are actually too large or too small. In consideration for the stated limitations and caveats, two results are provided. Both results used the previous SEM measurements to justify filtering all radii less than 0.3 μm and greater than 2 μm. Snowball counting and distribution binning was then performed with MATLAB (Figure 3.10).

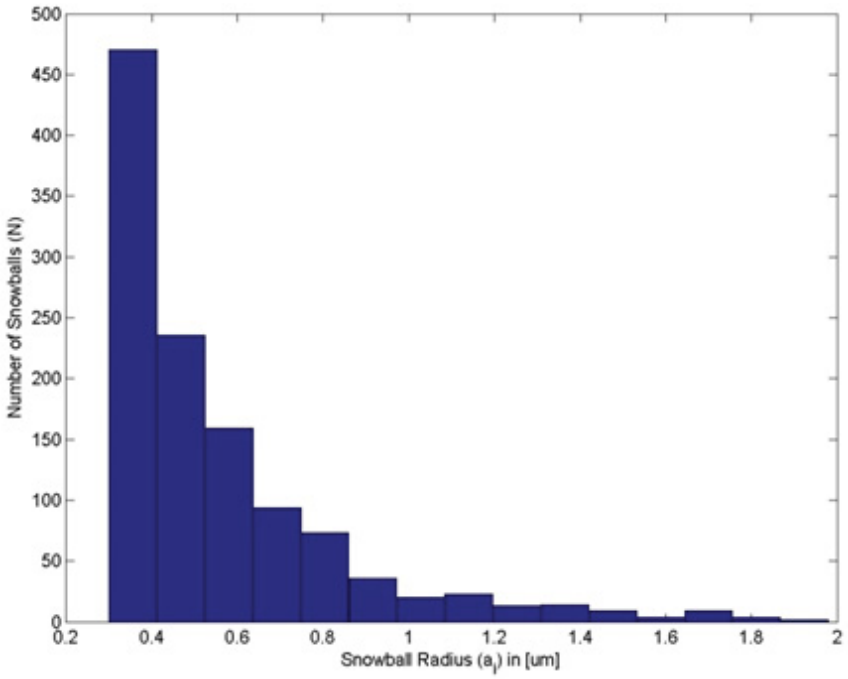


Figure 3.10 Snowball Radii Distribution of Drum Side from Microscope Method.

With no further adjustments or filtering other than what was previously stated, the drum side analysis determined an average a_i of 0.59 μm with a standard deviation of only 0.03 μm and an average N_i/A_{flat} of 11 snowballs per 100 μm^2 with a standard deviation of 4 snowballs per 100 μm^2. Matte side analysis determined an average a_i of 0.70 μm with a standard deviation of 0.08 μm and an average N_i/A_{flat} of 10 snowballs per 100 μm^2 with a standard deviation of 3 snowballs per 100 μm^2.

Since most, if not all, of the large radii previously filtered out to determine the snowball radii distribution were potentially neighbor snowballs clumped together during binarization, the distribution of snowballs was scaled to match the total area measured (i.e. the unfiltered area) in an attempt to recover surface area lost during filtering without skewing the distribution. This process does not change the value of a_i or its standard deviation but N_i/A_{flat} does change. The scaled drum side analysis determined 12 snowballs per 100 μm^2 with a standard deviation of 4 snowballs per 100 μm^2. The scaled matte side analysis determined 11 snowballs per 100 μm^2 with a standard deviation of 2 snowballs per 100 μm^2. Clearly this approach did not make a significant difference.

Although the microscope data for a_i closely correlated with the SEM method, it is difficult to know how accurate the method would be with other foils since the binarization method seemed to miss a significant number of snowballs, as evident from a comparison of N_i/A_{flat} between the microscope and SEM methods as well as Figure 3.9. Furthermore, the correlation for a_i was not too surprising since any radius measurement less than 0.3 μm or greater than 2 μm was intentionally filtered out, which was ultimately justified using SEM measurements. None the less, with a few small improvements such as an anti-vibration table, a CHT method for particle counting and the inclusion of statistical software capable of providing a distribution within the system, this method can provide a convenient approach.

3.3 Characterizing Untreated Copper Foil: A_{matte}/A_{flat}

There are 2 methods presented to obtain the A_{matte}/A_{flat} parameter of an untreated copper surface. The first method uses a mechanical profilometer (or perthometer) to measure the length, including all of the surface irregularities, in the x and

y dimensions to calculate the area. The second method uses a stack of images to create a quasi-three-dimensional image taken by a 3D digital microscope and measured using built-in software.

All measurement methods require some method of interpolating the distance between the measured discrete data points. There are 4 interpolation methods presented, which includes a minimum length, an effective maximum length and 2 intermediate lengths. The first interpolation is a simple linear interpolation using the Pythagorean Theorem to define the absolute minimum possible length between 2 points

$$Length_{min} = \sqrt{(Flat\ Length)^2 + (Height)^2} \tag{14}$$

shown in Figure 3.11.

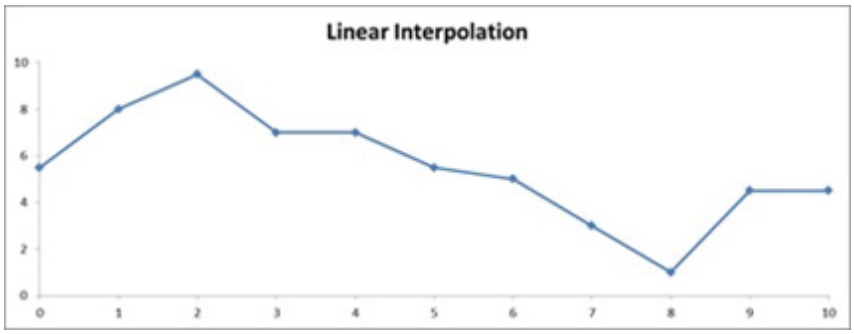


Figure 3.11 Linear Interpolation between Data Points (Absolute Minimum).

The second interpolation method calculates the arc length of a sine wave from 0 to π/2. This was considered a maximum length since it assumes a non-linear path between all points. In truth, this is not an absolute maximum. If the distance between the points is small, in this case less than 1 μm, this would provide a reasonable maximum estimate. However, as the data points move farther apart, this consideration breaks down since there is a higher probability for larger deviations and hence longer path lengths.

Since all of the step sizes between measurements were significantly less than 1 μm, it was considered the maximum length between points. The formula for calculating a non-linear arc length is

$$arc\ length = \int \sqrt{1 + \left(\frac{dy}{dx}\right)^2}\, dx \tag{15}$$

A simple method of implementing (15) for a sin interpolation is to use Simpson's Rule

$$\text{arc length} = \frac{\Delta x}{3}\left[f(x_0) + 2\sum_{j=1}^{n/2-1} f(x_{2j}) + 4\sum_{j=1}^{n/2} f(x_{2j-1}) + f(x_n)\right] \tag{16}$$

where $f(x_n) = \sqrt{1 + \cos^2(x_n)}$ and $n = 10$, shown in Figure 3.12.

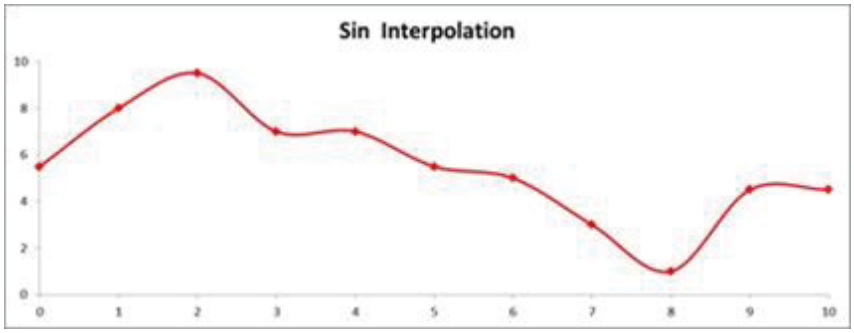


Figure 3.12 Sin Interpolation between Data Points (Effective Maximum).

The minimum and maximum interpolation methods can be used as a tool to determine whether other methods are unrealistic. The third, and **recommended**, interpolation is a hybrid of the first 2 methods. The idea behind this method is, if a linear interpolation underestimates the total length and a sin interpolation overestimates the entire length, then it's reasonable to believe the actual length is comprised of some relatively linear paths and some non-linear paths. Therefore, the hybrid interpolation uses a linear interpolation when $dz/dx = 0$ and a sin interpolation otherwise (Figure 3.13).

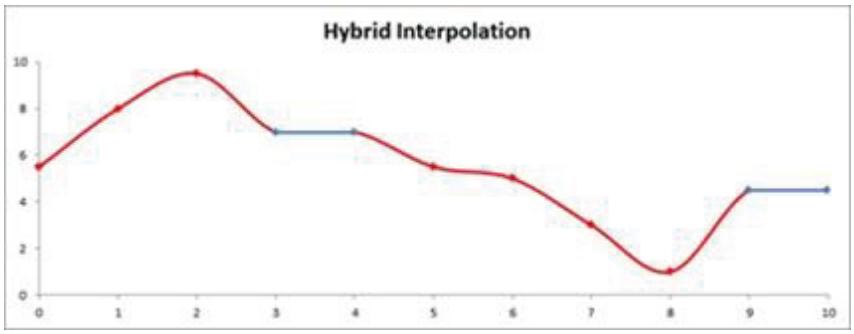


Figure 3.13 Hybrid Interpolation between Data Points (Intermediate).

The fourth method attempts to create a periodic interpolation by averaging the frequent small deviations across less frequent large deviations. This effectively acts like a low pass filter in an attempt to average the total length. There are 2 steps to implement this method. The first step is to binarize the peaks and valleys as determined by the average surface height deviation (R_a). The second step is to calculate the arc length of x^2 using (16), where $f(x_n) = \sqrt{1 + 4a^2x^2}$, $a = \left[4R_a/l_{flat}^2\right]$ and $n = 10$ (Figure 3.14).

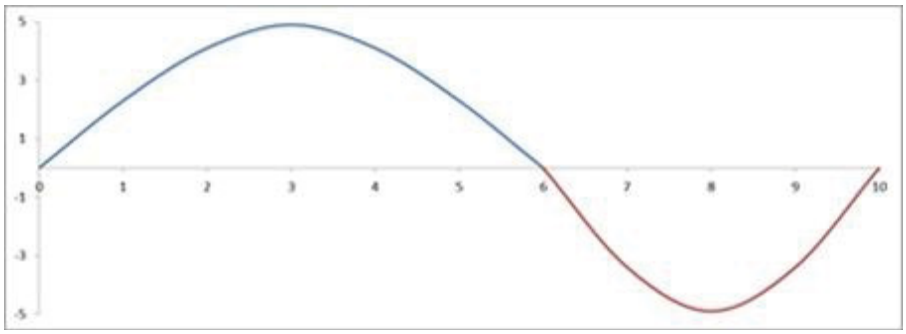


Figure 3.14 Periodic Interpolation of Data Points (Intermediate).

3.3.1 Mechanical Profilometer (Perthometer) Method

The perthometer used to measure the surface profile was a Mahr M2 (Figure 3.15).



Figure 3.15 Mahr M2 Perthometer Controller (left) and Pull Force Meter (right).

As mentioned, width and length measurements are needed to calculate the area. The perthometer does not record discrete data points or automatically calculate the total length. However, it will print a scaled profile on a receipt (Figure 3.16).

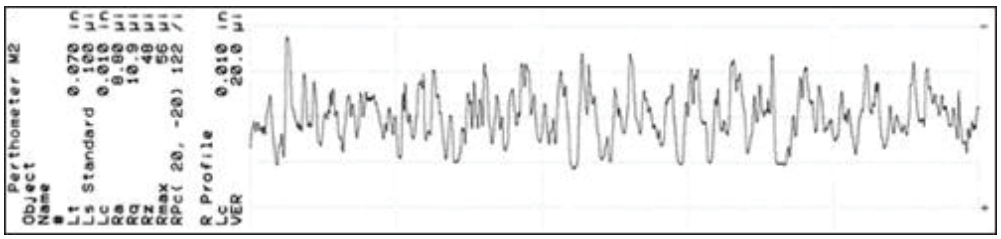


Figure 3.16 Printed Perthometer Surface Profile of Raw Untreated Copper Foil.

After the length and width measurements are obtained, the receipts need to be digitally scanned and converted to discrete data points (Figure 3.17). In order to get a step size between points of 0.335 μm, the receipts were scanned with a resolution of 600ppi.

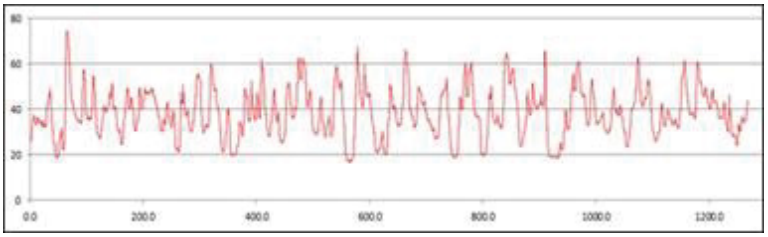


Figure 3.17 Recreation of Surface Profile from Discrete Data Points.

All 4 interpolation methods were implemented in Python and calculated on the fly during data discretization. Ten samples from both sides of raw untreated copper, drum and matte sides, were analyzed from 5 positions across the entire width of two rolls of copper foil. Results for A_{matte}/A_{flat} using the perthometer method were as follows:

Table 3.1 Drum Side A_{matte}/A_{flat}

Interpolation	Linear	Sin	Hybrid	Periodic
Average	1.0224	1.0758	1.0549	1.0222
$\boldsymbol{\sigma_s}$	0.003	0.003	0.003	0.006

Table 3.2 Matte Side A_{matte}/A_{flat}

Interpolation	Linear	Sin	Hybrid	Periodic
Average	1.1095	1.1674	1.1455	1.1165
$\boldsymbol{\sigma_s}$	0.006	0.007	0.007	0.028

The periodic interpolation method was found to unrealistically underestimate lengths and consequently the area, and had the largest standard deviation. Therefore, the **recommended method is the hybrid method**. One possible concern for the perthometer method is that it assumes the same length and width profiles exist across the entire area. However, if this assumption were incorrect it would likely result in a large standard deviation, where these measurements showed only small standard deviations. One way to test this assumption and/or improve the accuracy would be to use an optical profilometer. The methods outlined for a mechanical profilometer can be used directly to calculate the

area between all the data points and summing the complete area like a grid. This would reduce uncertainty of the measurement to a much smaller area, increasing the overall accuracy.

3.3.2 Digital 3D Microscope Analysis Method

The same 3D microscope used to determine a_i and N_i/A_{flat}, a Hirox KH-8700 E, was also used to determine A_{matte}/A_{flat}. This analysis requires the microscope to capture a quasi-3D image of the surface by taking several images at different focal lengths and stacking them, which is a simple automated process (Figure 3.18).

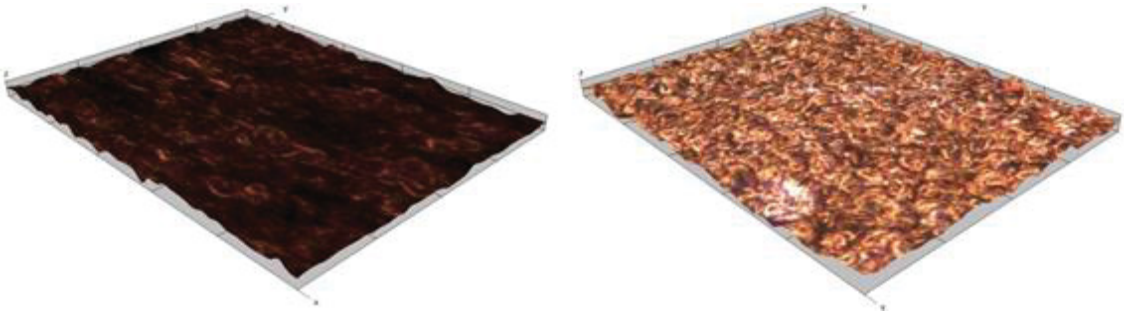


Figure 3.18 3D Drum Side (left) and Matte Side (right) Untreated Copper Surfaces.

Analysis is made easy using the built-in volume measurement software by setting the range and simply clicking on the surface. The software's interpolation algorithm between data points is undetermined. However, the measurement step size can be determined by exporting the data as a csv file, which in this case was 0.057 μm. Five samples from both sides of raw untreated copper, drum and matte sides, were analyzed from 5 positions across the entire width of two rolls of copper foil. Drum side analysis determined an average A_{matte}/A_{flat} of 1.13 with a standard deviation of 0.028. Matte

side analysis determined an average A_{matte}/A_{flat} of 1.17 with a standard deviation of 0.022.

Again, the vibration proved difficult to overcome for this measurement. The number of focal lengths was set to 15 intervals but it can be set higher to reduce the step size in the z-axis and improve the resolution. Beyond 15 intervals, the anti-vibration DSP filter was unable to properly compensate and caused the image to distort. As well, the vibration likely shifted the X-Y plane between focal lengths, further degrading accuracy of the measurements. This may explain the larger surface areas and increased standard deviation as compared to the perthometer method. It also seems unlikely that there is only a 4% difference in surface area between the drum and matte sides. Still, this is a very simple and convenient method that could likely improve its results with an anti-vibration table.

CHAPTER 4

USING CHARACTERIZED PARAMETERS IN SIMULATION TOOLS

Much of the text and images in this chapter have been submitted for a technical conference paper and presentation [22]. As concluded previously, all snowball radii should be determined entirely and described as a distribution, since power loss can change as a function of distribution and standard deviation. Although that conclusion is correct, only a single radius can be used in existing commercially available simulation tools to guarantee a causal impedance boundary function [15]

$$\frac{P_{rough}}{P_{smooth}} \approx 1 + \left(\frac{3}{2}\right)(SR)\left(\frac{1}{1+\frac{\delta(f)}{a}+\frac{1}{2}\left(\frac{\delta(f)}{a}\right)^2}\right) \tag{17}$$

where SR is the Hall-Huray Surface Ratio [16]

$$SR = \frac{4\pi N a^2}{\boldsymbol{A_{flat}}} \tag{18}$$

One concern as previously described for using a single radius rather than a radii distribution is minor deviations as a function of frequency. Such deviations are often negligible for practical purposes under 100 GHz, but can be improved with a distribution. Also, the assumption made by (17) that $A_{matte}/A_{flat} = 1$ may underestimate conductor losses under a few GHz, depending on how close the untreated surface is to being perfectly flat. The approach is then to determine a single "effective" radius that best represents the impact of the complete snowball distribution and untreated surface area on total power loss.

4.1 An Effective Snowball Radius

Implementation of (17) requires that a single **effective** snowball radius be determined, which is not the same as determining the **average** snowball size. To clarify, depending on how the calculation is performed, there may be 2 different averages. An absolute average is determined by averaging all of the measured snowball radii. A bin average is determined by averaging the range or distribution bins. All previously reported averages were the absolute averages. There are then 3 different radii: an '**absolute average radius**', a '**bin average radius**', and an '**effective radius**'.

In order to compare the characterization methods and snowball model predictions to actual insertion loss measurements, the SEM analysis method was used to characterize the snowball distribution of a single image of ED foil manufactured by Gould (Figure 2.15) to correspond with VNA measurements previously obtained by [7]. Characterization obtained a distribution for N_i/A_{flat} with a total density N_{total}/A_{flat} of 32 snowballs per 90 μm^2 (Figure 4.1).

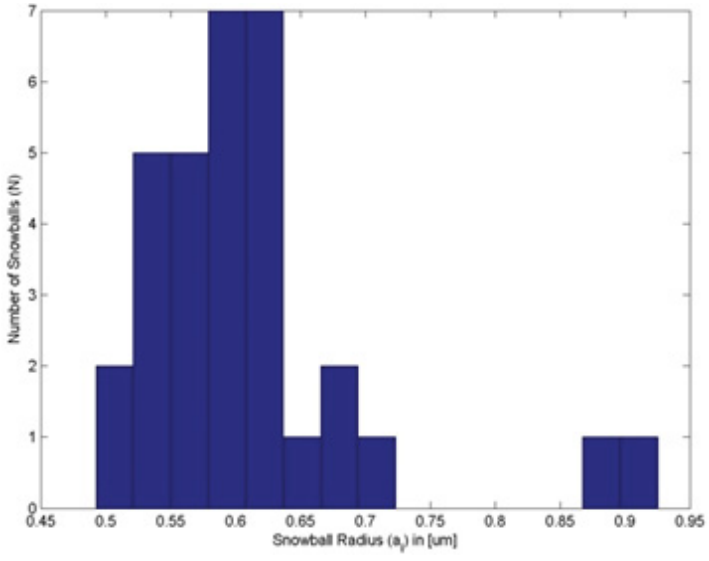


Figure 4.1 Gould Snowball Radii Distribution of Drum Side from SEM Method.

The value for A_{matte}/A_{flat} was assumed to be the same as the Oak-Mitsui copper of 1.055from the recommended hybrid interpolation results in Table 3.1 since a sample of untreated Gould copper was not available. Equation (8) was then calculated for the complete distribution across 15 bins and subsequently calculated for a single **absolute average radius** of 0.6 μm as well as a **bin average radius** of 0.7 μm, all using the same total snowball density N_{total}/A_{flat} of 32 snowballs per 90 μm^2. A single **effective radius** as it pertains to SR, was then calculated with the same total snowball density N_{total}/A_{flat} of 32 snowballs per 90 μm^2, only this time A_{matte}/A_{flat} was set to 1 to agree with (17), and the **effective radius** $a_{effective}$ was manually tuned until the effective curve best matched the complete distribution curve at 0.63 μm (Figure 4.2).

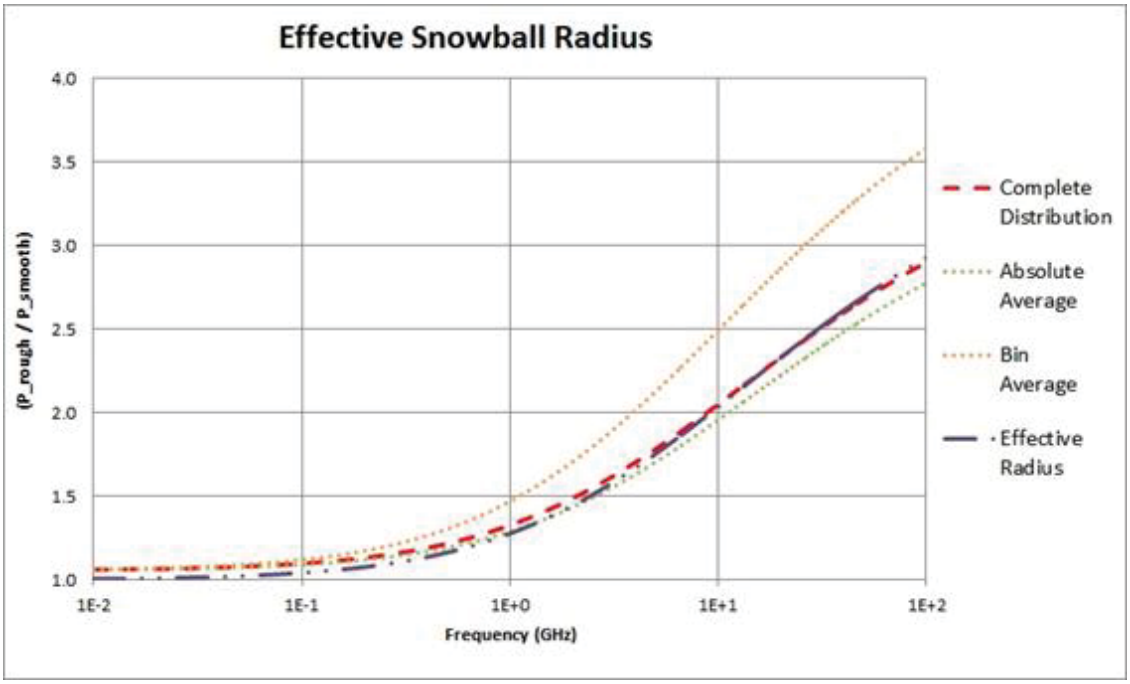


Figure 4.2 Determination of an Effective Snowball Radius.

In this instance, the **absolute average radius** tended to slightly underestimate the impact of the snowballs at high frequencies, while the **bin average radius** tended to overestimate. The proximity of the complete distribution and absolute average curves were caused by the skewed distribution of the snowballs which may change with products and vendors, and thus does not conflict with or supersede Figure 3.1. One convenient relationship between the complete distribution and **effective radius** curves worth noting is a single cross-over frequency. This metric could be leveraged to easily automate the process of fitting the effective radius curve to the complete distribution curve by selecting an appropriate cross-over frequency as an algorithm condition. The 2 parameters necessary to define the finite conductivity boundary in simulation for this particular copper foil were then: an **effective radius** of 0.63 μm and a corresponding **Hall-Huray Surface Ratio** of 1.77 from (18).

4.2 Performance Experiments

To evaluate the accuracy of the **effective radius** and its corresponding **Hall-Huray Surface Ratio** as determined in the previous section, 5" and 7" single-ended microstrips were modeled in Ansys® HFSS™ for insertion loss predictions and compared to actual VNA insertion loss measurements from the same test boards used by [7]. Microstrip and substrate dimensions of [7] were determined as previously measured by [17] (layer 6 - bottom layer) (Table 4.1). The dielectric constant and dissipation factor were $\varepsilon_r = 3.78$ and $\tan\delta = 0.086$ at 2 GHz, as determined from the manufacturer's specifications [18]. The dimensions were modeled exactly and a solder mask was added as illustrated in [17], with $\varepsilon_r = 3.5$ and $\tan\delta = 0.025$ at 7 GHz [15] (Figure 4.3).

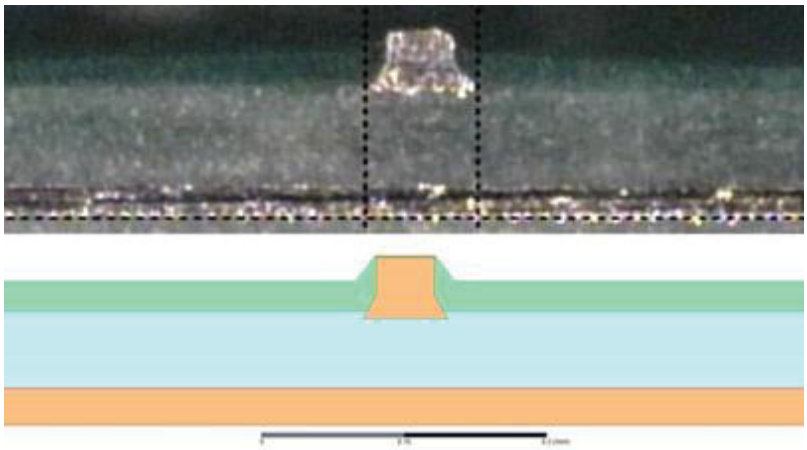


Figure 4.3 Actual Microstrip (top) and Modeled Microstrip (bottom).

Table 4.1 Microstrip Model Dimensions

Feature	Size
Trace Width (top)	2.4579 mils
Trace Width (bottom)	3.6256 mils
Trace Thickness	2.5746 mils
Substrate Thickness	2.8957 mils
Ground Thickness	1.3907 mils

Finally, a conductivity boundary was set for the conductor using the software's Huray Surface Roughness Model with the previously determined **effective radius** of 0.63 μm and **Hall-Huray Surface Ratio** of 1.77 before simulation. The only difference between the 5" and 7" models is the length. For comparison, HFSS offers a modified version of the Morgan-Hammerstad empirical fit, known as the Groisse equation

$$\frac{P_{rough}}{P_{smooth}} = 1 + \exp\left(-\left[\frac{\delta}{\Delta}\right]^{1.6}\right) \tag{19}$$

which also saturates at a maximum of 2.0 like the Morgan-Hammerstad empirical fit, but the Hammerstad equation saturates at a lower frequency [19]. An RMS value of 1.2 μm was used for the Groisse equation, as previously characterized in [7]. It was first simulated at 5" using a flat non-causal substrate model (Figures 4.4 and 4.5).

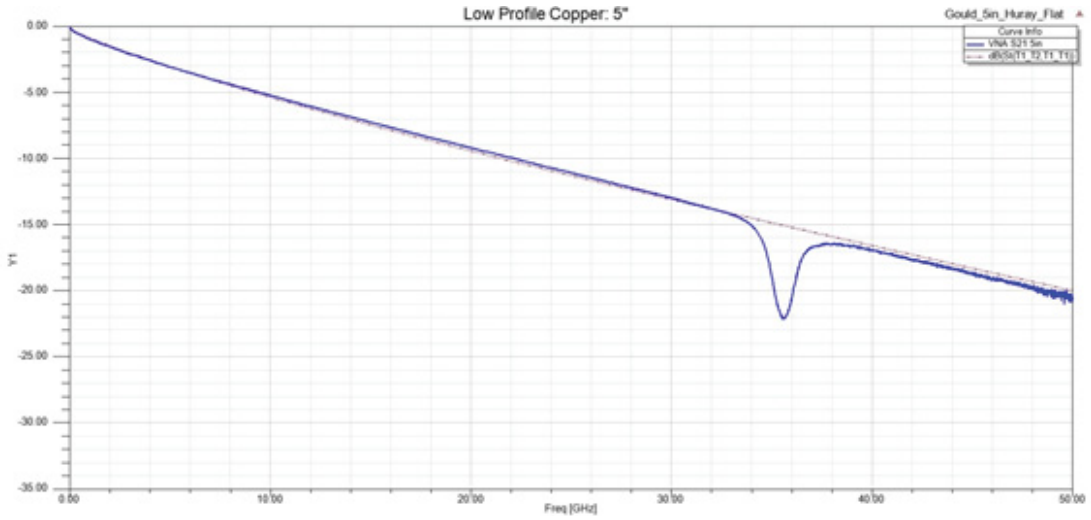


Figure 4.4 5" Huray Model with a flat non-causal substrate vs. VNA Measured.

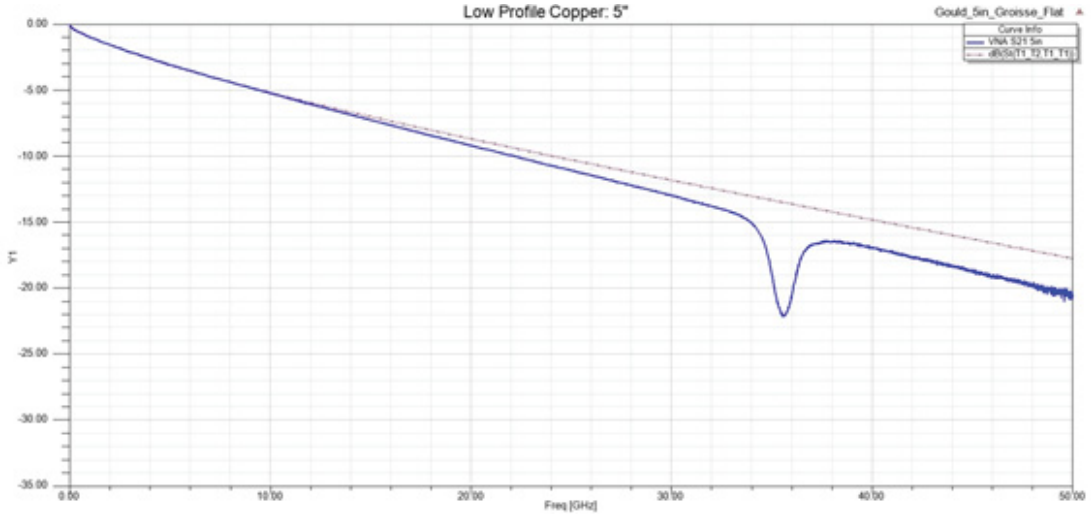


Figure 4.5 5" Groisse Model with a flat non-causal substrate vs. VNA Measured.

Figure 4.4 show a close correlation between the predicted and actual insertion losses up to 50 GHz using the Huray model with a characterized effective radius and a flat non-causal substrate model, with some expected minor deviations as a function of frequency. Figure 4.5 shows the Groisse equation was only capable of predicting up to 12 GHz for a 5" single-ended microstrip. It was then simulated at 7" using a flat non-causal substrate model (Figures 4.6 and 4.7).

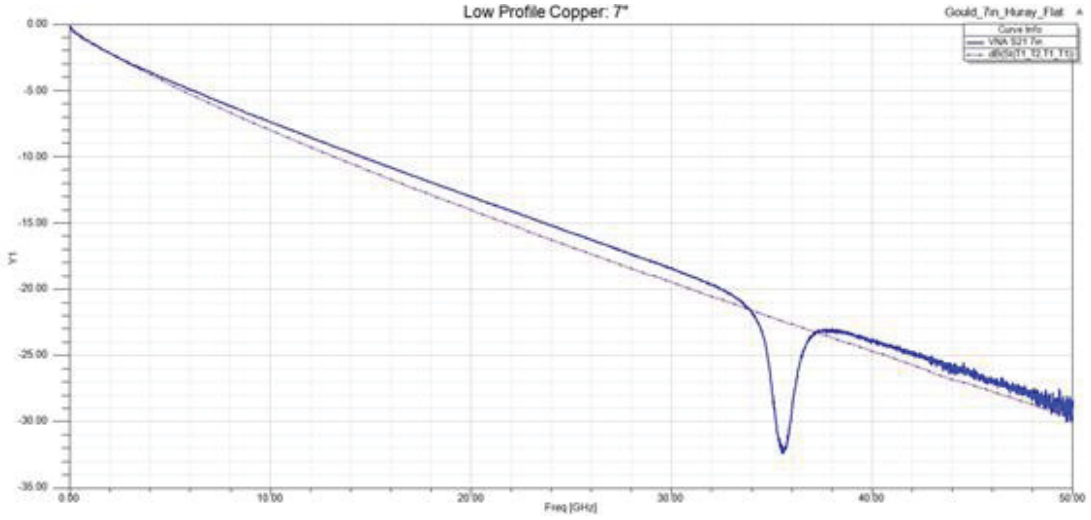


Figure 4.6 7" Huray Model with a flat non-causal substrate vs. VNA Measured.

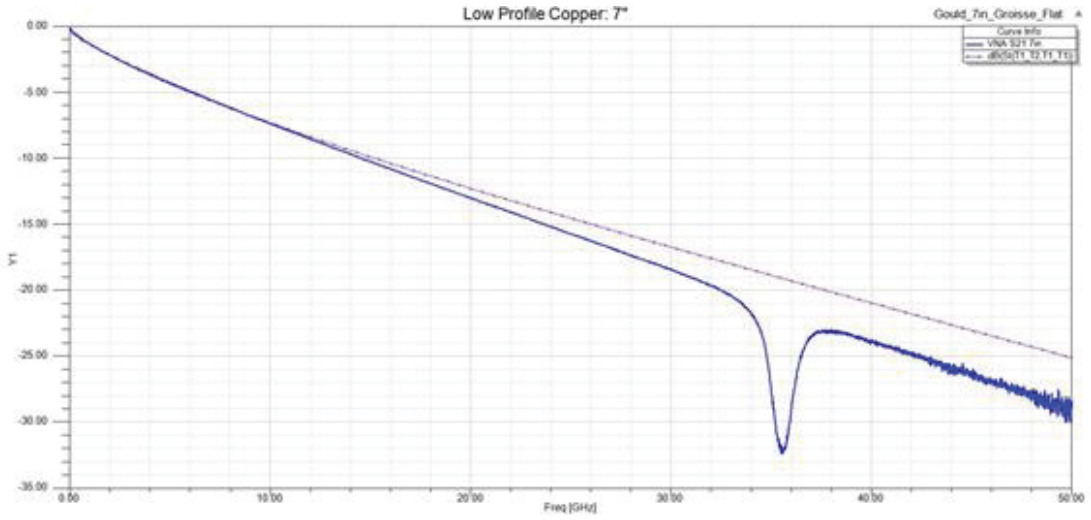


Figure 4.7 7" Groisse Model with a flat non-causal substrate vs. VNA Measured.

Figure 4.6 shows the 7” microstrip was slightly less lossy than predicted by the Huray model with a characterized effective radius and a flat non-causal substrate model, but maintained a relatively close correlation up to 50 GHz. The Groisse equation was again incapable of predicting above 12 GHz. The 5” microstrips were then simulated using a wideband Debye (Djordjevic-Sarkar) substrate model (Figures 4.8 and 4.9).



Figure 4.8 5” Huray Model with a Djordjevic-Sarkar substrate vs. VNA Measured.

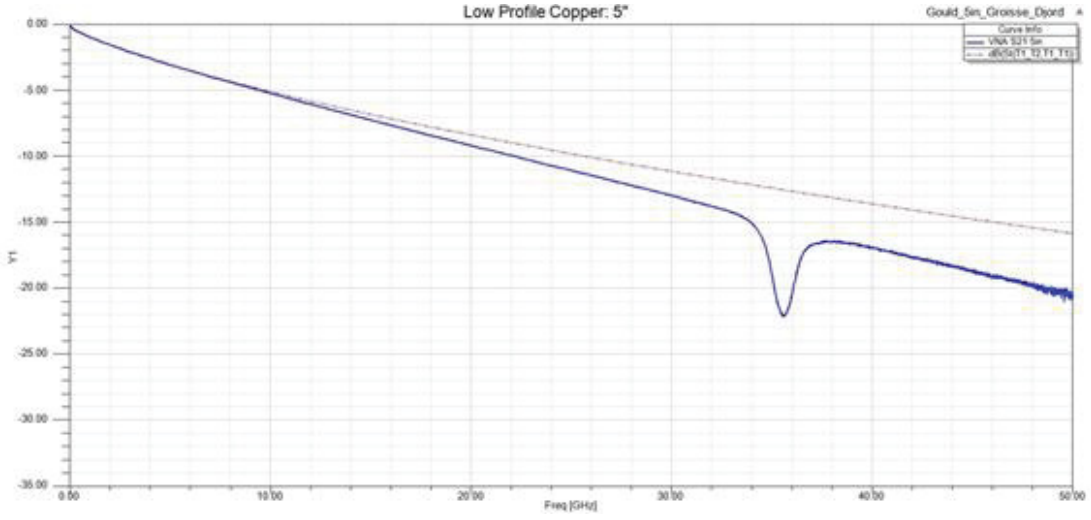


Figure 4.9 5” Groisse Model with a Djordjevic-Sarkar substrate vs. VNA Measured.

Figure 4.8 shows the Huray model with a characterized effective radius was capable of predicting up to about 22 GHz for a 5” trace using a Djordjevic-Sarkar substrate model. Figure 4.9 shows the Groisse model was only capable of predicting up to about 10 GHz using the same trace and substrate. Finally, the 7” microstrips were simulated using a Djordjevic-Sarkar substrate model (Figures 4.10 and 4.11).



Figure 4.10 7” Huray Model with a Djordjevic-Sarkar substrate vs. VNA Measured.



Figure 4.11 7” Groisse Model with a Djordjevic-Sarkar substrate vs. VNA Measured.

Figure 4.10 shows the Huray model with a characterized effective radius was again capable of predicting up to about 22 GHz for a 7” trace using a Djordjevic-Sarkar substrate model. Figure 4.11 shows the Groisse model was only capable of predicting up to about 8 GHz using the same trace and substrate. It is difficult at this point to know the exact root causes for all deviations observed. Figures 4.4 – 4.11 do support the claim that the Huray model was able to improve the predicted insertion loss as compared to the Groisse equation and thus the Morgan-Hammerstad empirical fit. Although only 1 image was used to determine a snowball distribution and a subsequent effective radius, Figures 4.4 – 4.11 also suggest the characterization methods described in this thesis can yield accurate conductor loss modeling at higher frequencies as compared to conventional methods.

It is also unclear at this point if there are hidden snowballs impacting the results or whether multiple layers of snowballs would have a significant effect. Still, it was surprising how well the distribution of only a single image predicted insertion loss when compared to conventional methods. Nonetheless, it seems reasonable to believe that an analysis of several samples could obtain a more statistically reliable representation of the snowball distribution across the entire copper foil surface.

CHAPTER 5

DISCUSSION

5.1 CONCERNS AND ALTERNATIVES

A potential concern for measuring the snowball distribution from SEM images is the obtainable field of view. Since an SEM image can only reveal the surface snowballs, any snowballs hidden between the surface snowballs and the matte foil surface are undetectable. More to the point, there is no way of determining the depth of a snowball stack-up with a two-dimensional image of the surface. Therefore, a method is recommended to estimate the total volume occupied by snowballs within an area if determined necessary. This process will need to be slightly different for the drum and matte sides. For the drum side, an additional cross section image will be needed to determine the height of the stack-up. The height could in turn be used to calculate the total volume occupied by the snowballs (Figure 5.1).

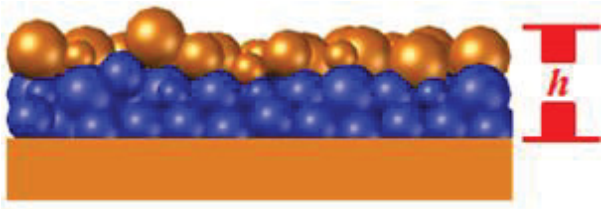


Figure 5.1 Hidden snowballs (blue) beneath surface snowballs on low profile ED foil.

Finally, the size distribution of the surface snowballs can be scaled to match the total volume occupied (Figure 5.2).

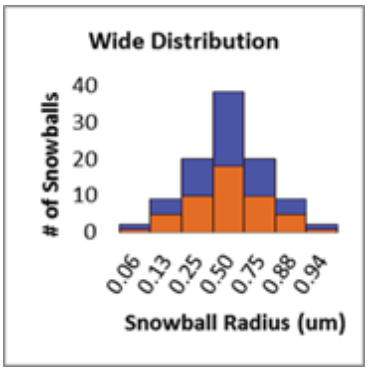


Figure 5.2 Hypothetical distribution (orange) scaled by hidden snowballs (blue).

For the matte side, it may be possible to measure the average diameter of the snowball stack-up at the peak (Figure 5.3).

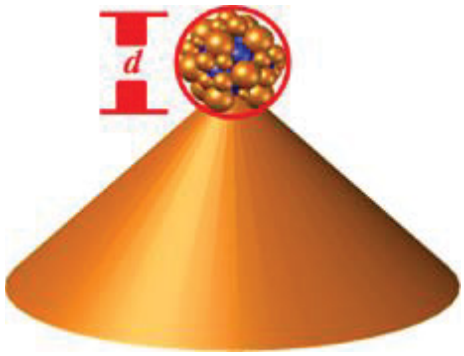


Figure 5.3 Hidden snowballs (blue) beneath surface snowballs on high profile ED foil.

This may need to be corrected if the snowball stack-up is not spherical. The diameter could in turn be used to calculate the total volume occupied by snowballs. Again, the size distribution of the surface snowballs can be scaled to match the total volume occupied (Figure 5.2).

5.2 Known Limitations of this Research

There are a few known limitations of these results. The first is that it ignores the elemental composition of the snowballs. While the snowballs are mostly copper, the

treatment process illustrated as the third phase in Figure 2.7, intentionally add impurities to the surface to provide a number of non-electrical properties such as anti-oxidation, anti-staining or PCB adhesion. One example is called a "treatment of brass" (TOB) which results in a surface composition of copper, carbon, oxygen, silicon, zinc, and nitrogen (Figure 5.4).

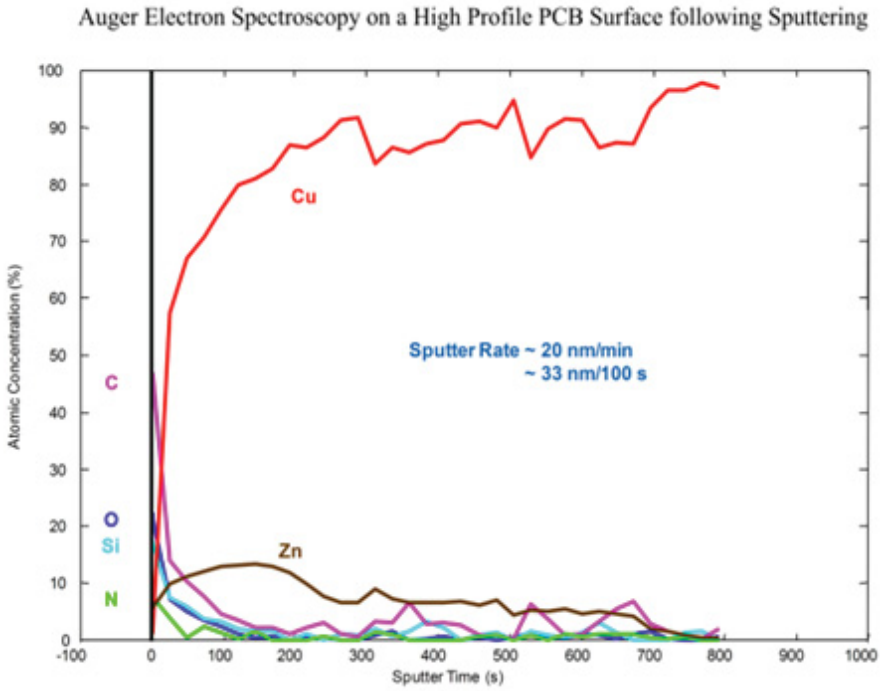


Figure 5.4 Elemental compositions of snowballs after a treatment of brass. [9]

Figure 5.4 shows how the elemental composition of a snowball changes from CuZn (brass) at the snowball surface to almost pure copper around 260 nm deep. Since the conductivity changes with each element, this can affect the snowball model's results, especially at higher frequencies where skin depth decreases. However, many of the impurities added to ED foil are trade secrets and can therefore change from one product to another. As future skin depths become isolated within this region, each manufacturer

will need to be responsible for their own analysis in order to maintain their trade secrets. Therefore, the elemental composition of the snowballs has been deemed beyond the scope of this research.

A second limitation of this research is the assumption that dielectric loss can be accurately determined for VNA correlation. This is especially true since the dielectric used for correlation was FR-4. It has been previously established that the periodic structure of the glass weave within the resin structure can cause additional resonant losses which are not accounted for in simulation [20]. Also, common substrate materials exhibit resonant effects on signal propagation [17]. Since this research is focused on the conductor losses, this known limitation has also been deemed beyond the scope of this research.

A third limitation is that the characterization methods described cannot be performed after lamination. Although this may not have any meaningful effect on the predicted losses, it does pose a challenge to PCB manufacturers. It is unusual for manufacturers to have access to either the material or instruments needed to perform the characterization outlined by this research. None the less, this research provides a considerable milestone towards the advancement of foil characterization as it pertains to accurate conductor loss modeling in high-speed devices. It may be adopted as presented by the manufacturers themselves as the demand for this characterization increases along with higher data rate designs in the near future. It may also be used in future research to develop a solution that is available to PCB manufacturers after the lamination process; such as a hybrid between this research and other RMS surface roughness detection methods from PCB cross sectional images [21].

CHAPTER 6

CONCLUSION AND FUTURE WORK

6.1 CONCLUSION

This thesis demonstrated a few methods of directly characterizing electrodeposited copper foil surface roughness to obtain snowball model parameters for accurate conductor loss modeling. The characterized parameters include A_{Matte}/A_{Flat}, a_i, and N_i/A_{Flat}. In doing so, this research has advanced the existing body of literature on high-speed conductor losses by improving the description of geometric surface profiles for electrodeposited copper foil as well as providing industry with the first steps to directly implement the snowball model. Additionally, this thesis further legitimized the analytic form of the snowball model as it pertains to scattered power, demonstrated the practical impact of its parameters, and revealed a source of existing irregularities between the estimated model parameters and actual performance measurements.

Furthermore, a method of determining a single effective snowball radius, $a_{effective}$ using N_{total}/A_{Flat}, was presented to implement the snowball model in existing commercially available field simulator software. Particular attention was paid to the value of ascertaining a complete distribution of snowball radii and how to determine the most effective radius to best represent the impact of the entire snowball distribution and untreated surface area on conductor loss. Simulation experiments, while limited, still demonstrated reasonable power loss predictions up to 50 GHz using a characterized snowball distribution and effective snowball radius with the snowball model.

6.2 Future Work

The next step could be to fabricate new test boards using the same electrodeposited foil characterized in this thesis to measure insertion loss for comparison with these results. A low loss substrate without periodic structures, such as polytetrafluoroethylene (PTFE) would be preferred to better isolate the conductor loss from the substrate loss. A foil cross section analysis could provide a method of characterizing multiple snowball layers to determine whether they exist and if they have any significant impact on conductor loss. If cross section images can be obtained with reasonable snowball visibility, the methods outlined in this thesis could be extended to analyze a PCB cross section for a post lamination characterization. While perhaps time consuming and simulation intensive, it would be interesting to model the snowballs explicitly in a field simulator and explore the results. Finally, the impact of the elemental composition of the snowballs is still undetermined.

REFERENCES

[1] Intel, "Intel Chips," [Online]. Available: http://www.intel.com/content/dam/www/public/us/en/documents/corporate-information/history-intel- chips-timeline-poster.pdf

[2] B. Lee *et al.*, "Design Optimization for Minimal Crosstalk in Differential Interconnect," *DesignCon 2012*, vol. 2, 2012, pp. 1263-1292

[3] S. Morgan, "Effect of Surface Roughness on Eddy Current Losses at Microwave Frequencies," *Journal of Applied Physics*, vol. 20, 1949, pp. 352-362

[4] E. Hammerstad and F. Bekkadal, "Microstrip Handbook," *ELAB-report, STF44 A74169*, Trondheim, Feb. 1975

[5] E. Hammerstad and O. Jensen, "Accurate Models for Microstrip Computer-Aided Design," *Microwave symposium Digest, IEEE MTT-S International*, May 1980, pp.407-409

[6] S. Hall *et al*., "Modeling Requirements for Transmission Lines in Multi-Gigabit Systems," *Electrical Performance of Electronic Packaging, 2004. IEEE 13th Topical Meeting*, Oct 2004, pp. 67-70

[7] O. Oluwafemi, "Surface Roughness and its Impact on System Power Losses," Ph.D. dissertation, Dept. of Elec. Eng., Univ. of South Carolina, Columbia, SC 2007

[8] P. Huray *et al.*, "Impact of Copper Surface Texture on Loss: A Model that Works," *DesignCon 2010*, vol. 1, 2010, pp. 462-483

[9] P. Huray, *The Foundations of Signal Integrity*. Hoboken, NJ: John Wiley & Sons, Inc., 2010, pp. 109-144, 216-276

[10] E. Bogatin *et al.*, "Which one is better? Comparing Options to Describe Frequency Dependent Losses," DesignCon 2013, vol. 1, 2013, pp. 469-494

[11] H. Kuba *et al.*, "Automatic Particle Detection and Counting By One-Class SVM From Microscope Image," *Proc. Int. Conf. on Neural Information Processing, Lecture Notes in Computer Science*, vol.5507, 2009, pp. 361-368

[12] M.Block and R.Rojas, "Local Contrast Segmentation to Binarize Images," in *Proc. of the 3rd International Conference on Digital Society (ICDS 2009)*, vol.1, no.1, Cancun, Mexico, 2009, pp.294-299

[13] C. Labno, "Two Ways to Count Cells with ImageJ," [Online]. Available: http://digital.bsd.uchicago.edu/resources_files/cell%20counting%20automated%20and%20manual.pdf

[14] T. Atherton and D. Kerbyson, "Size invariant circle detection," Image and Vision Computing, Vol. 17, no. 11, 1999, pp. 795-803

[15] J. Bracken, "A Causal Huray Model for Surface Roughness," DesignCon 2012, vol. 4, 2012, pp. 2880-2914

[16] Ansys, Inc., “HFSS™ Online Help,” pp. 19.104-19.109. [Online]. Available: https://support.ansys.com/portal/site/AnsysCustomerPortal/template.fss?file=/prod_docu/15.0/ebu/hfss_onlinehelp.pdf
[17] C. Jones, “Measurement and analysis of high frequency resonances in printed circuit boards,” MS dissertation, Dept. of Elec. Eng., Univ. of South Carolina, Columbia, SC 2010
[18] Isola, “IS620 Typical Laminate Properties.” [Online]. Available: http://advantage-dev.com/services/docs/Isola%20IS620rev2.pdf
[19] A. Horn *et al.,* “Effect of conductor profile on the insertion loss, phase constant, and dispersion in thin high frequency transmission lines,” DesignCon 2010, vol. 1, 2010, pp. 440-461
[20] P. Pathmanathan, “Power Loss due to Periodic Structures in High-Speed Packages and Printed Circuit Boards,” *Microelectronics and Packaging Conference (EMPC), 2011 18th European*, 12-15 Sept. 2011, pp.1-8
[21] S. De *et al.*, “Semi-Automatic Copper Foil Surface Roughness Detection from PCB Microsection Images,” *2012 IEEE International Symposium on Electromagnetic Compatibility (EMC)*, 6-10 Aug. 2012, pp.132-137
[22] M. Griesi *et al.*, “Electrodeposited Copper Foil Surface Characterization for Accurate Conductor Loss Modeling,” *DesignCon 2015*, 2015

APPENDIX A – PERIODIC INTERPOLATION PSEUDOCODE

1. Find R_z from all data points.
2. Use Boolean operator to identify number of peaks and valleys (defined $R_z/2$) for a cross section in 1 plane.
3. Measure the length of each peak or valley (resolution*N data points) and average for l_{flat}.
4. Repeat for each cross section to find average number of peaks and valleys along with their average lengths.
5. Create a periodic representation of average peaks and valleys per unit length for l_{matte}/l_{flat}.
6. Calculate 1 positive and negative arc length using their respective average lengths and a maximum R_z peak.
7. Multiply by the respective number of peaks and valleys for desired l_{flat}.
8. Repeat steps 1-6 for other plane.
9. The product of steps $7 * 8 = \frac{A_{matte}}{A_{flat}}$.

APPENDIX B – MATLAB CODE FOR OAK-MITSUI IMAGE ANALYSIS

```
% Count & Measure Snowballs
clear;
warning('off','images:initSize:adjustingMag'); % Suppress image size warning
warning('off','images:imfindcircles:warnForLargeRadiusRange'); % Suppress circle
radius range warning
warning('off','images:imfindcircles:warnForSmallRadius'); % Suppress circle radius
minimum warning
folder = 'Images/'; % Image Folder
titleName = input('Enter JPG image file name: ', 's');
fileName = strcat(folder,titleName,'.jpg');
semIn = imread(fileName); % Read Image
semIn = imresize(semIn,850/size(semIn,2)); % Maximize Image
figure; % Open New Figure Window
imshow(semIn,'Border','tight'); % Show Scaled Image
measureDist = imdistline; % Show Line Tool
scalePix = input('Measure the length of the scale with the line tool and enter: ');
scaleLin = input('Enter the actual scale value: ')/scalePix; % Calculate Pixel-to-Linear
Conversion Factor
scaleUnit = input('Enter the scale units: ', 's');
delete(measureDist); % Remove Line Tool
```

```
measureDist = imdistline; % Show Line Tool
cropIm = input('Measure from the top of the image to the top of the bottom info border
with the line tool and enter: ');
semIn = imcrop(semIn,[0 0 size(semIn,2) cropIm]); % Crop Image
delete(measureDist); % Remove Line Tool
close(figure,1); % Close Figure Window
snowballImage = figure; % Open New Figure Window
imshow(semIn,'Border','tight'); % Show Cropped Image
measureDist = imdistline; % Show Line Tool
radiusSmall = floor(input('Measure the diameter of the smallest snowball with the line
tool and enter: ')/2);
delete(measureDist); % Remove Line Tool
measureDist = imdistline; % Show Line Tool
radiusLarge = ceil(input('Measure the diameter of the largest snowball with the line tool
and enter: ')/2);
delete(measureDist); % Remove Line Tool
[centerLocation, radiiPix] = imfindcircles(semIn,[radiusSmall
radiusLarge],'ObjectPolarity','bright','Sensitivity',0.95,'Method','twostage','EdgeThreshold
',0.25); % Find Circles
results = viscircles(centerLocation,radiiPix); % Draw Circles
radiiLin = radiiPix*scaleLin; % Convert pixel radii to linear radii
histogramImage = figure; % Open New Figure Window
hist(radiiLin, 15); % Display histogram of snowball sizes in 15 bins
```

```
histTitle = strrep(titleName,'_','.'); % Format Histogram Title
title(textwrap(strcat('Snowball Distribution for',{' '},histTitle),30)); % Histogram Title
xlabel(strcat('Snowball Radius (a_i) in [',scaleUnit,']')); % Histogram X-axis Label
ylabel('Number of Snowballs (N)'); % Histogram Y-axis Label
[N, ai] = hist(radiiLin, 15); % Store snowball distribution
totalSnowballs = sum(N); % Total number of snowballs
avgSnowballRadius = mean(radiiLin); % Average size of snowballs
saveas(snowballImage,char(strcat('Results/',titleName,{' '},'- Snowballs')),'png'); % Save
Snowball Image
close(snowballImage);
saveas(histogramImage,char(strcat('Results/',titleName,{' '},'- Histogram')),'png'); % Save
Histogram Image
close(histogramImage);
xlName = char(strcat('Results/',titleName,{' '},'- Data','.xlsx')); % Excel File Name
%Store Data in Excel Spreadsheet
xlswrite(xlName,strcat({'Average Snowball Radius in ['},scaleUnit,{']'}),'Sheet1','A1');
xlswrite(xlName,avgSnowballRadius,'Sheet1','A2');
xlswrite(xlName,{'Total Number of Snowballs'},'Sheet1','B1');
xlswrite(xlName,totalSnowballs,'Sheet1','B2');
xlswrite(xlName,strcat({'Snowball Size (a_i) in ['},scaleUnit,{']'}),'Sheet1','A4');
xlswrite(xlName,transpose(ai),'Sheet1','A5:A19');
xlswrite(xlName,{'Number of Snowballs (N_i)'},'Sheet1','B4');
xlswrite(xlName,transpose(N),'Sheet1','B5:B19');
```

APPENDIX C – MATLAB CODE FOR GOULD IMAGE ANALYSIS

```
% Count & Measure Snowballs
clear;
warning('off','images:initSize:adjustingMag'); % Suppress image size warning
warning('off','images:imfindcircles:warnForLargeRadiusRange'); % Suppress circle
radius range warning
warning('off','images:imfindcircles:warnForSmallRadius'); % Suppress circle radius
minimum warning
folder = 'Images/'; % Image Folder
titleName = input('Enter JPG image file name: ', 's');
fileName = strcat(folder,titleName,'.jpg');
semIn = imread(fileName); % Read Image
semIn = imresize(semIn,850/size(semIn,2)); % Maximize Image
snowballImage = figure; % Open New Figure Window
imshow(semIn,'Border','tight'); % Show Scaled Image
measureDist = imdistline; % Show Line Tool
scalePix = input('Measure the length of the scale with the line tool and enter: ');
scaleLin = input('Enter the actual scale value: ')/scalePix; % Calculate Pixel-to-Linear
Conversion Factor
scaleUnit = input('Enter the scale units: ', 's');
```

```
delete(measureDist); % Remove Line Tool
measureDist = imdistline; % Show Line Tool
radiusSmall = floor(input('Measure the diameter of the smallest snowball with the line
tool and enter: ')/2);
delete(measureDist); % Remove Line Tool
measureDist = imdistline; % Show Line Tool
radiusLarge = ceil(input('Measure the diameter of the largest snowball with the line tool
and enter: ')/2);
delete(measureDist); % Remove Line Tool
[centerLocation, radiiPix] = imfindcircles(semIn,[radiusSmall
radiusLarge],'ObjectPolarity','bright','Sensitivity',0.94,'Method','twostage','EdgeThreshold
',0.1); % Find Circles
results = viscircles(centerLocation,radiiPix); % Draw Circles
radiiLin = radiiPix*scaleLin; % Convert pixel radii to linear radii
histogramImage = figure; % Open New Figure Window
hist(radiiLin, 15); % Display histogram of snowball sizes in 15 bins
histTitle = strrep(titleName,'_','.'); % Format Histogram Title
title(textwrap(strcat('Snowball Distribution for',{' '},histTitle),30)); % Histogram Title
xlabel(strcat('Snowball Radius (a_i) in [',scaleUnit,']')); % Histogram X-axis Label
ylabel('Number of Snowballs (N)'); % Histogram Y-axis Label
[N, ai] = hist(radiiLin, 15); % Store snowball distribution
totalSnowballs = sum(N); % Total number of snowballs
avgSnowballRadius = mean(radiiLin); % Average size of snowballs
```

```
saveas(snowballImage,char(strcat('Results/',titleName,{' '},'- Snowballs')),'png'); % Save
Snowball Image
close(snowballImage);
saveas(histogramImage,char(strcat('Results/',titleName,{' '},'- Histogram')),'png'); % Save
Histogram Image
close(histogramImage);
xlName = char(strcat('Results/',titleName,{' '},'- Data','.xlsx')); % Excel File Name
%Store Data in Excel Spreadsheet
xlswrite(xlName,strcat({'Average Snowball Radius in ['},scaleUnit,{']'}),'Sheet1','A1');
xlswrite(xlName,avgSnowballRadius,'Sheet1','A2');
xlswrite(xlName,{'Total Number of Snowballs'},'Sheet1','B1');
xlswrite(xlName,totalSnowballs,'Sheet1','B2');
xlswrite(xlName,strcat({'Snowball Size (a_i) in ['},scaleUnit,{']'}),'Sheet1','A4');
xlswrite(xlName,transpose(ai),'Sheet1','A5:A19');
xlswrite(xlName,{'Number of Snowballs (N_i)'},'Sheet1','B4');
xlswrite(xlName,transpose(N),'Sheet1','B5:B19');
clear;
```

APPENDIX D – MATLAB CODE FOR 3D MICROSCOPE DISTRIBUTION BINNING

```
clear;
folder = 'Spreadsheets/'; % Spreadsheet Folder
scaleUnit = 'um'; % Units
titleName = input('Enter Excel file name: ', 's');
fileName = strcat(folder,titleName,'.xlsx');
dataIn = xlsread(fileName);
histogramImage = figure; % Open New Figure Window
hist(dataIn, 15); % Display histogram of snowball sizes in 15 bins
histTitle = strrep(titleName,'_','.'); % Format Histogram Title
title(textwrap(strcat('Snowball Distribution for',{' '},histTitle),30)); % Histogram Title
xlabel(strcat('Snowball Radius (a_i) in [',scaleUnit,']')); % Histogram X-axis Label
ylabel('Number of Snowballs (N)'); % Histogram Y-axis Label
[N, ai] = hist(dataIn, 15); % Store snowball distribution
totalSnowballs = sum(N); % Total number of snowballs
avgSnowballRadius = mean(dataIn); % Average size of snowballs
saveas(histogramImage,char(strcat('Results/',titleName,{' '},'- Histogram')),'png'); % Save
Histogram Image
close(histogramImage);
xlName = char(strcat('Results/',titleName,{' '},'- Data','.xlsx')); % Excel File Name
```

```
%Store Data in Excel Spreadsheet
xlswrite(xlName,strcat({'Average Snowball Radius in ['},scaleUnit,{']'}),'Sheet1','A1');
xlswrite(xlName,avgSnowballRadius,'Sheet1','A2');
xlswrite(xlName,{'Total Number of Snowballs'},'Sheet1','B1');
xlswrite(xlName,totalSnowballs,'Sheet1','B2');
xlswrite(xlName,strcat({'Snowball Size (a_i) in ['},scaleUnit,{']'}),'Sheet1','A4');
xlswrite(xlName,transpose(ai),'Sheet1','A5:A19');
xlswrite(xlName,{'Number of Snowballs (N_i)'},'Sheet1','B4');
xlswrite(xlName,transpose(N),'Sheet1','B5:B19');
clear;
```

APPENDIX E – MATLAB CODE FOR AVERAGE DISTRIBUTION BINNING

```
clear;
folder = 'Spreadsheets/'; % Spreadsheet Folder
scaleUnit = 'um'; % Units
titleName = input('Enter Excel file name: ', 's');
fileName = strcat(folder,titleName,'.xlsx');
xMin = xlsread(fileName,'A1:A1');
xMax = xlsread(fileName,'A15:A15');
xSpan = xMax - xMin;
xInterval = xSpan/14;
xData = [xMin,0,0,0,0,0,0,0,0,0,0,0,0,0,xMax];
for i=2:14
   xData(i)=xMin + ((i-1)*xInterval);
end
xData = transpose(xData);
yData = xlsread(fileName,'B:B');
barImage = figure; % Open New Figure Window
bar(xData, yData, 1); % Display histogram of snowball sizes
histTitle = strrep(titleName,'_','.'); % Format Histogram Title
title(textwrap(strcat('Snowball Distribution for',{' '},histTitle),30)); % Histogram Title
```

```
xlabel(strcat('Snowball Radius (a_i) in [',scaleUnit,']')); % Histogram X-axis Label
ylabel('Number of Snowballs (N)'); % Histogram Y-axis Label
saveas(barImage,char(strcat('Results/',titleName,{' '},'- Histogram')),'png'); % Save
Histogram Image
close(barImage);
clear;
```

APPENDIX F – PYTHON CODE FOR COMPOSITE SIMPSON'S RULE

```
def arcLengthSinX(mag=1, upper=math.pi, lower=0, n=10):
        '''mag   int      [int]              upper   float    [radians]
        lower   float    [radians]                n        int       [int]'''
        deltaX = (upper-lower)/n
        sumTotal = 0
        sumLoop = 0
        for i in range(n+1):
                xN = lower + (i*deltaX)
                if (i == 0) | (i == n):
                        sumLoop =
math.sqrt(1+(math.pow(mag,2)*math.pow(math.cos(xN),2)))
                elif i%2 != 0:
                        sumLoop =
4*math.sqrt(1+(math.pow(mag,2)*math.pow(math.cos(xN),2)))
                else:
                        sumLoop =
2*math.sqrt(1+(math.pow(mag,2)*math.pow(math.cos(xN),2)))
                sumTotal = sumTotal + sumLoop
        return round((deltaX/3)*sumTotal,4)
```

```
def arcLengthX2(mag=1, upper=1, lower=0, n=10):
        '''mag   int      [int]              upper   float    [radians]
        lower   float    [radians]                n        int      [int]    '''
        deltaX = (upper-lower)/n
        sumTotal = 0
        sumLoop = 0
        for i in range(n+1):
                xN = lower + (i*deltaX)
                if (i == 0) | (i == n):
                        sumLoop = math.sqrt(1+(4*math.pow(mag,2)*math.pow(xN,2)))
                elif i%2 != 0:
                        sumLoop =
4*math.sqrt(1+(4*math.pow(mag,2)*math.pow(xN,2)))
                else:
                        sumLoop =
2*math.sqrt(1+(4*math.pow(mag,2)*math.pow(xN,2)))
                sumTotal = sumTotal + sumLoop
        return round((deltaX/3)*sumTotal,4)
```

APPENDIX G – DERIVATION OF EDDY CURRENT EQUATION

If: $\nabla \times \overrightarrow{H_S} = \overrightarrow{J_S}$

Then the on both sides is: $\nabla\left(\nabla \cdot \overrightarrow{H_S}\right) - \nabla^2 \overrightarrow{H_S} = \nabla \times \overrightarrow{J_S}$

From Gauss's law $\nabla \cdot \vec{H} = 0$, so: $-\nabla^2 \overrightarrow{H_S} = \nabla \times \overrightarrow{J_S}$

From Ohm's law $\vec{J} = \sigma \vec{E}$, so: $-\nabla^2 \overrightarrow{H_S} = \sigma \nabla \times \overrightarrow{E_S}$

From Faraday's law $\nabla \times \vec{E} = \frac{-\partial \vec{B}}{\partial t}$ so: $\nabla^2 \overrightarrow{H_S} = \sigma \frac{\partial \overrightarrow{B_S}}{\partial t}$

Finally, from [3]: $-\nabla^2 \overrightarrow{H_S} = -j\omega\mu\sigma \overrightarrow{H_S}$

So: $\sigma \nabla \times \overrightarrow{E_S} = -\nabla \times \overrightarrow{J_S} = -j\omega\mu\sigma \overrightarrow{H_S}$

As shown in (5).

APPENDIX GRIESI02

ResearchGate Search for publications, researchers, or questions or Discover by subject area Recruit researchers Join for free Login

Conference Paper

A Low Loss X-band Filter Using 3-D Polyjet Technology

February 2015
DOI:10.1109/MWSYM.2015.7166895
Conference: IEEE IMS 2015

Authors:



Fan Cai
Georgia Institute of Technology

wasif khan John Papapolymerou

Request full-text PDF
To read the full-text of this research, you can request a copy directly from the authors.

Download citation Copy link

Citations (31) References (10)

ResearchGate
Discover the world's research
- 25+ million members
- 160+ million publication pages
- 2.3+ billion citations

Join for free

No full-text available

To read the full-text of this research,
you can request a copy directly from the authors.

Request full-text PDF

Citations (31) References (10)

Effects of extreme surface roughness on 3D printed horn antenna

Article Full-text available Jun 2013

Cesar Roman Garcia · Raymond Rumpf · Harvey Tsang · J.H. Barton

View Show abstract

A Broadband, Micromachined Rectangular Waveguide to Cavity-Backed Coplanar Waveguide Transition Using Impedance-Taper Technique

Article Jan 2014

M. Moallem · Jack East · K. Sarabandi

View Show abstract

Development of a Ku-Band Corrugated Conical Horn Using 3-D Print Technology

Article Jan 2014

Jia-Chi Samuel Chieh · Brian Dick · Stuart Loui · John D. Rockway

View Show abstract

AFully Micromachined W-BandCoplanar Waveguide to Rectangular Waveguide Transition

Article

Manos Tentzeris

View Show abstract

A Fully Micromachined W-Band Coplanar Waveguide to Rectangular Waveguide Transition

Conference Paper Jul 2007

Yuan Li · Bo Pan · Manos Tentzeris · John Papapolymerou

View Show abstract

Reduced-size multilayer X-band filters with stacked resonators on a flexible organic substrate

Article Mar 2010 · IET MICROW ANTENNA P

Stanis Courrèges · Carlos Donado · Subhamoy Bhattacharya · John Papapolymerou

View Show abstract

Narrow-band microwave filter design

Article Nov 2007

Swanson, Daniel G., Jr

View Show abstract

Applications of Layer-by-Layer Polymer Stereolithography for Three-Dimensional High-Frequency Components

Article Dec 2004

Bosui Liu · Xun Gong · William J. Chappell

View Show abstract

Characterization of Electrodeposited Copper Foil Surface Roughness for Accurate Conductor Power Loss Modeling

M Griesi

Compact Ku band filter based on BMT dielectric resonators made in a single part using 3D ceramic stereo lithography process

L Carpentier · N Delhote · S Verdeyme · L Estagerie · H Leblond · D Pacaud

Recommended publications

Discover more

Article

Cleaning Technology on Filter Cake of Silicate-Based Polymer Drilling Fluid

February 2013 · Applied Mechanics and Materials

Qin Qin Ye · Yong Zhang Zhou · Dong Sheng Chen

In order to evaluate the cleaning effect on filter cake, a set of test device was designed. The cleaning fluid formula and parameters which were elected by experiments were optimized. The weight of the filter cake before and after cleaning was analyzed by wet weight method. New alkaline flush fluid formula was confirmed finally and the washing technology suitable for filter cake of silicate-based ... [Show full abstract]

Read more

Article

Projeto de filtros digitais IIR com técnicas de computação evolucionária

April 2012

Daniel Rossato de Oliveira

Read more

Article

Transfer-film technology to eliminate color-mixing problem of inkjet technology used in color filter...

January 2004

F.-L. Hsu · Y.-C. Lo · H.-A. Li · C.-C. Chien

Read more

Article

Filtering technology

June 2003 · Communications Engineer

J. Lillington

Read more

Last Updated: 10 Jul 2024

Download on the App Store

GET IT ON Google Play

Company

About us

News

Careers

Support

Help Center

Business solutions

Advertising

Recruiting

© 2008-2024 ResearchGate GmbH. All rights reserved.

Terms · Privacy · Copyright · Imprint · Consent preferences

A Low Loss X-band Filter Using 3-D Polyjet Technology

Fan Cai, Wasif Tanveer Khan, John Papapolymerou

Georgia Institute of Technology

Atlanta, USA

fcai6@gatech.edu

***Abstract* — In this paper, the Polyjet technology was applied to build high-Q X-band resonators and low loss filters for the first time. As one of state-of-the-art 3-D printing technologies, the Polyjet technique produces RF models with finest resolution and outstanding surface finish in a clean, fast and affordable way. The measured resonator with 0.3% frequency shift yielded a quality factor of 214 at 10.26 GHz. A Vertically stacked two-cavity bandpass filter with an insertion loss of 2.1 dB and 5.1% bandwidth (BW) was realized successfully. The dimensional tolerance of this process was found to be less than 0.5%. The well matched performance of the resonator and the filter, as well as the fine feature size indicate that the Polyjet process is suitable for the implementation of low loss and low cost RF devices.**

***Index Terms*— 3-D printing, cavity resonators, narrow bandpass cavity filter, Polyjet printing.**

I. INTRODUCTION

THREE dimensional (3-D) printing has recently received intense interest as it enables the development of cost effective, high performance, complex, and reliable components. This high-tech fabrication approach has demonstrated wide applications in bio-medical, mechanical, art and environmental areas by showing potential huge benefits. However, it is still in an early stage when it applies to the RF area.

To date low temperature Co-Fired Ceramic (LTCC) and Multi-Layer Organic (MLO) techniques have been the dominant methods for 3-D system on package (SOP) [1]-[2] RF front ends. However, they require several steps, such as etching, making masks, etc. These techniques are not only costly, but also show relatively increased complexity. The conventional microwave resonators and waveguides made of metal are heavy and bulky while costly to manufacture. Digital printed electronics can get rid of time consuming steps, be highly repeatable and largely reduce the new prototype manufacturing cost.

Currently, Polyjet technology represents state-of-the-art additive printing technology due to its high accuracy, edge visualization and fine feature details among all of the additive manufacturing technologies. Previously, the mostly used 3-D printing technology for RF structures was mainly implemented by strereolithography (SL) [3]-[5] due to its fine feature size of 50 μm. However, the Polyjet technology improves the resolution to 16 μm per layer. Recently in [6], it was demonstrated that a horn antenna was printed by Fused Deposition Modeling (FDM) with ABS plastic and coated by conductive spray. This process is low cost whereas the resolution is above 100 μm. Furthermore, the surface roughness is around 60 μm which is prohibitive for RF applications where the quality is a major concern.

In this paper, we demonstrate the rapid development of a low-cost, lightweight high-Q X-band resonator and bandpass filter implemented by Polyjet printing for the first time. The technique achieved 16 μm at individual layer thickness and the horizontal fabrication deviation was less than 0.5%. A single cavity resonator and a vertical stacked filter are analyzed and built. The theoretically calculated results are well-matched with measurements. The fabrication process is simplified as much as possible and only takes two steps: printing resin and sputtering or electroplating copper. The final parts were measured without tuning while the surface was not subjected to any post finishing process.

II. DESIGN

A. Resonator

The finite-element method (FEM) was used in the theoretical analysis to compute the EM fields inside the cavity with the aid of Ansys High Frequency Structure Simulator (HFSS).

First, a rectangular X-band cavity resonator was built to characterize the processing technique. The resonant frequency of the dominant mode TE_{101} dictates the dimensions of the cavity by

$$f_{101} = \frac{c}{2\pi\sqrt{\mu_r \varepsilon_r}} \sqrt{\left(\frac{m\pi}{a}\right)^2 + \left(\frac{n\pi}{b}\right)^2 + \left(\frac{l\pi}{d}\right)^2} \qquad (1)$$

Where a = 20.2 mm, b = 5 mm, and d = 21.4 mm are the width, height, and length of the cavity, respectively. m = l=1, n = 0 are the indexes for the 101 mode. f101 was calculated to be 10.2 GHz.

The proposed cavity resonator was made in two pieces and assembled along the vertical center plane, excited by two Pasternack connectors (PE44217). No obvious electric field distortion or degradation was found because the assembly plane was parallel to the E-field. The simulated E-field within the assembled cavity is shown in Fig. 1. The simulated quality factor was found to be 255 in HFSS with the built-in Huray Model to assess the additional loss caused by the surface roughness. The physical mechanism of the model and its implementation process is shown in [7]. The surface roughness is measured to be 0.5 μm±0.1um. The waviness in the surface roughness profile with a varied value of more than 3 μm increases the loss and this is effectively taken into account

within the Huray's model.

B. Filter

The vertically integrated two-pole filter can be developed by using two-cavity resonators from a 2nd-order Chebyshev filter calculation [8], [9]. The overhang structure is oriented vertically, therefore, it cannot be monolithically fabricated using traditional techniques such as micromachining and conventional printing. The fractional bandwidth is designed to be 3.9%. Each resonator has dimensions of 20.2 mm × 21.4 mm × 5 mm. The iris aperture is 6.2 mm wide. The wall of the resin is designed to be 3.18 mm thick for properly securing the excitation probes at the feeding position. The geometry of the two cavity filter is described in Fig. 2.

II. Fabrication

Polyjet 3-D printing is able to provide high-quality rapid prototyping with highest accuracy. It is easy, clean, quick and cost-effective. The outstanding surface finish, fine details and durability make this technique suitable for RF applications. In addition, the small-footprint system as well as the environmental friendly process make it ideal for future low cost RF product fabrication. The system contains 3-D printer jets and instantly UV-cures tiny droplets of liquid photopolymer. Fine layers accumulate on the build tray to create a precise 3D model or part. The complex and overhang shapes are formed by the removable gel-like support material which could be easily removed by hand, or with water. The final performance of the parts will be determined by manufacturing tolerances and the surface roughness.

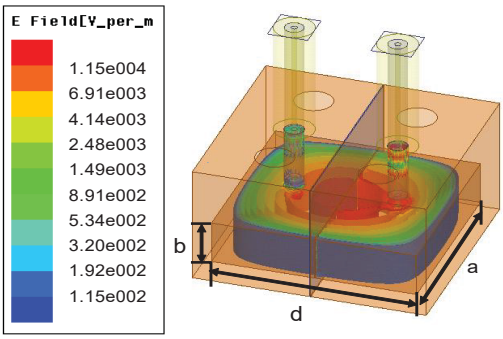


Fig. 1. Simulated E-field of the practical resonator with split plane.

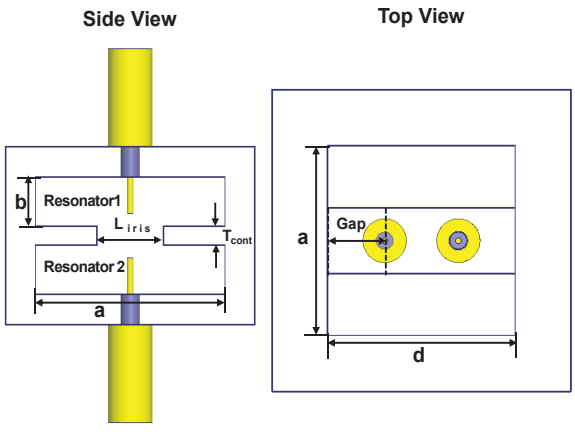


Fig. 2. HFSS simulation model of the two cavity filter.



Fig. 3. Objet Eden 250 system.

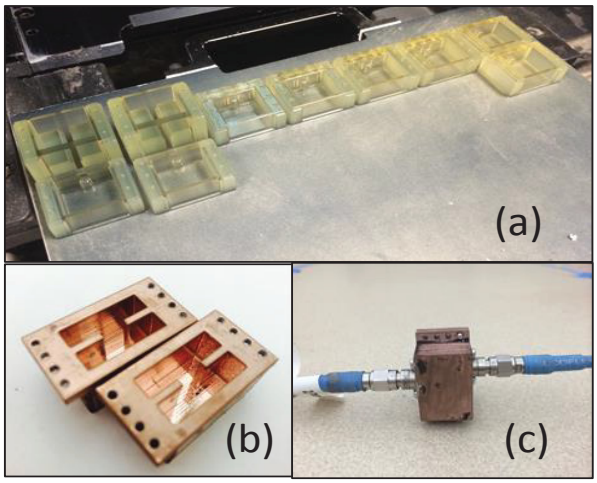


Fig. 4. Fabricated samples: (a) raw resin samples; (b) vertical filter sample after sputtering with copper; (c) assembled filter sample connected with K-band connectors.

The resonator and the filter were fabricated by the Objet Eden 250 system shown in Fig. 3 with UV curable resin. Aside from the fact that the resolution improves to a large extent, the fabrication process is much easier than traditional photolithography. The lateral resolution of Eden was larger than 15 μm while the vertical resolution was 16 μm. The fabrication process only includes two steps: printing the parts by the Objet Eden 250 system and sputtering 5 μm thick copper on the surface of the parts. The latter step can also be replaced by appropriate electroplating.

For the HFSS simulation models shown in Fig. 1 and Fig. 2, the dimensions were measured and summarized in Table I. The measured resonant frequency of the cavity resonator is shown both in Table I and in Fig. 5. The fabricated samples are shown in Fig. 4. The fabrication tolerance of the Polyjet process was less than 0.5%. The surface roughness of the parts is not uniform throughout the sample, but depends on the printing direction. It was found to be around 0.5 μm when the surface plane is parallel to the printing direction. However, this could be largely distorted when this is perpendicular to the surface plane or sacrificial materials exist.

TABLE I
FABRICATION TOLERANCES & RESONATOR'S FREQUENCY

	Des. (mm)	Fab. (mm)	Deviation
a	20.20	20.18	0.1%
b	5.00	4.98	0.4%
d	21.4	21.21	0.42%
L_{iris}	6.20	6.19	0.16%
T_{cont}	1.85	1.85	0.11%
Gap	6.00	6.01	0.17%
f_c	20.2	20.26	0.3%

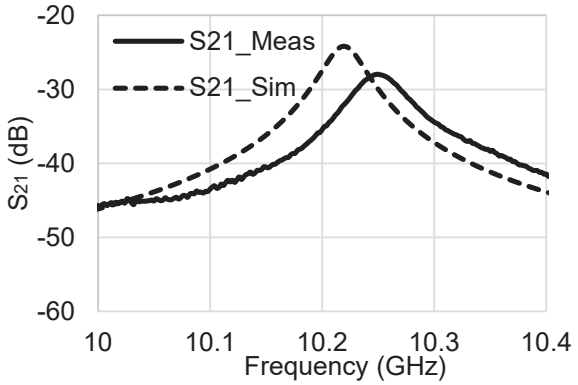


Fig. 5. Simulated and measured S21 of the single cavity resonator.

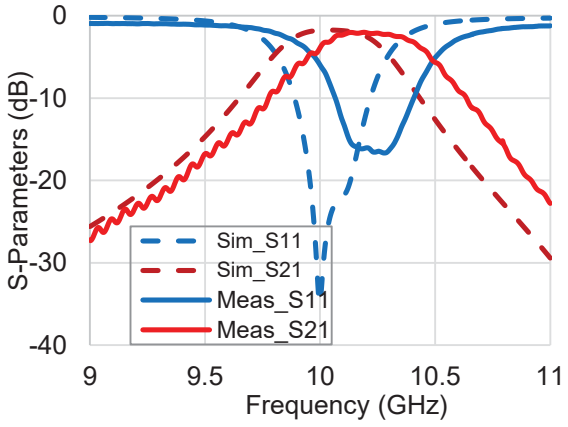


Fig. 6. Simulated and measured results of the filter.

III. MEASUREMENT

The filter was assembled with screws and the critical external coupling was achieved by using a coaxial line feed. The screws were placed inside holes that were "produced" as part of the prototype during the fabrication (no extra steps were needed for this). An SOLT calibration was performed. The reference planes for the measurement were at the edge of connectors. The measured and simulated results of the fabricated resonator and two-pole filter can be seen in Fig. 5 and Fig. 6, respectively. The small difference in the resonant frequency is due to the fabrication tolerances.

The loaded Ql of the cavity is defined as:

$$Q_l = \frac{f_0}{\Delta f_{3-dB}} \tag{2}$$

where f0 = 10.26 GHz is the measured resonant frequency and Δf3-dB = 0.05 GHz is the 3 dB bandwidth shown in Fig. 5. Based on (2) the loaded quality factor was measured to be 205. The weaker coupling observed in the measurement as compared to the simulation is due to the contact space between the connectors and the resonator. The external Qex of the resonator can be derived from the following equation:

$$S_{21}(dB) = 20log_{10}\frac{Q_l}{Q_{ex}} \tag{3}$$

Based on Qex and Ql, we can calculate Qu from Equation (4) and it is found to be 214.

$$\frac{1}{Q_l} = \frac{1}{Q_u} + \frac{1}{Q_{ex}} \tag{4}$$

The slight difference between the measured and simulated values of the unloaded quality factor can be attributed to possible increased surface roughness inside the walls of the fabricated cavities and non-idealities in the metal coverage of the resin material. This issue is still under investigation.

For the filter, the measured results matched closely with the simulations without any post-tuning. The measured fractional bandwidth was found to be 5.1%, compared to 3.9% of the designed value. The measured insertion loss (IL) was 2.1 dB, matching well the simulated value of 1.9 dB. The shift of the center frequency between the simulation model and the fabricated prototype is 0.2 GHz, representing 2% variation. In addition, the return loss (RL) is better than 15 dB through the pass band.

IV. CONCLUSIONS

This paper presents the Polyjet printing technology for RF application for the first time. It shows the best precision among all of the additive printing technologies and thus produces measurements which agreed very well with the simulations. The fabricated resonator showed an unloaded quality factor of 214 at X-band with slight frequency shift by 0.3%. The insertion loss of the fabricated filter was measured to be 2.1 dB with 15 dB return loss. The fractional bandwidth was 5.1%. The

loss is mainly due to surface roughness and possible non-idealities in the metal coverage of the resin material. These results indicate that the developed Polyjet printing process is promising for the next generation low cost passive RF components.

V. Acknowledgment

This work was supported by the National Science Foundation under grant number ECCS-1231869.

VI. References

[1] M. Moallem, J. East, and K. Sarabandi, "A broadband, micromachined rectangular waveguide to cavity-backed coplanar waveguide transition using impedance-taper technique," *IEEE Tran. THz Sci. Tech.,* vol. 4, no. 1, pp. 49–55, Jan. 2014.

[2] Y. Li, B. Pan, M. Tentzeris and J. Papapolymerou, "A Fully Micromachined W-Band Coplanar Waveguide to Rectangular Waveguide Transition," in *IEEE MTT-S Int. Microwave Symp.,* Honolulu, HI, USA, June 2007, pp. 1031-1034.

[3] B. Liu, X. Gong, and W. J. Chappell, "Layer-by-layer polymer stereolithography fabrication for three-dimensional RF components," *IEEE MTT-S Int. Microwave Symp. Dig.*, June 2004, pp. 481–484.

[4] L. Carpentier, N. Delhote, S. Verdeyme, L. Estagerie, H. Leblond, D. Pacaud, "Compact Ku band filter based on BMT dielectric resonators made in a single part using 3D ceramic stereolithography process", *IEEE MTT-S Int. Microwave Symp. Dig*., June 2012.

[5] C. R. Garcia , R. C. Rumpf , H. H. Tsang and J. H. Barton "Effects of extreme surfaceroughness on 3D printed horn antenna", *Electron.Lett.*, vol. 49, no. 12, pp.734 -736 2013.

[6] J. Chieh, B. Dick, S. Loui, J. Rockway, "Development of a Ku-Band Corrugated Conical Horn Using 3-D Print Technology", *IEEE Antennas and Wireless Propagation Letters*, Volume. 13, pp. 201-204, Jan. 2014.

[7] M. Griesi, "Characterization of Electrodeposited Copper Foil Surface Roughness for Accurate Conductor Power Loss Modeling" Thesis, 2014.

[8] S. Courreges, C. A. Donado Morcillo, S. Bhattacharya, and J. Papapolymerou, "Reduced-size multilayer x-band filters with stacked resonators on a flexible organic substrate," *IET Microwaves, Antennas and Propagation*, vol. 4, no. 2, pp. 277-285, 2010.

[9] D. G. Swanson, "Narrow-band microwave filter design," *IEEE Microw. Mag.*, vol. 8, no. 5, pp. 105–114, Oct. 2007.

APPENDIX GRIESI03

A low loss X-band filter using 3-D Polyjet technology

Publisher: IEEE Cite This PDF

Fan Cai ; Wasif Tanveer Khan ; John Papapolymerou All Authors

15 Cites in Papers

605 Full Text Views

Abstract

Document Sections

I. Introduction

II. Design

II. Fabrication

III. Measurement

IV. Conclusions

Authors

Figures

References

Citations

Keywords

Metrics

Abstract:
In this paper, the Polyjet technology was applied to build high-Q X-band resonators and low loss filters for the first time. As one of state-of-the-art 3-D printing technologies, the Polyjet technique produces RF models with finest resolution and outstanding surface finish in a clean, fast and affordable way. The measured resonator with 0.3% frequency shift yielded a quality factor of 214 at 10.26 GHz. A Vertically stacked two-cavity bandpass filter with an insertion loss of 2.1 dB and 5.1% bandwidth (BW) was realized successfully. The dimensional tolerance of this process was found to be less than 0.5%. The well matched performance of the resonator and the filter, as well as the fine feature size indicate that the Polyjet process is suitable for the implementation of low loss and low cost RF devices.

Published in: 2015 IEEE MTT-S International Microwave Symposium

Date of Conference: 17-22 May 2015 **DOI:** 10.1109/MWSYM.2015.7166895

Date Added to IEEE *Xplore*: 27 July 2015 **Publisher:** IEEE

Electronic ISBN:978-1-4799-8275-2 **Conference Location:** Phoenix, AZ, USA

Print ISSN: 0149-645X

I. Introduction

Three dimensional (3-D) printing has recently received intense interest as it enables the development of cost effective, high performance, complex, and reliable components. This high-tech [illegible] ated wide applications in bio-medical, mechanical, art and environmental areas by showing potential huge benefits. However, it is still in an early stage when it applies to the RF area

Sign in to Continue Reading

Authors

Figures

References

Export References & Cited By

Select All

More Like This

Early GaAs FET monolithic microwave integrated circuit developments for radar applications at Plessey, UK
2008 IEEE MTT-S International Microwave Symposium Digest
Published: 2008

Dielectric Resonator Filters for Application in Microwave Integrated Circuits
IEEE Transactions on Microwave Theory and Techniques
Published: 1971

Show More

1. M. Moallem, J. East and K. Sarabandi, "A broadband micromachined rectangular waveguide to cavity-backed coplanar waveguide transition using impedance-taper technique", *IEEE Tran. THz Sci. Tech.*, vol. 4, no. 1, pp. 49-55, Jan. 2014.
View Article Google Scholar

2. Y. Li, B. Pan, M. Tentzeris and J. Papapolymerou, "A Fully Micromachined W-Band Coplanar Waveguide to Rectangular Waveguide Transition", *IEEE MTT-S Int. Microwave symp.*, pp. 1031-1034, June 2007.
View Article Google Scholar

3. B. Liu, X. Gong and W. J. Chappell, "Layer-by-layer polymer stereolithography fabrication for three-dimensional RF components", *IEEE MTT-S Int. Microwave Symp. Dig.*, pp. 481-484, June 2004.
View Article Google Scholar

4. L. Carpentier, N. Delhote, S. Verdeyme, L. Estagerie, H. Leblond and D. Pacaud, "Compact Ku band filter based on BMT dielectric resonators made in a single part using 3D ceramic stereo lithography process", *IEEE MTT-S Int. Microwave Symp. Dig.*, June 2012.
Google Scholar

5. C. R. Garcia, R. C. Rumpf, H. H. Tsang and J.H. Barton, "Effects of extreme surfaceroughness on 3D printed horn antenna", *Electron. Lett.*, vol. 49, no. 12, pp. 734-736, 2013.
CrossRef Google Scholar

6. J. Chieh, B. Dick, S. Loui and J. Rockway, "Development of a Ku-Band Corrugated Conical Horn Using 3-D Print Technology", *IEEE Antennas and Wireless Propagation Letters*, vol. 13, pp. 201-204, Jan. 2014.
View Article Google Scholar

7. M. Griesi, "Characterization of Electrodeposited Copper Foil Surface Roughness for Accurate Conductor Power Loss Modeling", 2014.
Google Scholar

8. S. Courreges, C. A. Donado Morcillo, S. Bhattacharya and J. Papapolymerou, "Reduced-size multilayer x-band filters with stacked resonators on a flexible organic substrate", *IE Microwaves Antennas and Propagation*, vol. 4, no. 2, pp. 277-285, 2010.
CrossRef Google Scholar

9. D. G. Swanson, "Narrow-band microwave filter design", *IEEE Microw. Mag.*, vol. 8, no. 5, pp. 105-114, Oct. 2007.
View Article Google Scholar

Citations

Keywords

Metrics

CHANGE USERNAME/PASSWORD

PAYMENT OPTIONS

VIEW PURCHASED DOCUMENTS

COMMUNICATIONS PREFERENCES

PROFESSION AND EDUCATION

TECHNICAL INTERESTS

US & CANADA: +1 800 678 4333

WORLDWIDE: +1 732 981 0060

CONTACT & SUPPORT

About IEEE *Xplore* | Contact Us | Help | Accessibility | Terms of Use | Nondiscrimination Policy | IEEE Ethics Reporting | Sitemap | IEEE Privacy Policy

A not-for-profit organization, IEEE is the world's largest technical professional organization dedicated to advancing technology for the benefit of humanity.

© Copyright 2024 IEEE - All rights reserved, including rights for text and data mining and training of artificial intelligence and similar technologies.